DE-AC02-76ER01198

DOE/ER/01198/1389

AN ULTRASONIC STUDY OF TRAPPED HYDROGEN IN NIOBIUM

DO NOT MICROFILM
COVER

BY

KAI-FENG HUANG

B.S., National Taiwan University, 1976
M.S., University of Illinois, 1978

THESIS

Submitted in partial fulfillment of the requirements
for the degree of Doctor of Philosophy in Physics
in the Graduate College of the
University of Illinois at Urbana-Champaign, 1982

DISTRIBUTION OF THIS DOCUMENT IS UNLIMITED

Urbana, Illinois

PACS indices: 61.70.Bv
62.80.+f
63.20.Mt

DISCLAIMER

This report was prepared as an account of work sponsored by an agency of the United States Government. Neither the United States Government nor any agency Thereof, nor any of their employees, makes any warranty, express or implied, or assumes any legal liability or responsibility for the accuracy, completeness, or usefulness of any information, apparatus, product, or process disclosed, or represents that its use would not infringe privately owned rights. Reference herein to any specific commercial product, process, or service by trade name, trademark, manufacturer, or otherwise does not necessarily constitute or imply its endorsement, recommendation, or favoring by the United States Government or any agency thereof. The views and opinions of authors expressed herein do not necessarily state or reflect those of the United States Government or any agency thereof.

DISCLAIMER

Portions of this document may be illegible in electronic image products. Images are produced from the best available original document.

DOE/ER/01198--1389

DE83 001127

DOE/ER/01198--1389

AN ULTRASONIC STUDY OF TRAPPED HYDROGEN IN NIOBIUM

MASTER

BY

KAI-FENG HUANG

B.S., National Taiwan University, 1976
M.S., University of Illinois, 1978

THESIS

Submitted in partial fulfillment of the requirements
for the degree of Doctor of Philosophy in Physics
in the Graduate College of the
University of Illinois at Urbana-Champaign, 1982

DISCLAIMER

This report was prepared as an account of work sponsored by an agency of the United States Government. Neither the United States Government nor any agency thereof, nor any of their employees, makes any warranty, express or implied, or assumes any legal liability or responsibility for the accuracy, completeness, or usefulness of any information, apparatus, product, or process disclosed, or represents that its use would not infringe privately owned rights. Reference herein to any specific commercial product, process, or service by trade name, trademark, manufacturer, or otherwise, does not necessarily constitute or imply its endorsement, recommendation, or favoring by the United States Government or any agency thereof. The views and opinions of authors expressed herein do not necessarily state or reflect those of the United States Government or any agency thereof.

Urbana, Illinois

DISTRIBUTION OF THIS DOCUMENT IS UNLIMITED

PACS indices: 61.70.Bv
62.80.+f
63.20.Mt

THIS PAGE

WAS INTENTIONALLY

LEFT BLANK

AN ULTRASONIC STUDY OF TRAPPED HYDROGEN IN NIOBIUM

Kai-feng Huang, Ph.D.
Department of Physics
University of Illinois at Urbana-Champaign, 1982

The purpose of the present work is to establish a model for the configuration of hydrogen trapped at interstitial oxygen or nitrogen impurities in BCC metals. Such a model would be important for an understanding of the physical properties of such systems, particularly of the quantum diffusion effects which occur.

A review of all the available data (specific heat, internal friction, neutron scattering, channeling, thermal conductivity) on Nb-O-H or Nb-N-H systems, is first given. By reexamining the data for clues, an eight-state tunnelling model is proposed, and the properties of the system are developed. A comparison of the predictions of this model with the data is given, and the four parameters that describe the model are determined. A simple potential calculation is also performed to demonstrate the qualitative features of the model.

Measurements have been made of ultrasonic attenuation and velocity in the Nb-O-H system as a function of temperature, frequency, polarization and isotope. In addition to the previously found stable peak, an additional peak is found when the specimen is cooled rapidly. The peak anneals at the same temperature as those found by Hanada in their resistivity quenching experiments, indicating that the quenched-in defect is an OH_2 complex. An extension of the model described in Part A is given to account for the relaxation.

ACKNOWLEDGMENTS

The author would like to thank his advisor, Professor A. V. Granato for his patience, advice, and encouragement throughout the course of this investigation and during the preparation of this thesis.

He also expresses gratitude to Professor H. K. Birnbaum for assistance in the preparation and charging of the samples, and for the many helpful discussions.

He is grateful to Bernard Ho for some helpful discussions in the preparation of the thesis.

Finally, the author wishes to express his love and appreciation to his wife, Yi-kuang, for her patience, understanding, and encouragement during his graduate work at the University of Illinois.

The author gratefully acknowledges the support of the United States Department of Energy under contract DE-AC02-76ER01198.

TABLE OF CONTENTS

CHAPTER Page

LIST OF FIGURES

FIGURE Page

LIST OF TABLES

PART A

I. INTRODUCTION

The purpose of the present work is to establish a model for the configuration of hydrogen trapped at interstitial impurities in BCC transition metals. Such a model would be important for an understanding of the physical properties of such systems, particularly of the quantum diffusion effects which occur.

At high temperatures, it is known[1,2] that impurity atoms like nitrogen, oxygen and carbon occupy octahedral symmetry interstitial sites, and that hydrogen is located at tetrahedral sites[3-5] (Fig. 1). At low temperatures, the solubility of hydrogen is low, and H precipitates out in a hydride phase in pure Nb, but becomes trapped at O or N in impure Nb. There have been many experiments using many different experimental techniques (specific heat, internal friction, neutron and x-ray scattering, channeling, thermal resistivity), but no generally accepted model for the configuration has been established. There have been some models developed to explain some of the results, but which fail to explain others.

We first review the existing evidence for clues in the next section (II). In Section III, a model is proposed, and the properties of this system are developed. In Section IV, a comparison of the predictions of this model with available data is given, and the four parameters of the model are determined. In Part B, ultrasonic studies of rapidly cooled Nb-O-H are given and discussed in terms of an extension of the model in Part A in Section III. The model is found to give a reasonable account of all available data.

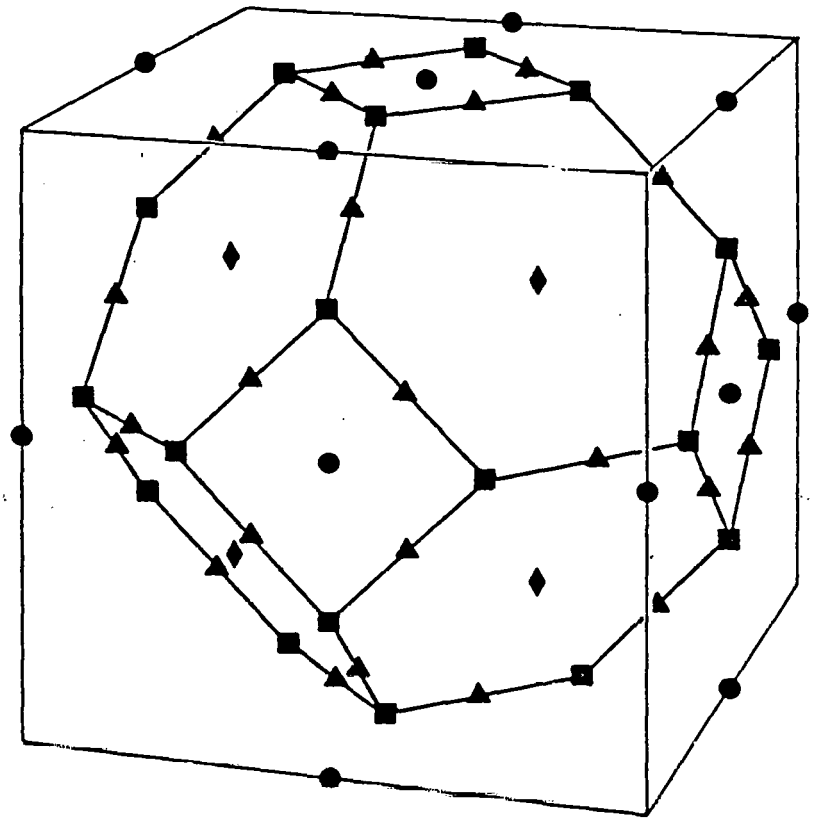

Figure 1. Possible interstitial sites of hydrogen in niobium

● - Octahedral symmetry
■ - Tetrahedral symmetry
▲ - Triangular symmetry
♦ - Hexahedral symmetry

II. REVIEW OF PREVIOUS EXPERIMENTS AND EXISTING MODELS

1. Specific Heat

Measurements of the specific heat of niobium containing hydrogen by Sellers, Anderson and Birnbaum[6] showed the existence of an excess heat capacity below 1.5 K. The large difference between the excess heat capacity due to hydrogen and deuterium as shown in Fig. 2, suggested that the effect might be due to quantum mechanical tunnelling of the interstitial hydrogen in the niobium lattice. This was consistent with studies of diffusion of hydrogen in niobium which indicated a non-Arrhenius temperature dependence at low temperatures,[7-8] and a non-classical isotope effect.[9-10]

2. Thermal Conductivity

The effect of hydrogen and deuterium upon the thermal conductivity of niobium was investigated by O'Hara, Sellers and Anderson.[11] If there exists eigenstates which contribute to the heat capacity, their coupling to phonon modes might be possible. This would produce a minimum in the phonon mean free path at nearly the same temperature as the heat capacity contributions. Their measurements indicate minima in the phonon mean free path at 0.8 K for hydrogen and 0.1 K for deuterium (Fig. 3), where the contributions to the heat capacity occur. Removal of the hydrogen or deuterium reduced the minima, indicating the connection between phonon scattering and hydrogen defects.

However, hydrogen in Nb was later shown to precipitate at low temperatures into the beta phase hydride by Westlake and Ockers.[12] There should not exist too much α-phase (free) hydrogen in the lattice, which

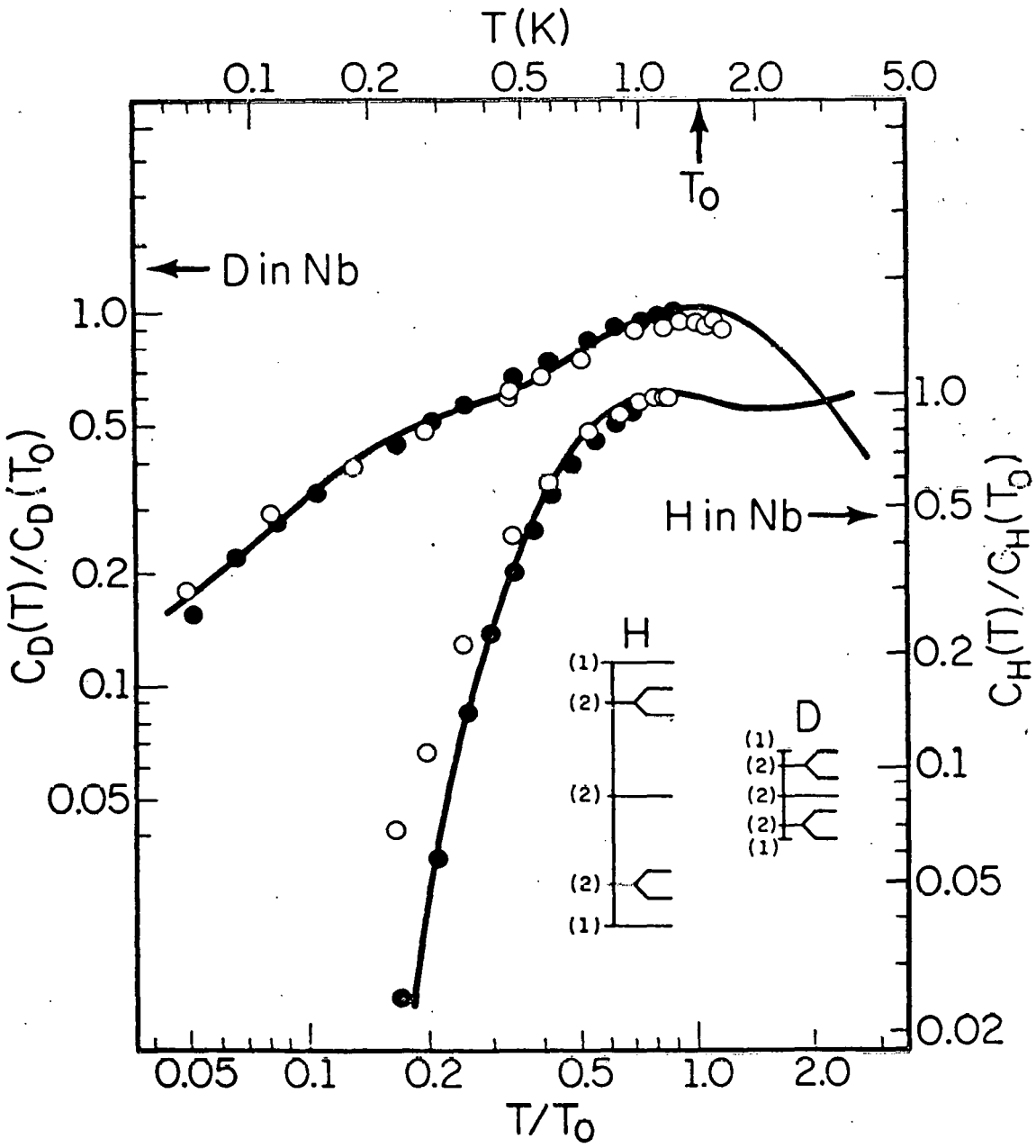

Figure 2. Experimental heat capacities as a function of temperature for hydrogen and deuterium in niobium The open circles are for as-received specimens, while the closed circles are for 3000 ppm charged specimens. The solid lines represent the fit of the Birnbaum-Flynn model. The energy level spectra for hydrogen and deuterium are shown at the lower right. (From Birnbaum and Flynn[21])

Figure 3. Phonon mean free paths, ℓ, in Nb limited by scattering mechanisms other than the sample surfaces. The phonon mean free path attributed to boundary scattering is indicated by the dashed line. Electrons dominate the scattering above ≃ 2 K. The symbols represent: ■ , annealed and out-gassed Nb; × Nb with D intentionally added; ▲ Nb with H intentionally added; O, Nb with H removed. The additional scattering caused by the introduction of D can be seen roughly by comparing the (×) and (O) data. (From O'Hara, Sellers and Anderson[11])

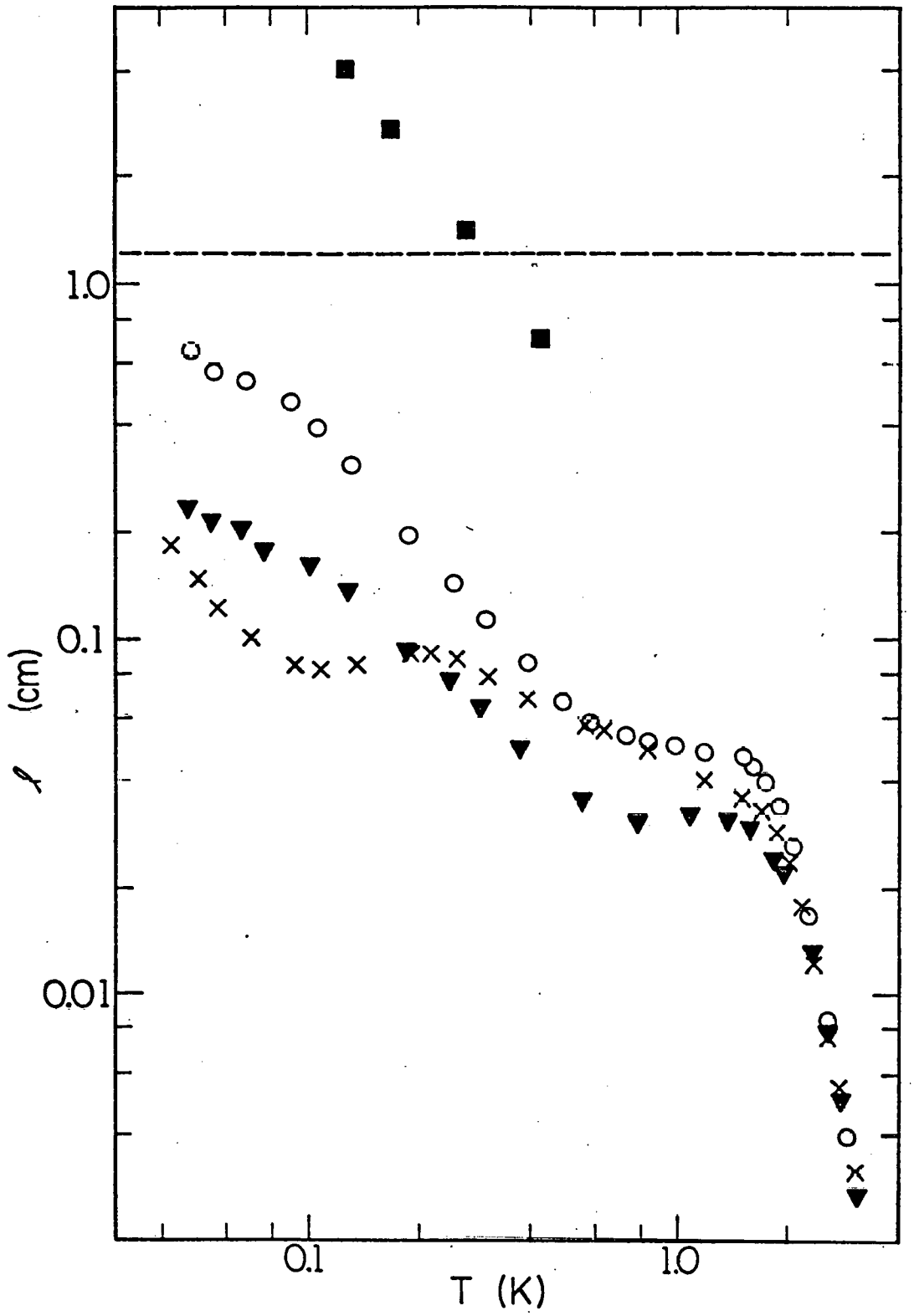
1.0
0.1
0.01
ℓ (cm)
0.1
1.0
T (K)

was suggested by Sellers, et al.[6] as the defects that caused the excess heat capacity and the mean free path minima. It was proved later by other experiments that it is the hydrogen trapped by some heavy interstitials like O or N, rather than the free hydrogen, that caused the low temperature quantum effects.

3. Effect of Interstitial Trapping

As early as 1973, Baker and Birnbaum[7,9] showed that anelastic relaxations of hydrogen charged niobium, which appear around 150 K at 10 MHz, were due to complexes of O-H or N-H pairs. These relaxations are believed to be caused by reorientations of the hydrogen around the trapping interstitial O or N in the presence of an applied stress.

Resistivity measurements by Pfeiffer and Wipf[13] verified the trapping of hydrogen in niobium. Their analysis indicates that only one hydrogen atom traps at any one nitrogen interstitial, with any excess hydrogen precipitating. A binding energy of 0.12 eV was found, consistent with the result of Baker and Birnbaum.

The heat capacity experiments by Sellers, Anderson and Birnbaum were redone by Morkel, Wipf and Neumaier[14] to investigate the effect of nitrogen trapping. They found that no excess heat capacity was present in nitrogen free samples. The introduction of nitrogen produced excess heat capacities similar to those found previously by Sellers, Anderson and Birnbaum. They concluded that the excess heat capacity is due to N-H pairs and that below 80 K the concentration of free hydrogen is less than 1 ppm.

4. Neutron Scattering

Inelastic neutron scattering experiments by Magerl, Wagner and Stump,[15]

and also Richter and Shapiro,[16] revealed the local vibrational spectra of hydrogen in niobium. It is found that the energy spectra have the following features,

(1) There are two vibrational levels centered at 0.11 eV and 0.16 eV with an intensity ratio of 1:2, which indicates that the higher vibrational level is doubly degenerate.

(2) The energy levels for deuterium are 0.085 eV and 0.12 eV with the same intensity ratio of 1:2.

Shown in Fig. 4 is the spectra for NbH and NbD. Later experiments by Rush, et al.[17] showed that there is not much change in the vibrational levels for the α-phase hydrogen and the hydrogen trapped at nitrogen or oxygen.

An inelastic neutron scattering experiment by Wipf, et al.[18] was made at two different temperatures (0.09 K and 5 K) on a polycrystalline Nb sample containing 1.3 at % of O-H pairs. The results are shown in Fig. 5. At the lower temperature (0.09 K), the intensity shoulder at ∿ 0.2 meV on the energy loss side demonstrates the presence of inelastic scattering processes (energy gain processes do not occur at this low temperature). At 5 K, the intensity on the energy gain side increases, whereas it decreases on the energy loss side. This decrease indicates that the scattering is not due to phonons since, in such a case, the scattering would increase with temperature. It was then proposed by Wipf, et al. that the inelastic scattering results from energy transfer to hydrogen tunnelling states. A tunnelling matrix element of .19±.04 meV is found which agrees with the value of 0.14±0.05 meV found by Wipf and Neumaier[19] from the specific heat measurements. (Since major specific heat contributions for an assumed two level system are expected for

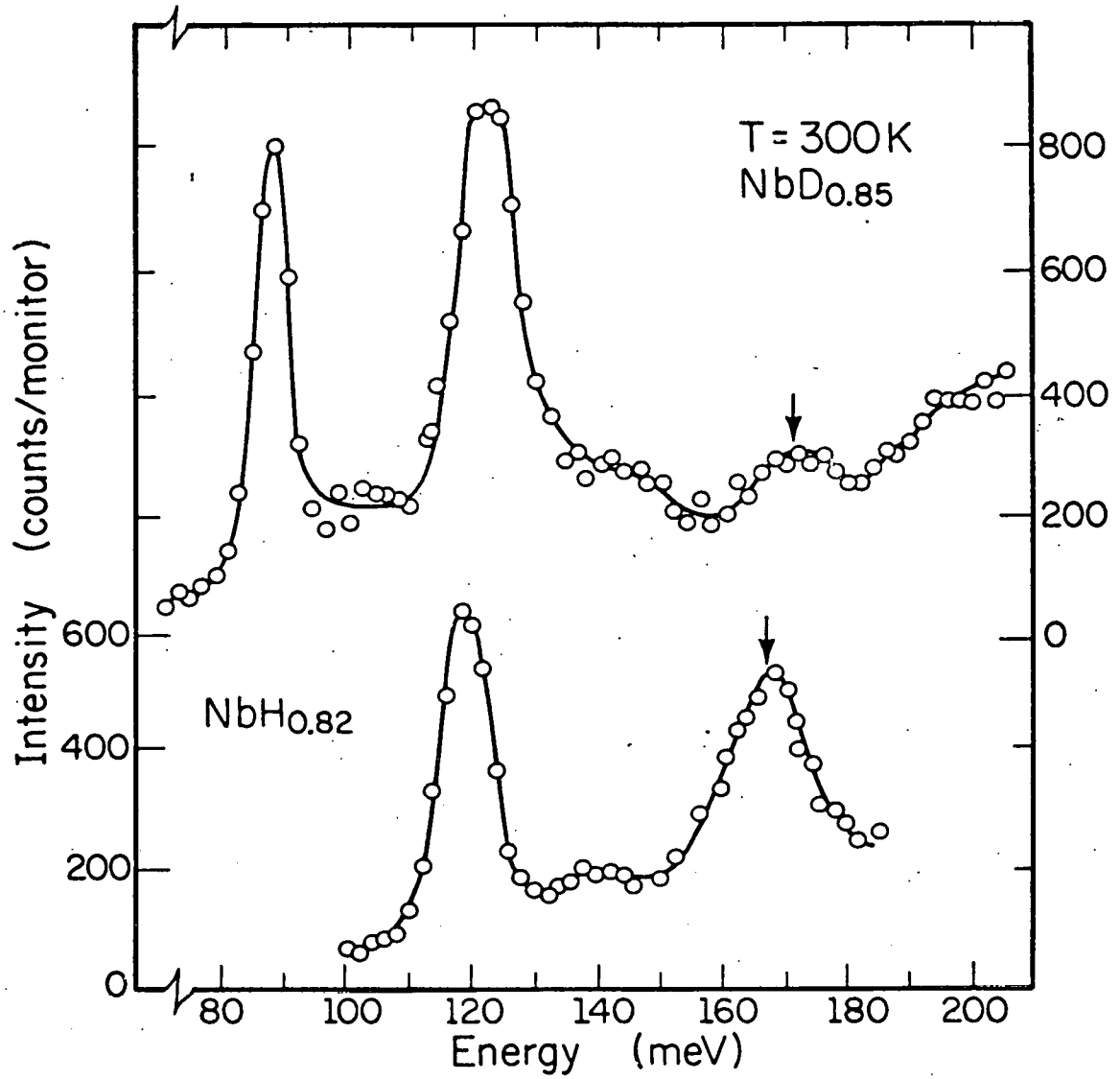

Figure 4. Spectra obtained on $NbD_{0.85}$ and $NbH_{0.82}$ at room temperature. The width of the second peak is about twice that of the first peak for both hydrogen and deuterium, indicating that the higher level is doubly degenerate. There is an isotope effect. The energy values of these peaks for deuterium are reduced by a factor of 1.4. The arrow indicates the position of the second harmonic of the lower deuterium vibrational level. (From Richter and Shapiro[16])

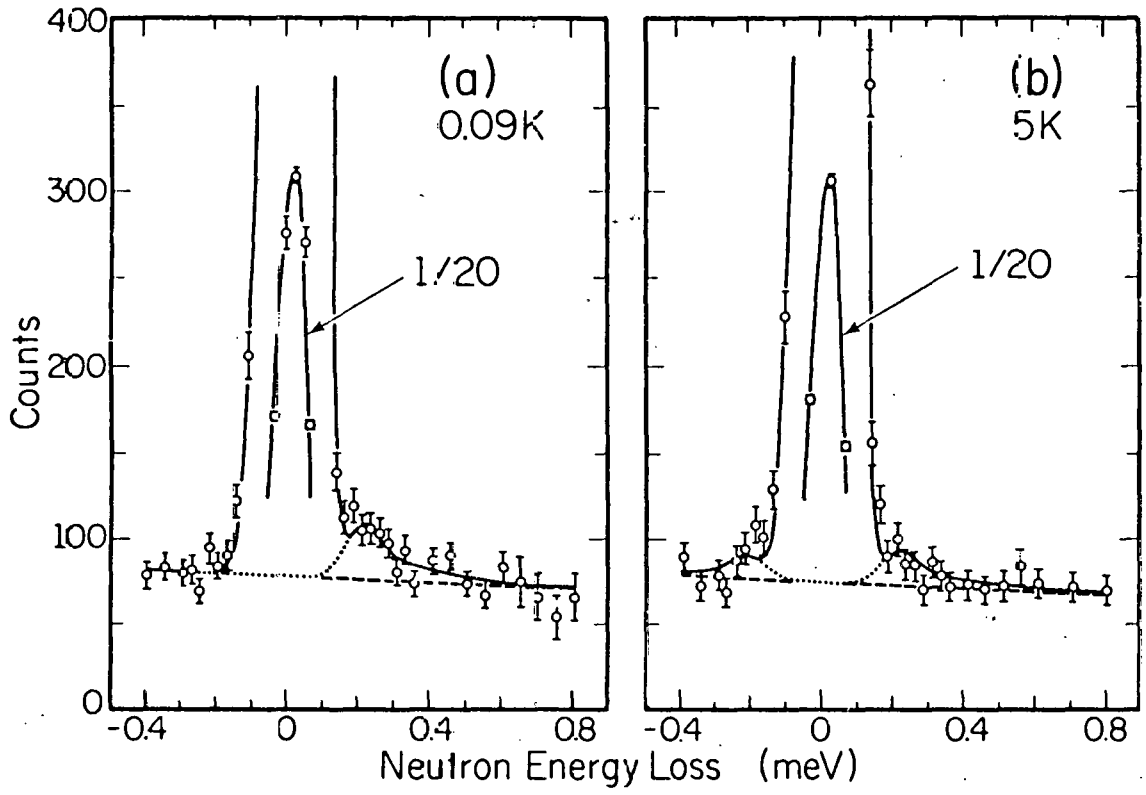

Figure 5. Inelastic neutron spectra of $NbO_{0.013}H_{0.016}$ at 0.09 K (a) and 5 K (b). At the lower temperature (0.09 K), the intensity shoulder at $\sim$ 0.2 meV on the energy loss side demonstrates the presence of inelastic scattering processes (energy gain processes do not occur at this low temperature). At 5 K, the intensity on the energy gain side increases, whereas it decreases on the energy loss side. This temperature dependence is typical for neutron scattering on tunnelling systems. (From Wipf, et al.[18])

$T \geq 0.42\ \Delta E$ (where ΔE is the smallest energy gap), a value for this ΔE between 0.15 and 0.2 meV can be concluded immediately from the specific heat data.)

5. Low Temperature Ultrasonic Results

The thermal conductivity results by O'Hara, et al.[11] indicates a coupling of hydrogen defects to phonons, suggesting that the hydrogen defects may affect the elastic constants and also show relaxation effects. Poker, Setser, Granato and Birnbaum[20] made measurements of ultrasonic attenuation and velocity on Nb-O-H alloys as a function of temperature, frequency and wave polarizations. The results showed a relaxation peak near 2.5 K at 10 MHz. The decrement and elastic constant change are shown in Fig. 6. The peak was seen only in the C' mode, but not the C_{44} mode. The relaxation time was found to be Arrhenius (Fig. 7) with an activation energy of 1.8 meV and a frequency factor of 3.89×10^{10}, which are too small for a classical system. It was also found that the relaxation strength deviates from the classical 1/T temperature dependence (Fig. 8), indicating a low temperature quantum depletion of the states which are involved in the relaxation transition. An energy of 0.4 meV was found for the energy difference between the ground state and the first excited states which were assumed to be the states involved in the relaxation transition. The data require a minimum of 4 tunnelling states, or a configuration of at least 4 equivalent sites. The deuterium results (Fig. 9) were very different from those of hydrogen. Instead of a relaxation peak, a step rise in the decrement was observed near 2 K.

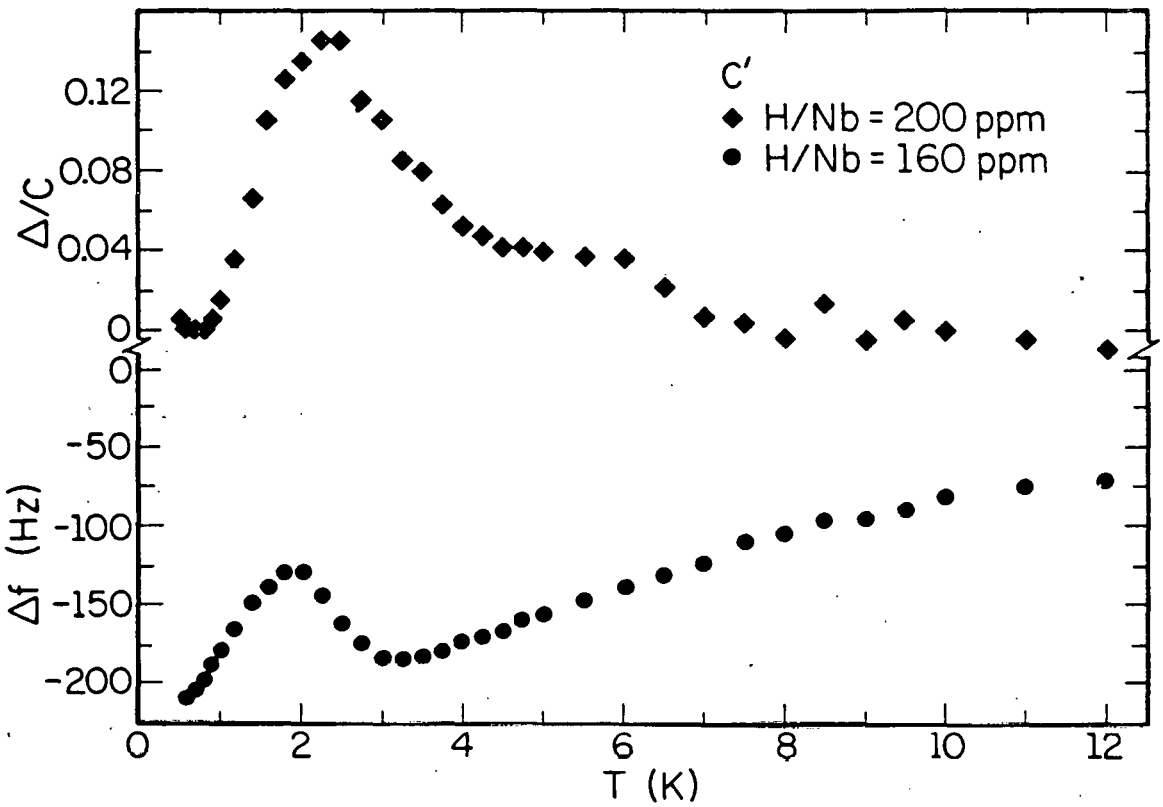

Figure 6. The decrement per unit concentration for H/Nb = 200 ppm and frequency change for H/Nb = 160 ppm as functions of temperature for a 10 MHz C' mode. The dispersion in the frequency change occurs in the same temperature range as the peak in the decrement. (From Poker[22])

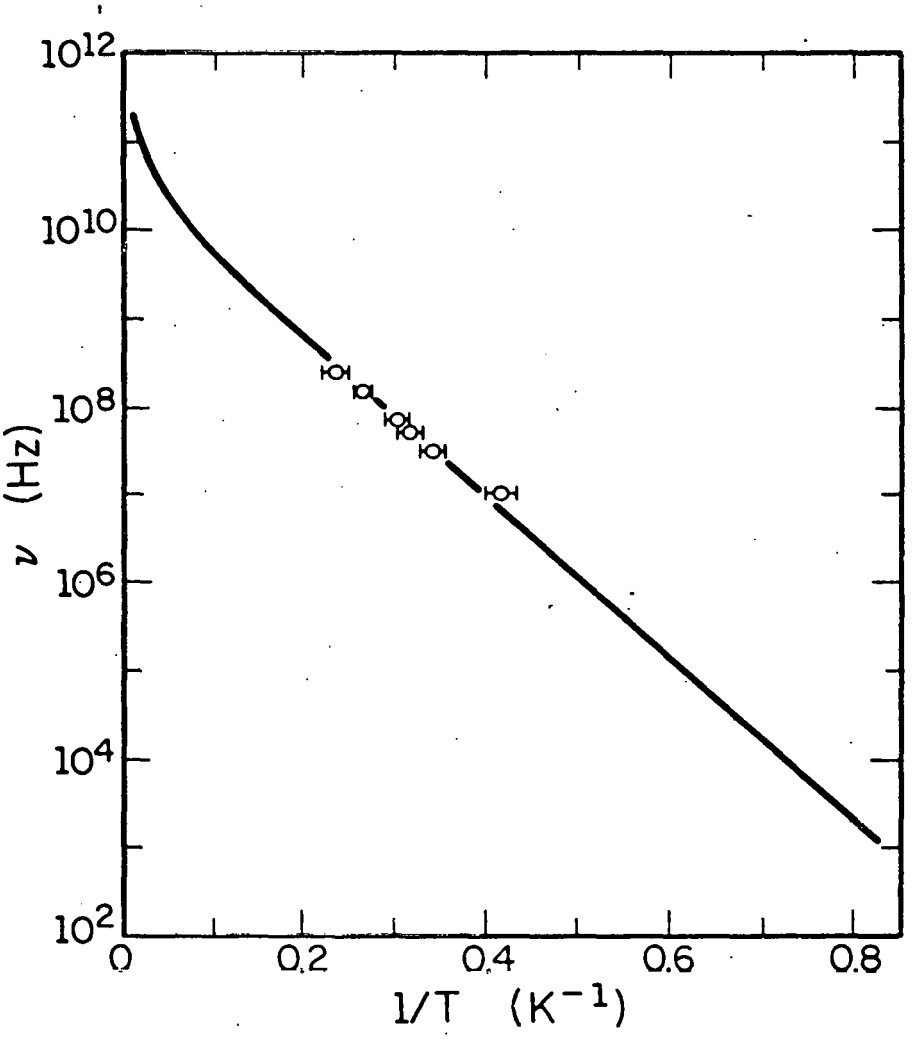

Figure 7. The relaxation frequency as a function of inverse temperature. The solid line through the data points is the fit to the theory, with an activation energy of 1.8 meV and a frequency factor of 3.89×10^{10}. (From Poker[22])

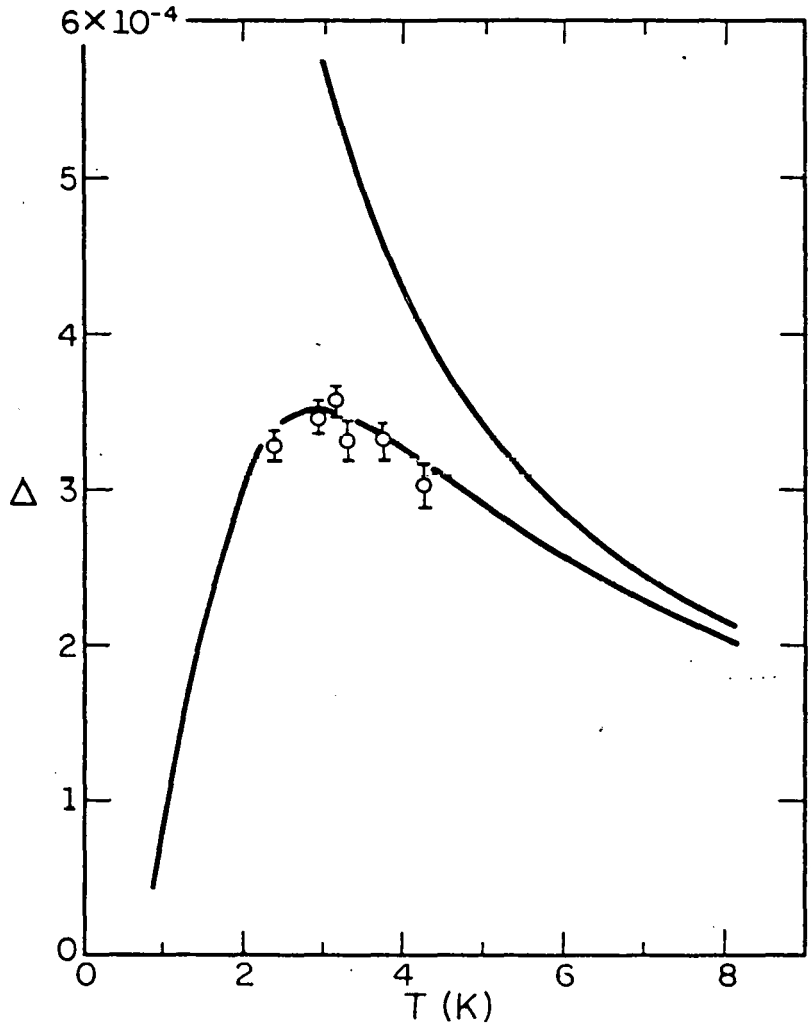

Figure 8. The relaxation strength versus temperature. The solid curve through the data points is the fit of the eight-state model with the parameter $2\alpha/k = 4.5$ K. The other curve indicates the classical relaxation strength which approaches the same high temperature limit as the eight-state model. (From Poker[22])

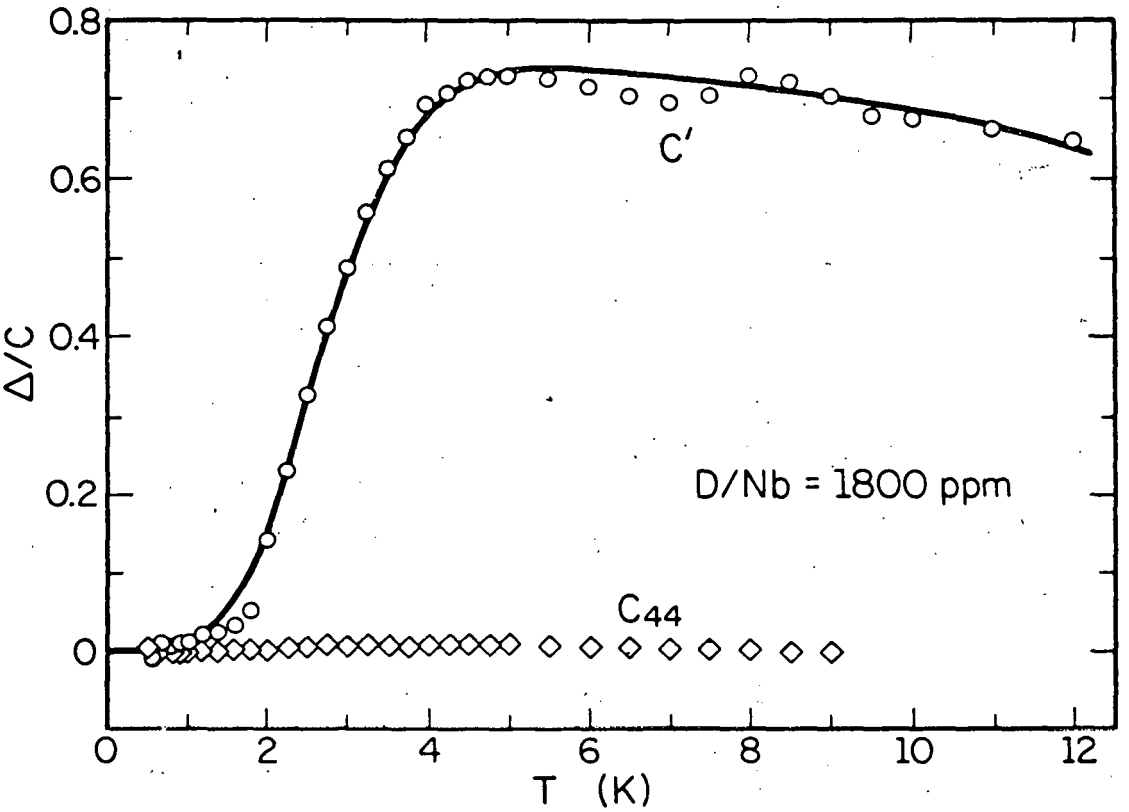

Figure 9. The decrement per unit concentration for D/Nb = 1800 ppm as a function of temperature for the C' and C_{44} modes. The solid curve is the fit of the eight-state model with $\alpha = 0.06$ meV and $n_1 = 8 \times 10^{-4}$.

6. Existing Models

Birnbaum and Flynn[21] were the first to propose a delocalized model which was meant to explain the specific heat result. They assumed that hydrogen is spread out over the four tetrahedral and four triangular sites on the face of a unit cell. An offset energy is assigned for the energy difference between tetrahedral and triangular sites, and only the tunnelling between adjacent tetrahedral and triangular sites is allowed. Some of the states couple to strains of the lattice. Their fit to the heat capacity is shown in Fig. 2. The energy level diagrams for both hydrogen and deuterium corresponding to the best fit are shown in the lower right corner.

Poker[22] found that an elaboration of the Birnbaum Flynn model to take account of the external stress and the trapping oxygen could explain their ultrasonic data. The first excited states are doubly degenerate and this degeneracy is lifted when stress is applied. An Orbach process is proposed to account for the relaxation, since the relaxation time then has an exponential temperature dependence. This model was criticized by Wipf, et al.[23] on the grounds that

(1) There is no independent evidence for occupancy of the assumed triangular sites and

(2) An offset energy for the triangular sites of less than 1.8 meV is required to obtain the activation energy. This is rather unlikely for two inequivalent sties.

Wipf and Neumaier[19] proposed instead a two-site tunnelling model, in which hydrogen tunnels through two adjacent tetrahedral sites. The two energy levels are separated by $(J^2 + \varepsilon^2)^{1/2}$, where J is the tunnelling

matrix element and ε is the strain energy. A Lorentzian distribution was assumed and the neutron scattering data and specific heat data can be explained. However, in order to account for the rather small specific heat and high concentration of N-H pairs, they had to use a very broad strain distribution so that only a small fraction of the total number of N-H pairs could contribute to the low temperature specific heat. It is worth noting that the specific heat data for both hydrogen and deuterium start to level off at 1.0 K. But the two state model would predict that it is still increasing linearly due to the fact that there are still states available at higher temperatures. A more detailed discussion of the fitting will be given in Section IV.

To find a satisfactory model for the trapped hydrogen, it is useful to reexamine all the experimental data from different sources. First of all, the low temperature ultrasonic data provides a piece of very important information, which concerns the number of sites that hydrogen tunnels through. The low temperature quantum depletion of the relaxation strength and also the Orbach process required to explain the relaxation time suggest that there should be at least four tunnelling sites, ground state, two doubly degenerate states for the relaxation and a fourth state as the intermediate state for the Orbach process. This suggests consideration of a four-state model consisting of the four nearest neighbouring tetrahedral sites in a plane around the oxygen impurity (The four tetrahedral sites marked m in Fig. 10). However, the four states have equal spacings between the ground state, first degenerate excited states and the fourth state. It cannot explain the two energies 0.4 meV and 1.8 meV obtained from the ultrasonic data. Therefore a model with more than four tunnelling

sites is suggested. One should also be aware of the fact that the presence of an O or N interstitial defect severely changes the energetic levels of the surrounding potential tunnelling sites. The strength of the Nb-H or O-H interaction depends strongly on both the distance and crystal direction. This means specifically that energy differences will exist between the surrounding sites that cannot be transformed into each other by symmetry operations around O or N. In other words, one should be looking only for tunnelling sites that can be transformed into each other by point group symmetry operations around the trap center. Another important fact that should be taken into account is that the vibrational frequencies of the free hydrogen are similar to those of the trapped hydrogen. Rush, et al.[17] suggest that the trapped hydrogen still occupies tetrahedral sites just like the free hydrogen, but only those tetrahedral sites not too close to the trap center, and the displaced two nearest neighbour Nb atoms. The sites thus suggested by them are shown in Fig. 10 marked q. However, the trapping of hydrogen by oxygen means that there must be an appreciable interaction between hydrogen and oxygen. Under the effect of trapping, any regular tetrahedral sites will not have the same potential property. Furthermore, channeling experiments on the TaNxDy system[2] have suggested a trapping site in between a tetrahedral and an octahedral site. The system is very similar to the Nb-O-H or Nb-N-H system, therefore it seems inappropriate to us to suggest that the trapped hydrogen still occupies a tetrahedral site.

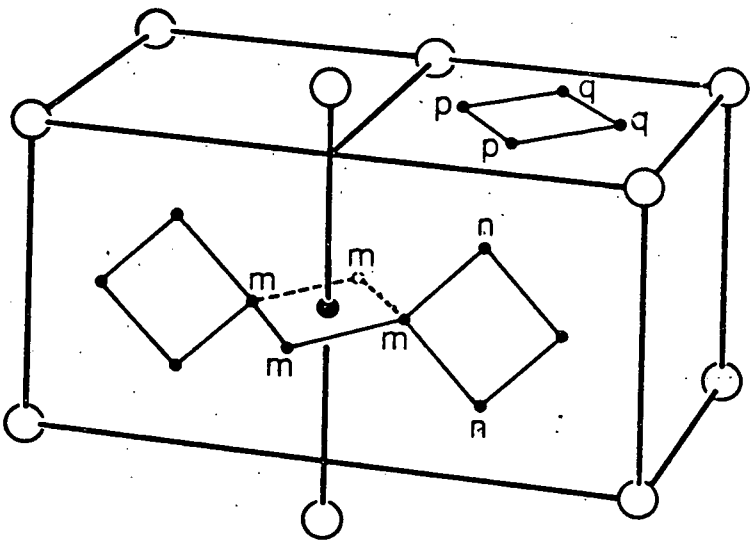

Figure 10. Schematic representation of the tetrahedral sites near an octahedral site occupied by oxygen. The four nearest neighbor tetrahedral sites around the oxygen are marked m. The second nearest neighbor tetrahedral sites are marked n. The trapping sites suggested by Rush, et al.[17] are marked q. Wipf and Neumaier[19] suggest a two-state tunnelling model, using the two sites marked p or the two marked q.

III. AN EIGHT STATE MODEL

1. The Eight Tunnelling States

A model of eight equivalent tunnelling sites, with none of them being a tetrahedral site, is proposed here to account for all the available experimental data. With the facts that more than four equivalent connected tunnelling sites are required and that the nearest Nb atoms are heavily displaced, one can start to search for models. If one looks only for symmetrically equivalent sites, it is impossible to find a tunnelling system with more than four equivalent and connected tetrahedral sites. The four nearest neighbour tetrahedral sites around the oxygen are the best one can find. But if one takes into account the fact that the two niobium atoms which are nearest neighbours of the oxygen are heavily displaced and that some electronic repulsive interaction between the oxygen and hydrogen exists, it is not so hard to imagine that the potential minima for these four tetrahedral sites may be removed, and two new potential minima are created in the neighbourhood of each of the four tetrahedral sites. The postulated eight new sites, located at the eight corners of a box, are shown in Fig. 11 and Fig. 12. One then can assume that hydrogen can tunnel through these eight sites.

Since tunnelling is very sensitive to the distance between two tunnelling sites, it is assumed that only tunnelling along paths approximated by the box edges is possible, and tunnelling across the box faces or along a body diagonal is prohibited.

From a symmetry point of view, two tunneling matrix elements are needed to describe the tunnelling system, with the first one α for tunnelling between

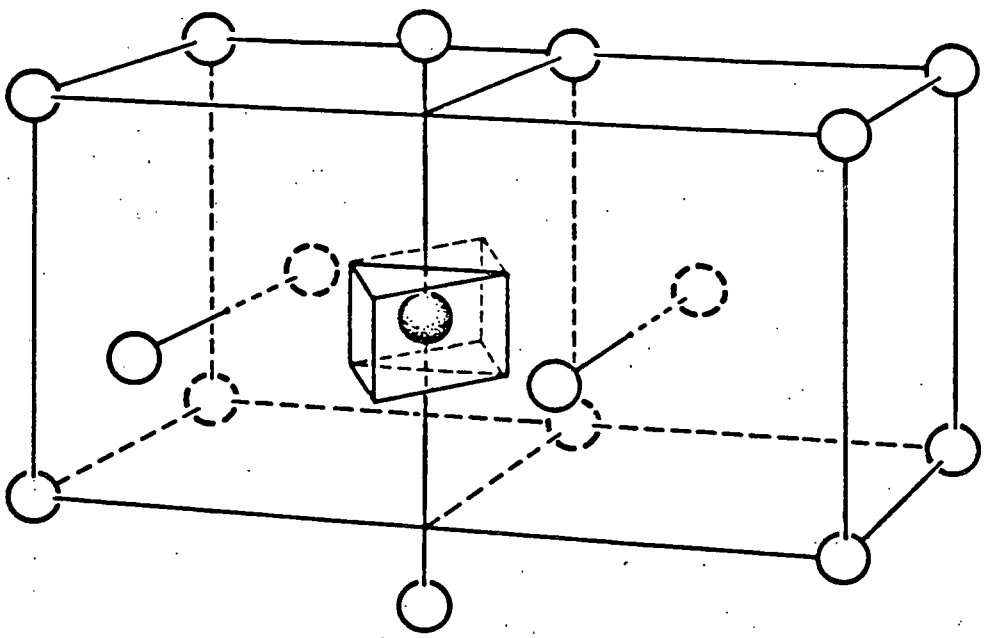

Figure 11. Schematic representation of the tunnelling sites for a hydrogen trapped by oxygen on an octahedral site in a Nb lattice. The eight sites are located at the eight corners of the box. The two nearest neighbor niobium atom with respect to the oxygen are heavily displaced.

Nb host lattice atoms

Oxygen trap center

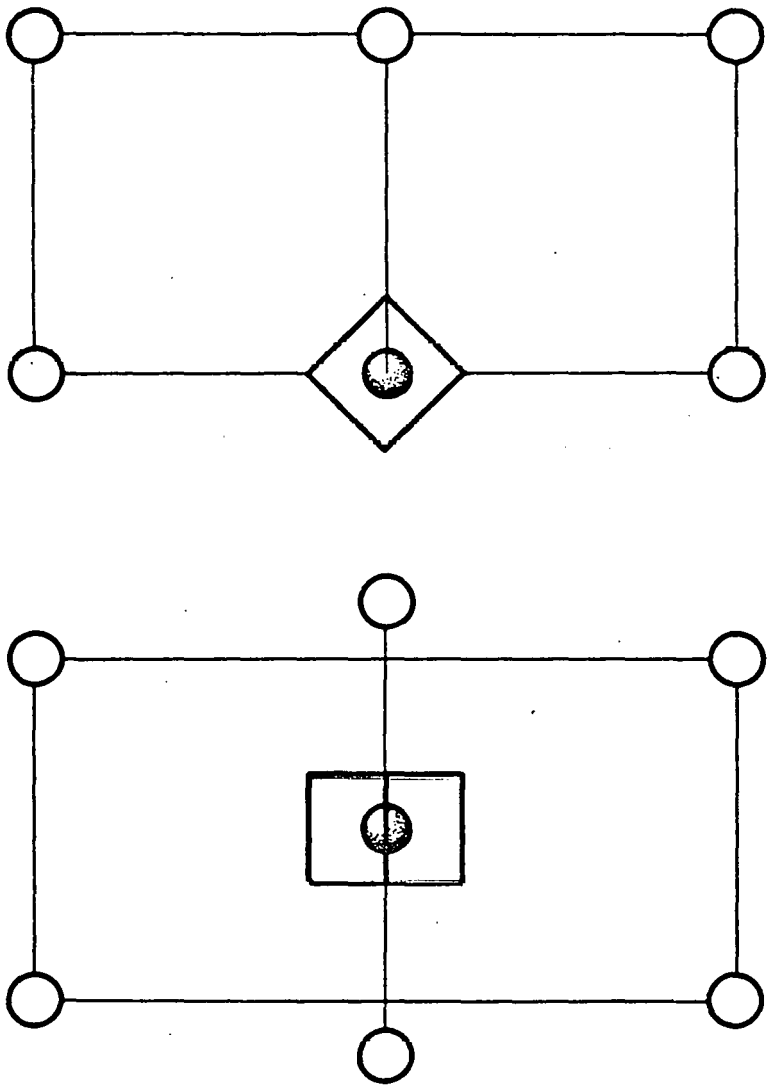

Figure 12. The top view and side view of Figure 11.

adjacent horizontal sites and the second one β for tunnelling between adjacent vertical sites. Shown in Fig. 13 are the eight tunnelling sites labeled a, b, c, d, e, f, g and h. If the overlaps of the adjacent localized wave functions of the wells are small enough, approximate solutions can be found for the eight tunnelling levels of the system in terms of linear combinations of the ground level local wave functions a, b, c, d, e, f, g, h. A matrix can be established and the problem is reduced to solving the secular equation shown below:

$$\begin{vmatrix} -E & \alpha & 0 & \alpha & \beta & 0 & 0 & 0 \\ \alpha & -E & \alpha & 0 & 0 & \beta & 0 & 0 \\ 0 & \alpha & -E & \alpha & 0 & 0 & \beta & 0 \\ \alpha & 0 & \alpha & -E & 0 & 0 & 0 & \beta \\ \beta & 0 & 0 & 0 & -E & \alpha & 0 & \alpha \\ 0 & \beta & 0 & 0 & \alpha & -E & \alpha & 0 \\ 0 & 0 & \beta & 0 & 0 & \alpha & -E & \alpha \\ 0 & 0 & 0 & \beta & \alpha & 0 & \alpha & -E \end{vmatrix} = 0 \qquad (1)$$

The eight levels are

$$\begin{aligned} E_{1,4} &= -\beta \mp 2\alpha \\ E_{2,3} &= -\beta \\ E_{5,8} &= \beta \mp 2\alpha \\ E_{6,7} &= \beta \end{aligned} \qquad (2)$$

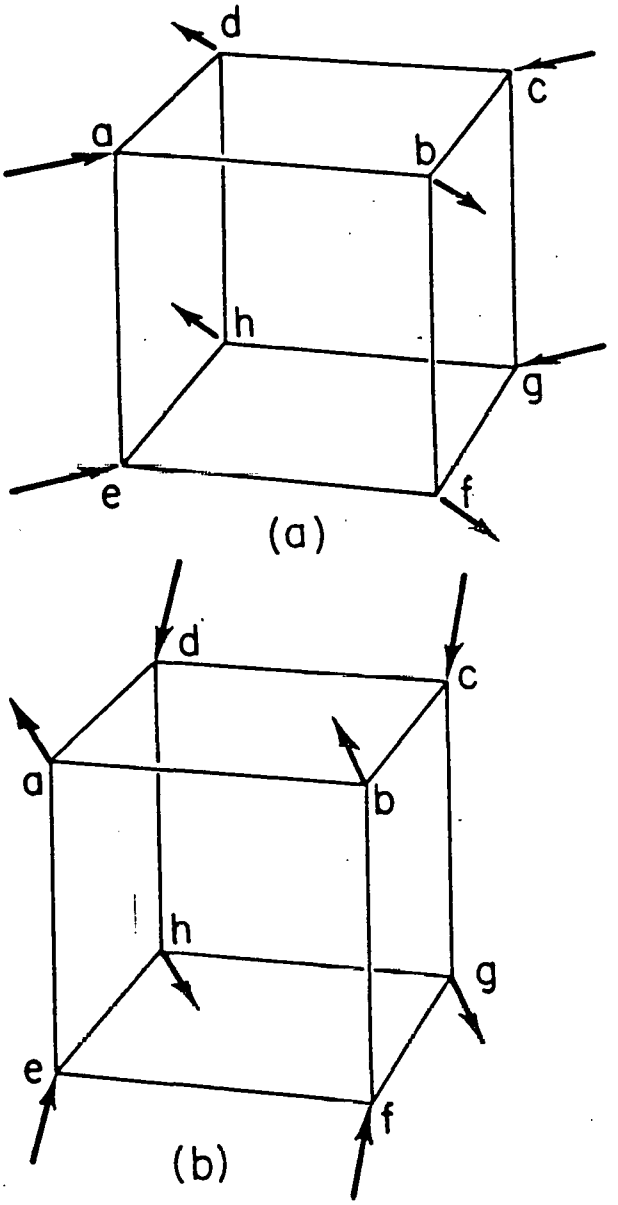

Figure 13. The eight tunnelling sites marked a,b,c,d,e,f,g,h. A C' strain represents pushing in along a [100] direction and pulling out along another [100] direction. It corresponds to pushing in along ac and eg, pulling out along bd and fh shown in (a). A C_{44} strain corresponds to pulling out along ah and bg, while pushing in along cf and de (b).

The wave functions can also be obtained

$$\psi_1 = \frac{1}{\sqrt{8}}(a + b + c + d + e + f + g + h)$$

$$\psi_2 = \frac{1}{2}(a - c + e - g)$$

$$\psi_3 = \frac{1}{2}(d - b + h - f)$$

$$\psi_4 = \frac{1}{\sqrt{8}}(a - b + c - d + e - f + g - h)$$

$$\psi_5 = \frac{1}{\sqrt{8}}(a + b + c + d - e - f - g - h) \qquad (3)$$

$$\psi_6 = \frac{1}{2}(a - c - e + g)$$

$$\psi_7 = \frac{1}{2}(b - d - f + g)$$

$$\psi_8 = \frac{1}{\sqrt{8}}(a - b + c - d - e + f - g + h) .$$

Some interesting features ought to be mentioned about the wave functions. Shown in Fig. 14 are the wave functions and the nodal planes. ψ_1, with no nodal planes, is the ground state. ψ_2 and ψ_3 are doubly degenerate, with one nodal plane; ψ_6 and ψ_7 are degenerate too, but with two nodal planes. The energy levels do not necessarily have the same order as they are numbered. Figure 15 shows the plot of E/β versus α/β. One can see that when $\beta = 0$,

$$E_1 = E_5 < E_{2,3} = E_{6,7} < E_4 = E_8 ,$$

when $\beta < \alpha$,

$$E_1 < E_5 < E_{2,3} < E_{6,7} < E_4 < E_8 ,$$

when $\beta > \alpha$

$$E_1 < E_{2,3} < E_4 < E_5 < E_{6,7} < E_8 .$$

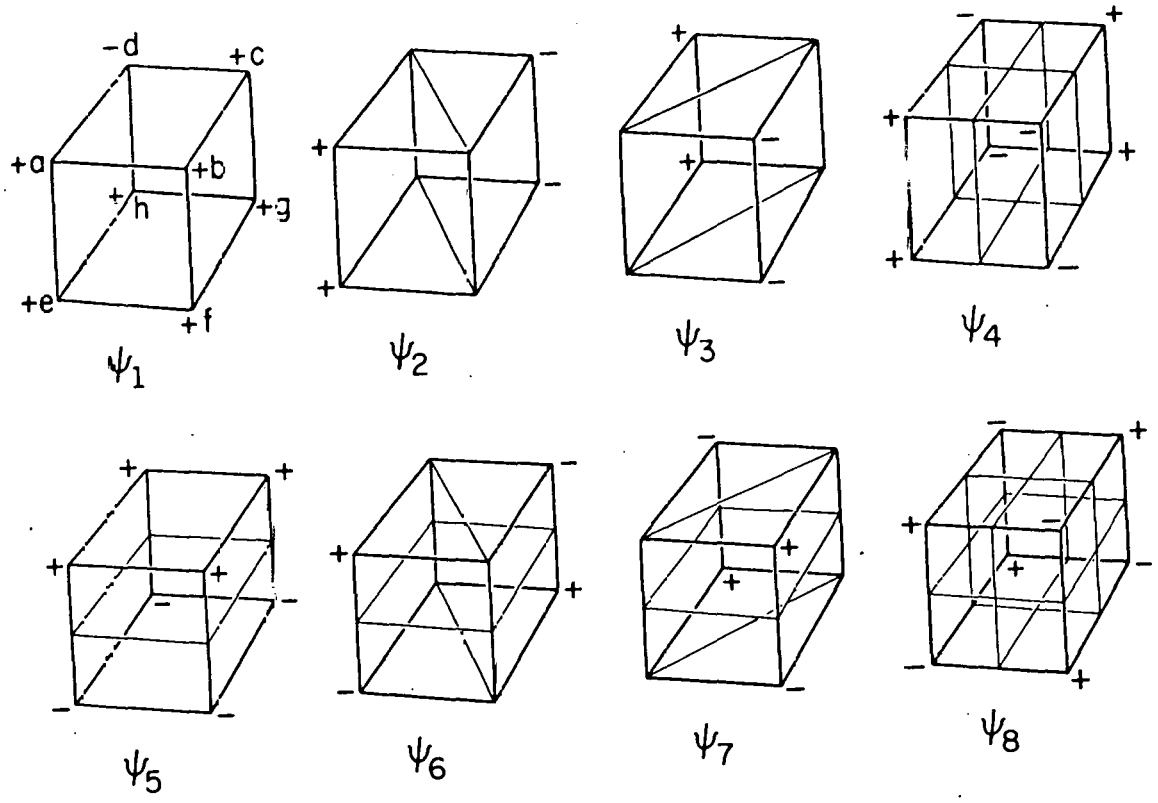

Figure 14. The wave functions of the eight tunnelling states as linear combinations of the ground level local wave functions, a,b,c,d,e,f,g,h. Also shown are the nodal planes of the wave functions. ψ_1 is the ground state with no nodal plane. ψ_2 and ψ_3 are degenerate with one vertical nodal plane. ψ_4 has two vertical nodal planes; ψ_5 has only one horizontal nodal plane. ψ_6 and ψ_7 are degenerate with one vertical nodal plane and one horizontal nodal plane. ψ_8 has three nodal planes.

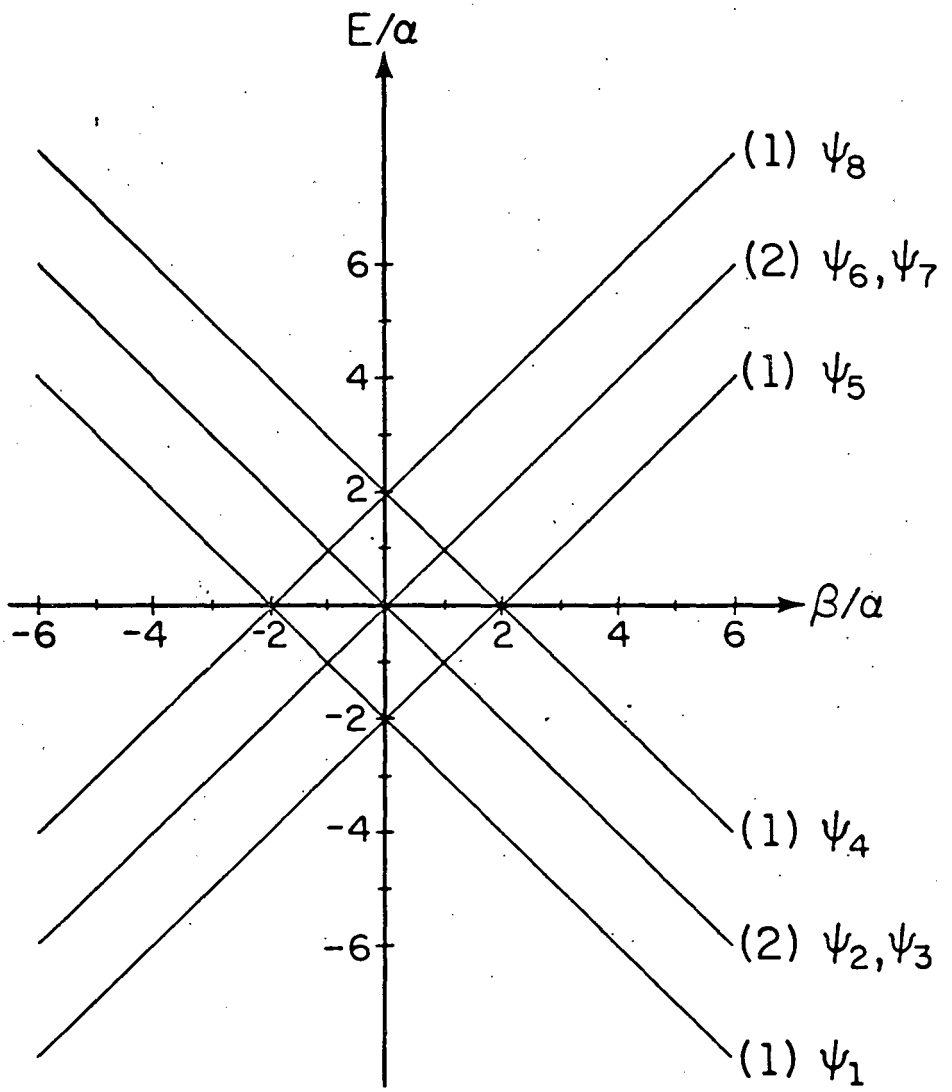

Figure 15. The eight energy levels normalized to α as a function of β/α. The energy levels do not necessarily have the same order as they are numbered. It depends mainly on whether $\beta > \alpha$ or $\beta < \alpha$. The number in parenthesis indicates the degeneracy of the energy level.

To obtain the strain dependence of these energy levels, one needs to know the strain lambda tensor, which represents the distortion of the lattice by the defect. The detailed calculation of strain interaction energy using a lambda tensor is given in the Appendix. However, one can also here use a simple symmetry argument to show the qualitative result of strain interactions. Shown in Fig. 13 are the typical C' type and C_{44} type strain. A C' type strain is pushing in along ac and eg, pulling out along bd and fh. One may assume that the energy levels of a, c, e, g will be raised by $\gamma\eta$ and those of b, d, f, h lowered by $\gamma\eta$, where η is the strength of the C' type strain and γ is the coupling constant. Similarly a C_{44} strain will raise the energy levels of c, d, e, f by $\gamma_{44}\eta_{44}$, and lower those of a, h, b, g by $\gamma_{44}\eta_{44}$. One can then get new secular equations by adding the energy changes in the diagonal elements of the matrix. Diagonalizing the matrix gives

$$\begin{aligned} E_{1,4} &= -\beta \mp [(2\alpha)^2 + \gamma^2\eta^2]^{1/2} \\ E_{2,3} &= -\beta \mp \gamma\eta \\ E_{5,8} &= \beta \mp [(2\alpha)^2 + \gamma^2\eta^2]^{1/2} \\ E_{6,7} &= \beta \mp \gamma\eta \end{aligned} \tag{4}$$

for a C' type strain.

The energy levels as a function of η and η_{44} are shown in Fig. 16 and Fig. 17, with $\beta > \alpha$. Shown in Fig. 18 are the energy levels as a function of η, but with $\alpha > \beta$. A notable feature of these energy levels is that a C' type strain splits the two degenerate levels linearly, while a C_{44} strain splits them quadratically.

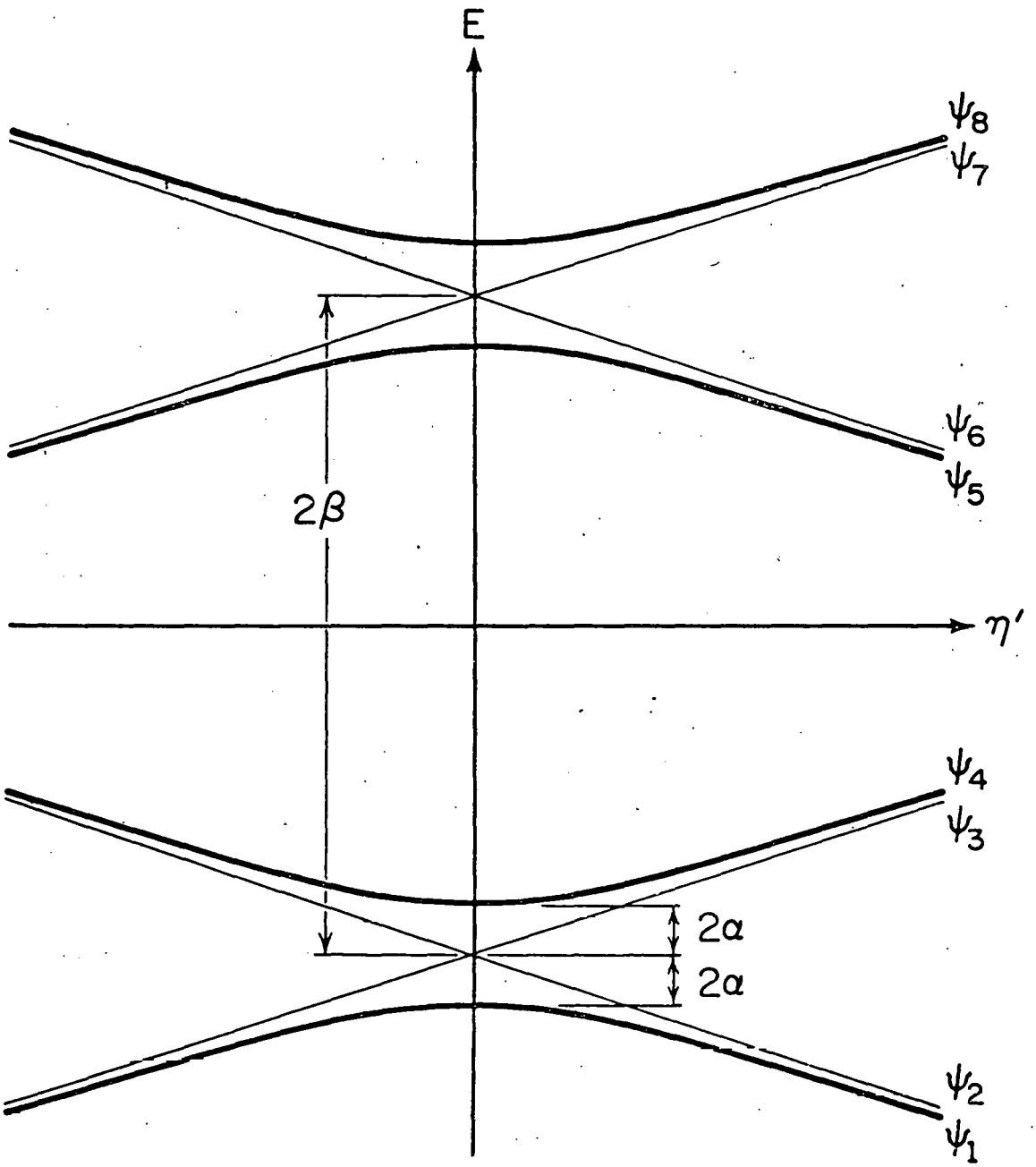

Figure 16. The energy levels of the eight-state model as a function of C' strain for $\beta > \alpha$. The two degenerate states split linearly when C' strain is applied. The energy difference between the ground state and the first excited states is 2α, which determines the temperature at which depopulation occurs. The energy difference between $\psi_{2,3}$ and ψ_5 is $2(\beta - \alpha)$, which determines the activation energy of the Orbach process.

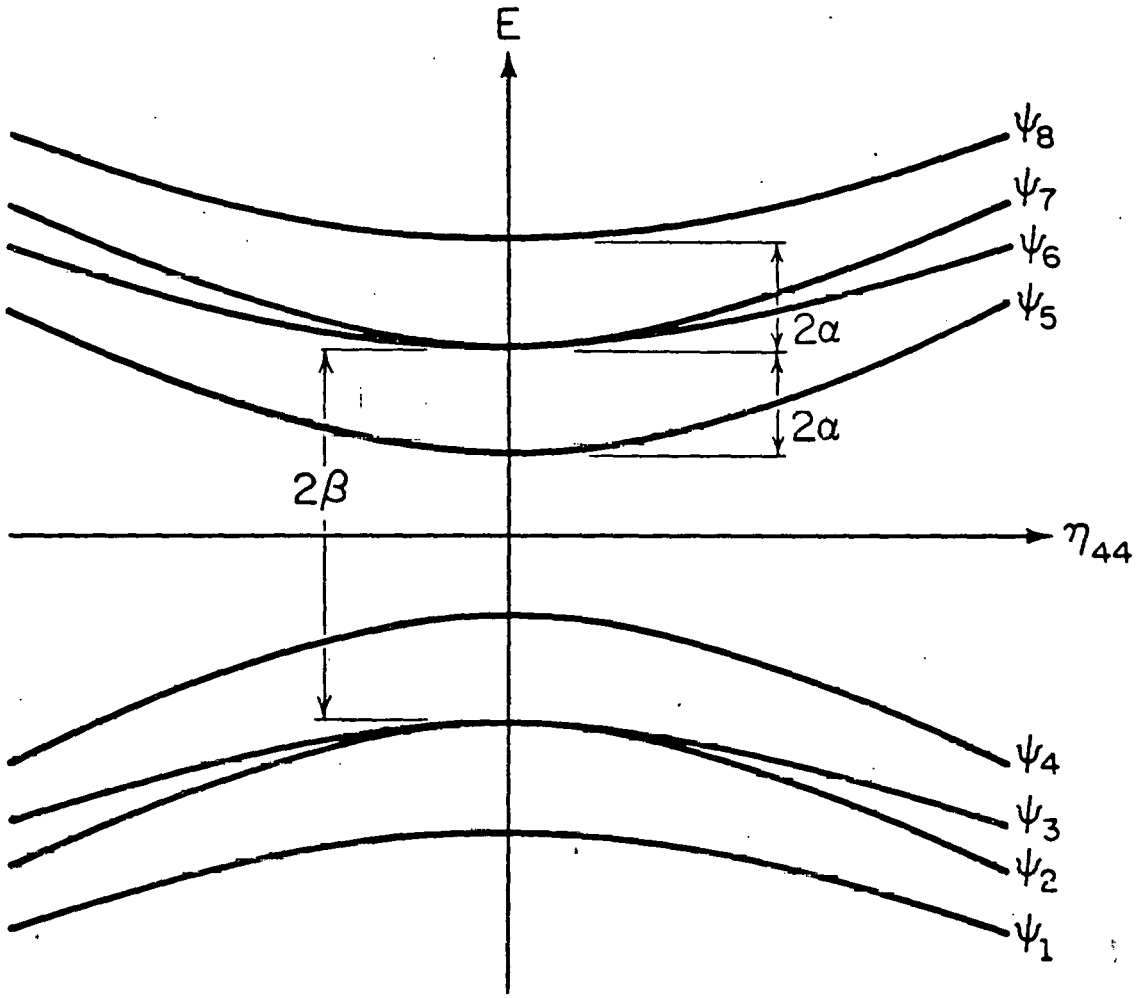

Figure 17. The energy levels as a function of C_{44} strain for $\beta > \alpha$. The two degenerate states split quadratically when an C_{44} strain is applied.

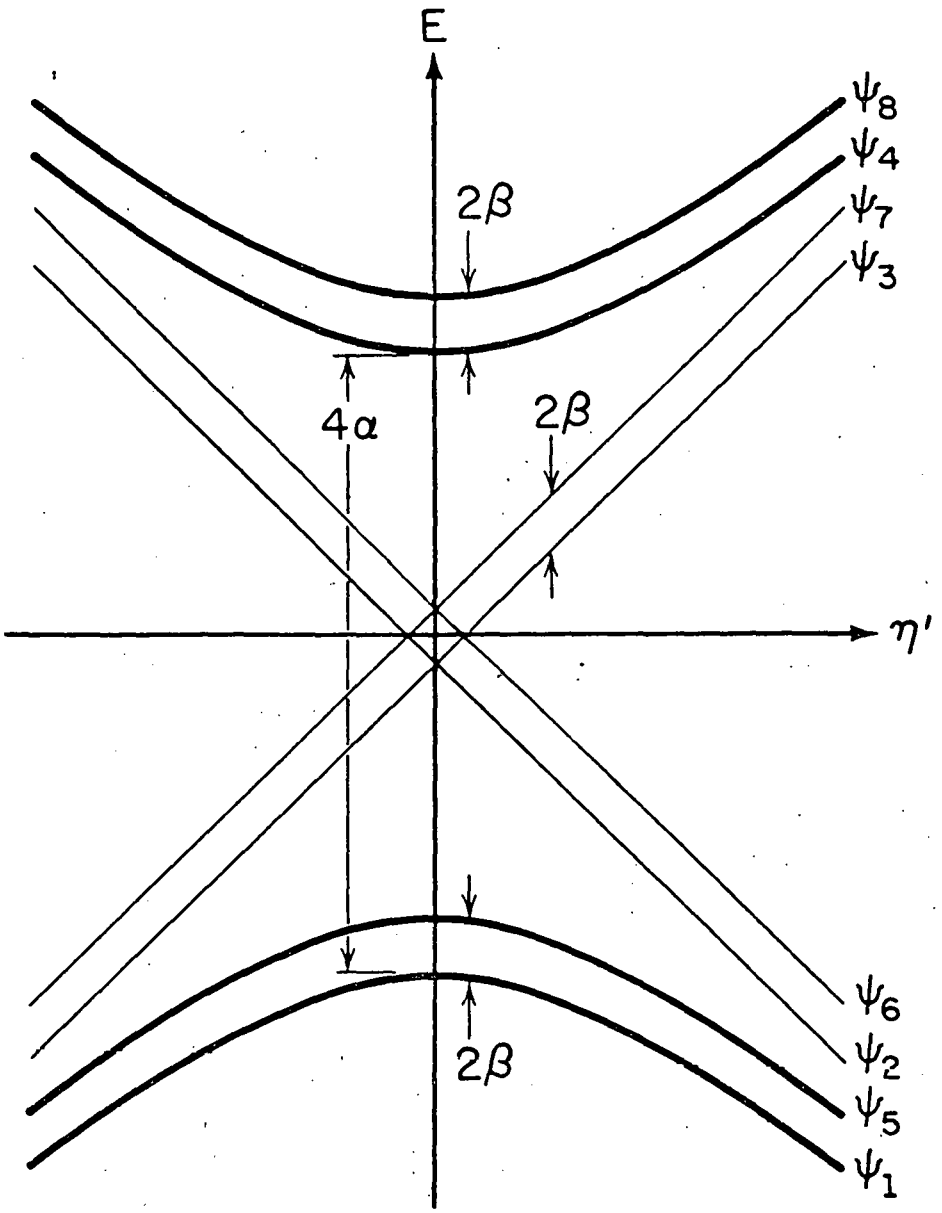

Figure 18. The energy levels as a function of C' strain for $\alpha > \beta$.

The matrix elements $\langle\psi_m|V|\psi_n\rangle$ between ψ_m and ψ_n through the interaction V (C' or C_{44}) can also be obtained. Shown in Fig. 19 are the possible couplings (with nonzero matrix elements) between the states through C' or C_{44}. One can see that $\psi_{2,3}$ couples only with ψ_5 and ψ_8 through C_{44}. ψ_1 couples to ψ_4 and ψ_4 to ψ_8 through C'. The matrix elements $\langle\psi_m|V|\psi_n\rangle$ between all states due to C' or C_{44} strain interaction are given in the Appendix.

With the energy levels as a function of strain known, a strain distribution is needed. However, there is not much known about how in the system the strain is distributed; one can assume a simple square distribution or a Lorentzian distribution. These distributions are shown in Fig. 20.

2. Specific Heat

The specific heat can be calculated from the eight energy levels using

$$C = \frac{d}{dT}[kT^2 \frac{d}{dT}(\ln Z)] \tag{5}$$

where $Z = \sum_{i=1}^{8} \exp(-E_i/kT)$ is the partition function. Here the energy levels as a function of C' strain are used. For small strains, this should be a good approximation. For a given strain η, the specific heat $C(\eta)$ is then

$$C(\eta) = k\left(\frac{\beta}{kT}\right)^2 \mathrm{Sech}^2\left(\frac{\beta}{kT}\right) + \frac{1}{kT^2}\frac{A(\eta) - B(\eta)}{D(\eta)} \tag{6}$$

where

$$A(\eta) = (4\alpha^2 + 2\gamma^2\eta^2)\left(1 + \mathrm{Cosh}\,\frac{\gamma\eta}{kT}\,\mathrm{Cosh}\,\frac{(4\alpha^2 + \gamma^2\eta^2)^{1/2}}{kT}\right)$$

$$B(\eta) = 2\gamma\eta(4\alpha^2 + \gamma^2\eta^2)^{1/2}\,\mathrm{Sinh}\,\frac{\gamma\eta}{kT}\,\mathrm{Sinh}\,\frac{(4\alpha^2 + \gamma^2\eta^2)^{1/2}}{kT}$$

$$D(\eta) = \left[\mathrm{Cosh}\,\frac{\gamma\eta}{kT} + \mathrm{Cosh}\,\frac{(4\alpha^2 + \gamma^2\eta^2)^{1/2}}{kT}\right]^2$$

The first term, which is independent of strain, is a Schottky specific heat.

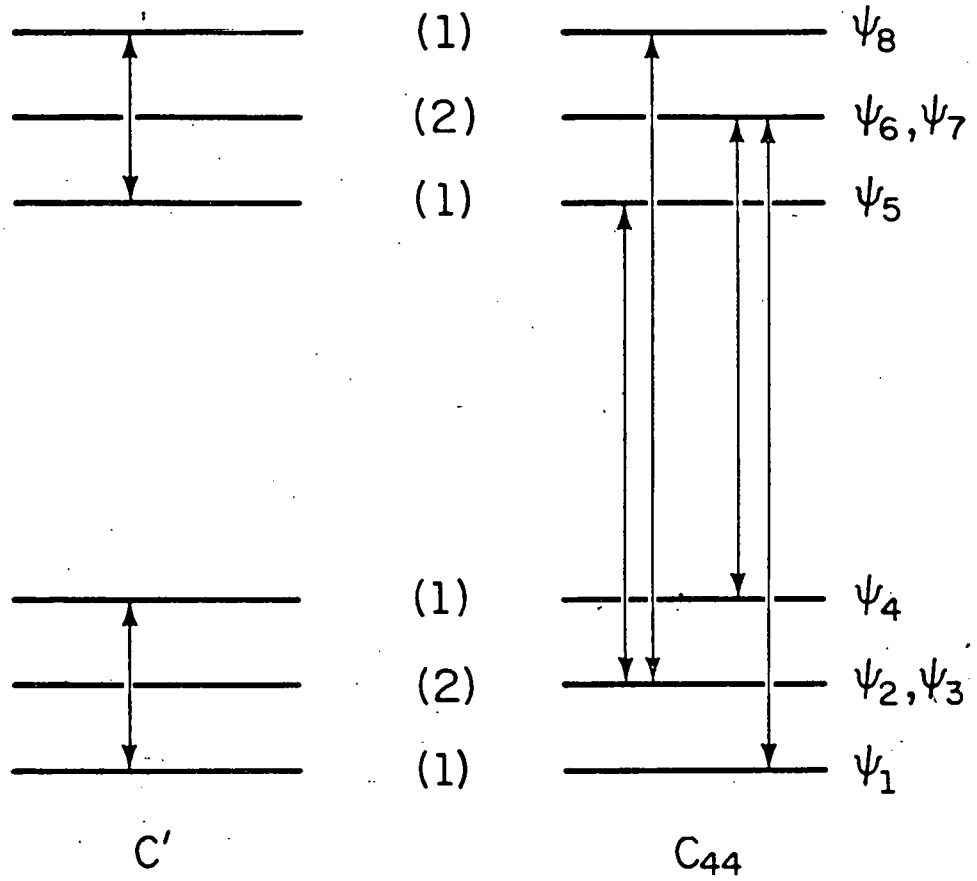

Figure 19. The states with non-zero matrix elements through C' or C_{44} mode. ψ_1 couples to ψ_4, ψ_5 to ψ_8 through C' phonons. $\psi_{2,3}$ couple to ψ_5 and ψ_8, $\psi_{6,7}$ to ψ_1 and ψ_4 through C_{44} phonons.

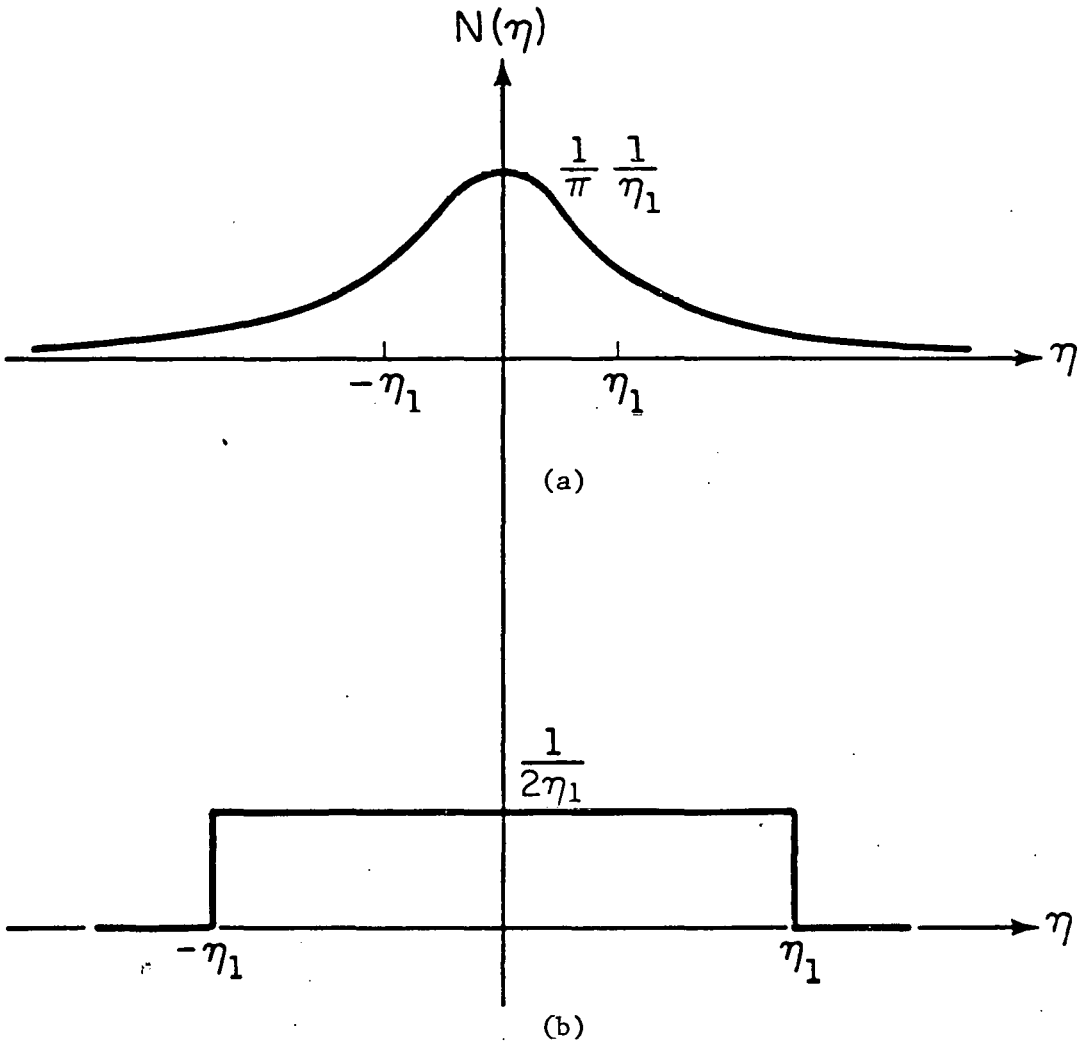

Figure 20. The Lorentzian strain distribution (a) and the square strain distribution (b).

It increases exponentially at low temperatures, then peaks at $T \simeq 0.42 \frac{2\beta}{k}$, and finally decreases as $1/T^2$. The second term is strain dependent. At zero strain, its behavior is similar to that of a Schottky specific heat. With a strain distribution, it broadens out and the peak gets smaller. The specific heat, under the consideration of a strain distribution $N(\eta) = \frac{1}{\pi} \frac{\eta_1}{\eta_1^2 + \eta^2}$, is

$$C(\eta) = C_{OH} \int N(\eta) C(\eta) d\eta \qquad (7)$$

where C_{OH} is the concentration of OH pairs.

A typical specific heat as a function of T and η_1 is shown in Fig. 21. It can be seen that the first term peaks around .25 K, while the second term peaks around 0.9 K. As a function of increasing η_1, the second term spreads out more and more, while the first term stays about the same. A comparison with the two-state model suggested by Wipf, et al.[19] is made here to demonstrate the main difference between the two models. Shown in Fig. 22 is the specific heat as a function of temperature and increasing η_1 predicted by the two-state model. It is worth noting that the low temperature specific heat is notably reduced as η_1 increases in the two state model, while it stays about the same in the eight-state model.

3. Ultrasonic Attenuation and Velocity

Before one begins to describe the possible transitions that can be predicted from this model, it is instructive to review two useful relaxation processes, the Orbach process[24] and the direct process.[25] The Orbach process involves the absorption and emission of two phonons with the system passing through a real intermediate eigenstate, while the direct process consists of only the absorption or emission of one phonon,

Figure 21. The specific heat as a function of temperature and increasing η_1 for the eight-state system. The first term (a Schottky specific peak), which is independent of strain, peaks around 0.25 K (β/k = 0.3 K). The second term, which is strain dependent, peaks around 0.9 K ($2\alpha/k$ = 1 K). Curve A represents zero strain. Curve B, C and D represent $\eta_1 = 1 \times 10^{-4}$, 5×10^{-4}, 1×10^{-3} respectively. The overall shape changes as a function of η_1.

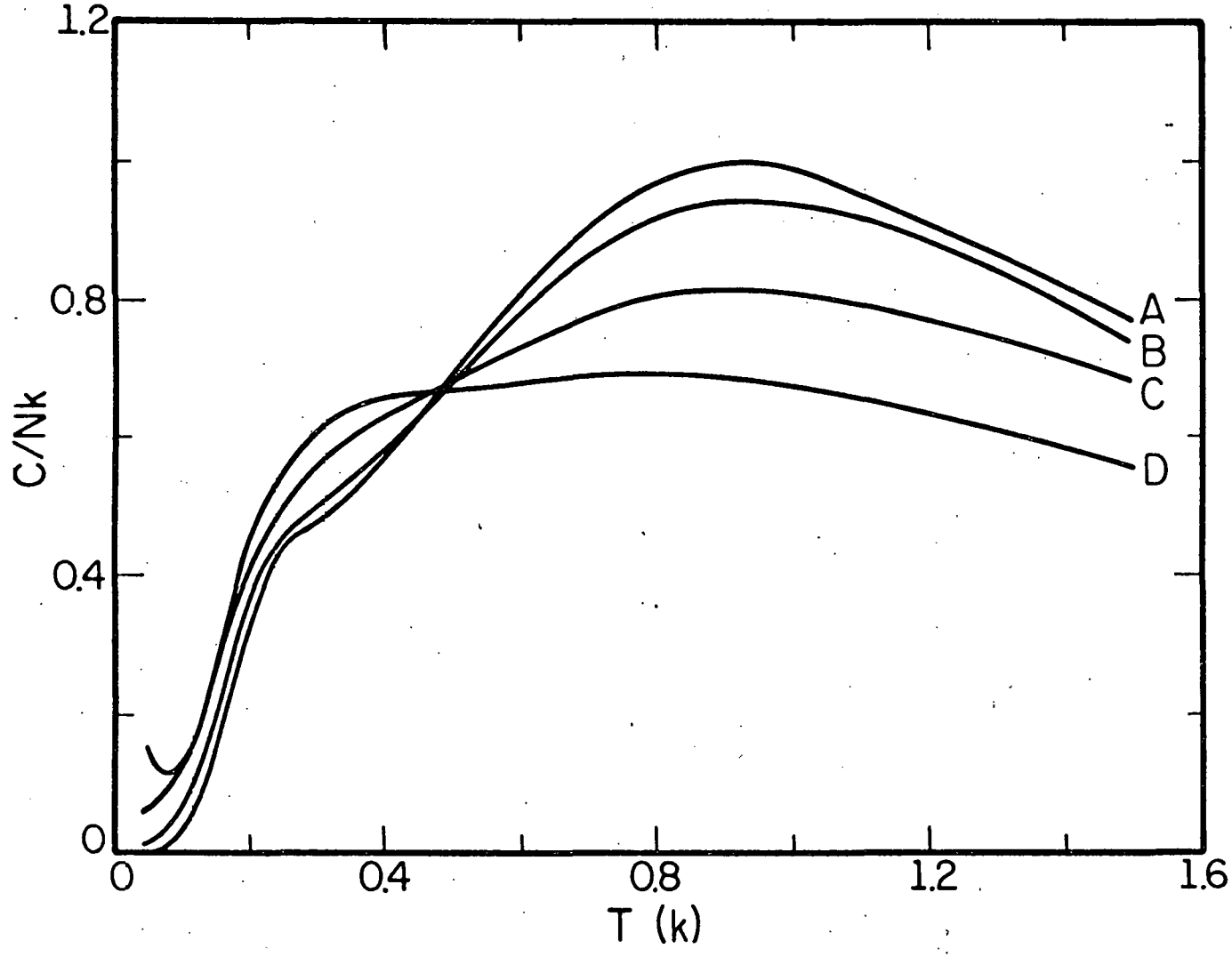
1.2
0.8
0.4
0
C/Nk
0
0.4
0.8
1.2
1.6
T (k)
A
B
C
D

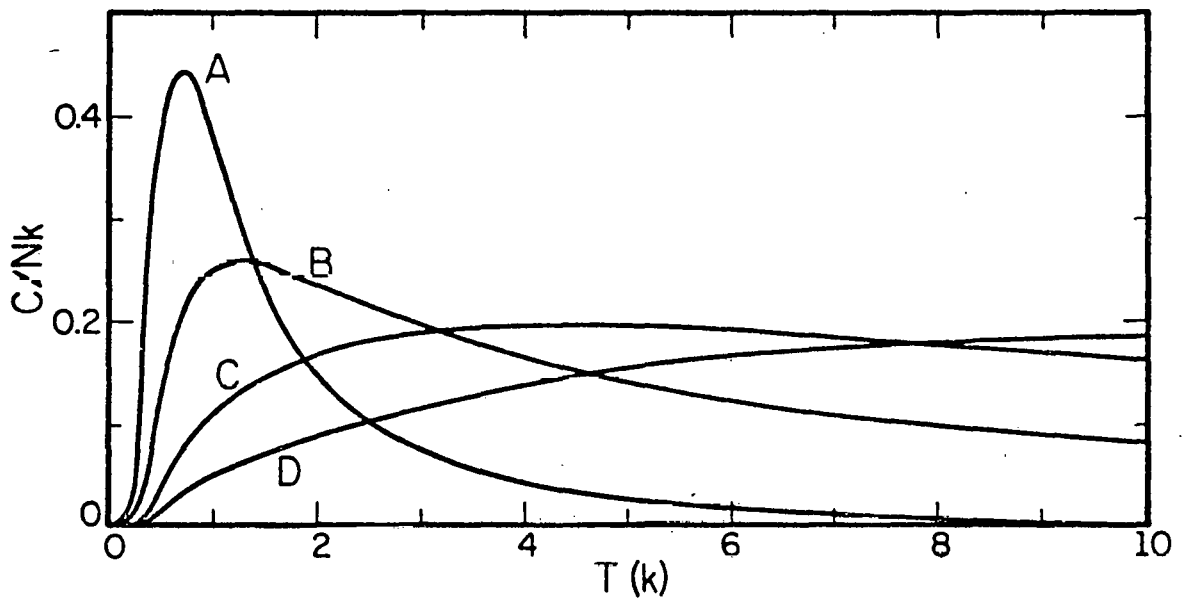

Figure 22. The specific heat as a function of temperature for the two state model proposed by Wipf and Neumaier.[19] Curve A represents the specific heat for zero bias strain and an energy gap $\Delta E/k = 1$ K, which is a Schottky specific heat. Curve B, C and D represent the specific heat for three different Lorentzian distributions. The broader the distribution is, the smaller the specific heat is at low temperatures.

with the system making a transition between two eigenstates. Both processes are shown schematically in Fig. 23. Hence if a transition between eigenstates A and C is desired, both processes can occur, but only the fast one dominating. The relaxation times for the two processes are given by

$$1/\tau_{Or} = A\,\Delta^3 |\langle A|V|B\rangle|^2 \,[\exp(\Delta/kT) - 1]^{-1} \tag{8}$$

$$1/\tau_{D} = A\,\delta^3 |\langle A|V|C\rangle|^2 \,\mathrm{Coth}\,\frac{\delta}{2kT} \tag{9}$$

$$A = \frac{3}{2\pi\rho\hbar^4 v^5}$$

where τ_{Or} and τ_{D} are the relaxation times for the Orbach process and the direct process respectively, $\hbar$ is Planck's constant, ρ is the density of the solid, v is the velocity of sound in the solid and k is Boltzmann's constant, Δ and δ are the energy differences shown in Fig. 23. The term $\langle A|V|C\rangle$ represents the matrix element between the states A and C caused by the interaction V due to the phonon strain field. (For the Orbach process, $\langle A|V|B\rangle = \langle A|V|C\rangle$ has been assumed.) At low temperatures, the relaxation time for the Orbach process has the form

$$1/\tau_{Or} = A\,\Delta^3 |\langle A|V|B\rangle|^2 \exp(-\frac{\Delta}{kT}) \tag{10}$$

which has the appearance of a thermally activated process, while the relaxation time for the direct process has the form

$$1/\tau_{D} = A\,\delta^3 |\langle A|V|C\rangle|^2 \,(\frac{2k}{\delta})\,T \tag{11}$$

which depends on temperature linearly.

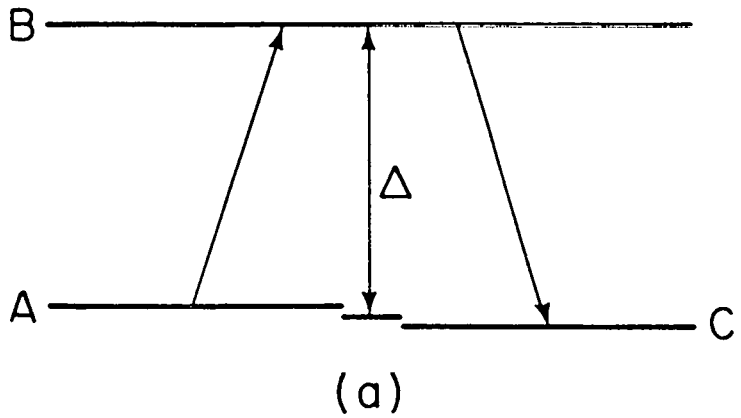

(a)

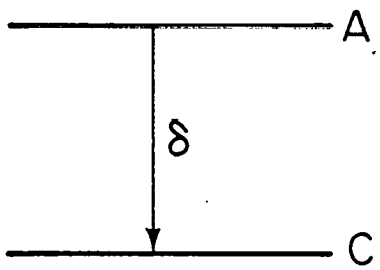

(b)

Figure 23. (a) The Orbach process. The transition occurs by the absorption of a phonon with the transition from state A to state B, followed by the emission of a phonon with the transition from state B to state C. The relaxation time has an exponential temperature dependence with an activation energy Δ.

(b) The direct process. The transition occurs by the emission of a phonon with the transition from state A to state C. The relaxation time has a linear temperature dependence at low temperatures.

From the energy diagram and the coupling between the states, it is possible to identify all the relaxation processes that can be predicted by the model. First of all, the C' strain lifts the degeneracy of the first excited states, so that repopulation of the states is expected. Since these states are not coupled to each other, a direct process is not allowed. However, they do couple to E_5 and E_8 through a C_{44} mode, so that an Orbach process can occur. The relaxation time is

$$1/\tau = A\left(\frac{\gamma_{44}}{\sqrt{2}}\right)^2 \left[\Delta_1^3 \exp(-\Delta_1/kT) + \Delta_2^3 \exp(-\Delta_2/kT)\right] \tag{12}$$

where

$$\Delta_1 = E_5 - E_2 = 2(\beta - \alpha)$$

$$\Delta_2 = E_8 - E_2 = 2(\beta + \alpha)$$

$$\langle\psi_2|H_{44}|\psi_5\rangle = \langle\psi_2|H_{44}|\psi_8\rangle = \frac{\gamma_{44}}{\sqrt{2}} \qquad \text{(see the Appendix)}$$

Transitions can occur through two intermediate states E_5 and E_8, but only the faster one will dominate at each temperature.

The decrement Δ and the elastic constant change are given by the Debye equations,

$$\frac{\Delta}{\pi} = \Delta_R \frac{\omega\tau}{1 + \omega^2\tau^2}$$

$$\frac{\Delta C}{C} = \Delta_R \frac{1}{1 + \omega^2\tau^2} \tag{13}$$

where Δ_R is the relaxation strength, and ω is the angular frequency applied. A Debye peak is expected in the decrement at $\omega\tau = 1$.

The other possible transition is between E_1 and E_4, or E_5 and E_8, through a direct process. These levels are flat for small strains, so that

no repopulation is expected. However for large internal strains, a direct process can still be expected. For two levels like $E_{1,4} = -\beta \mp (4\alpha^2 + \gamma^2\eta^2)^{1/2}$, the relaxation strength is given[26] by

$$\Delta_R(\eta) = \frac{1}{C}\left(\frac{\gamma^2}{kT}\right)\frac{\gamma^2\eta^2}{(4\alpha^2 + \gamma^2\eta^2)}\,\mathrm{Sech}^2\,\frac{(4\alpha^2 + \gamma^2\eta^2)^{1/2}}{kT} \tag{14}$$

where C is the appropriate elastic constant. The relaxation time for this direct process is

$$1/\tau_D = 8kA\,\left|\langle\psi_1|H'|\psi_4\rangle\right|^2(4\alpha^2 + \gamma^2\eta^2)T \tag{15}$$

$\langle\psi_1|H'|\psi_4\rangle$ can be shown to have the form

$$\langle\psi_1|H'|\psi_4\rangle = \frac{2\alpha\gamma}{(4\alpha^2 + \gamma^2\eta^2)^{1/2}} \tag{16}$$

$$\therefore\quad 1/\tau_D = 32kA\,\alpha^2\gamma^2\,T \equiv BT \tag{17}$$

with $\quad B \equiv 32kA\,\alpha^2\gamma^2$

Hence the decrement and the elastic constant change can be expressed as

$$\Delta(\eta) = \pi\Delta_R(\eta)\,\frac{\omega\tau}{1 + \omega^2\tau^2}$$

$$\frac{\Delta C(\eta)}{C} = \Delta_R(\eta)\,\frac{1}{1 + \omega^2\tau^2} \tag{18}$$

With a strain distribution $N(\eta)$, one can calculate the decrement and the elastic constant change

$$\frac{\Delta}{\pi} = \frac{\omega\tau}{1+\omega^2\tau^2}\int N(\eta)\Delta_R(\eta)d\eta$$

$$\frac{\Delta C}{C} = \frac{1}{1+\omega^2\tau^2}\int N(\eta)\Delta_R(\eta)d\eta \tag{19}$$

The integral $\int N(\eta)\Delta_R(\eta)d\eta$ can be done numerically, if the strain distribution function is known. However, one can also know the qualitative behavior of the decrement and the elastic constant change by making some approximations.

First of all, Δ_R in Equation 14 can be approximated by

$$\Delta_R(\delta) = \begin{cases} 0 & kT < \delta \\ \frac{1}{C}\frac{\gamma^2}{kT}\frac{(\delta^2 - 4\alpha^2)}{\delta^2} & kT > \delta \end{cases} \tag{20}$$

where $\delta^2 = 4\alpha^2 + \gamma^2\eta^2$ is assumed.

Secondly a simple square strain distribution function

$$N(\eta) = \begin{cases} 0 & |\eta| > \eta_1 \\ \frac{1}{2\eta_1} & |\eta| > \eta_1 \end{cases} \tag{21}$$

is used. A corresponding distribution function $N(\delta)$ can be expressed as

$$N(\delta) = \frac{\delta}{\gamma\eta_1(\delta^2 - 4\alpha^2)^{1/2}} \qquad 2\alpha < \delta < (\gamma^2\eta_1^2 + 4\alpha^2)^{1/2} \equiv \delta_1 \tag{22}$$

The integral then can be evaluated in three regimes:

(a) $kT < 2\alpha$

For all $\delta > 2\alpha > kT$ $\quad \Delta_R = 0$

Therefore, $\int N(\delta)\Delta_R d\delta = 0$

(b) $2\alpha < kT < \delta_1 = (\gamma^2\eta^2 + 4\alpha^2)^{1/2}$

For $\delta > kT$ $\quad \Delta_R = 0$

Therefore, $$\int_{2\alpha}^{\delta_1} N(\delta)\Delta_R d\delta = \int_{2\alpha}^{kT} \frac{1}{C}\frac{\gamma^2}{kT}\frac{(\delta^2 - 4\alpha^2)}{\delta^2}\frac{\delta d\delta}{\gamma\eta_1(\delta^2 - 4\alpha^2)^{1/2}}$$

$$= \frac{1}{C}\frac{\gamma}{kT\eta_1}\int_{2\alpha}^{kT}\frac{(\delta^2 - 4\alpha^2)^{1/2}}{\delta}\,d\delta$$

$$= \frac{1}{C}\frac{\gamma}{kT\eta_1}\left[(k^2T^2 - 4\alpha^2)^{1/2} - 2\alpha\,\mathrm{Cos}^{-1}\left(\frac{2\alpha}{kT}\right)\right]$$

(c) $kT > \delta_1$

$$\int_{2\alpha}^{\delta_1} N(\delta)\Lambda_R\,d\delta = \frac{1}{C}\frac{\gamma}{kT\eta_1}\left[\gamma\eta_1 - 2\alpha\,\mathrm{Cos}^{-1}\left(\frac{2\alpha}{\delta_1}\right)\right]$$

One then can calculate the decrement and elastic constant change

$$\frac{\Delta}{\pi} = \begin{cases} 0 & kT < 2\alpha \\ \dfrac{\omega\tau}{1+\omega^2\tau^2}\dfrac{1}{C}\dfrac{\gamma}{\eta_1 kT}\left[(k^2T^2 - 4\alpha^2)^{1/2} - 2\alpha\,\mathrm{Cos}^{-1}\left(\dfrac{2\alpha}{kT}\right)\right] & 2\alpha < kT < \delta_1 \\ \dfrac{\omega\tau}{1+\omega^2\tau^2}\dfrac{1}{C}\dfrac{\gamma}{\eta_1 kT}\left[\gamma\eta_1 - 2\alpha\,\mathrm{Cos}^{-1}\left(\dfrac{2\alpha}{\delta_1}\right)\right] & kT > \delta_1 \end{cases} \quad (23)$$

$$\frac{\Delta C}{C} = \begin{cases} 0 & kT < 2\alpha \\ \dfrac{1}{1+\omega^2\tau^2}\dfrac{1}{C}\dfrac{\gamma}{\eta_1 kT}\left[(k^2T^2 - 4\alpha^2)^{1/2} - 2\alpha\,\mathrm{Cos}^{-1}\left(\dfrac{2\alpha}{kT}\right)\right] & \alpha < kT < \delta_1 \\ \dfrac{1}{1+\omega^2\tau^2}\dfrac{1}{C}\dfrac{\gamma}{\eta_1 kT}\left[\gamma\eta_1 - 2\alpha\,\mathrm{Cos}^{-1}\left(\dfrac{2\alpha}{\delta_1}\right)\right] & kT > \delta_1 \end{cases} \quad (24)$$

Two cases $\omega\tau >> 1$ and $\omega\tau << 1$ are considered.

(1) $\omega\tau >> 1$

$$\frac{\omega\tau}{1 + \omega^2\tau^2} = \frac{1}{\omega\tau} = \frac{BT}{\omega} \qquad (1/\tau = BT)$$

$$\frac{1}{1 + \omega^2\tau^2} = \frac{1}{\omega^2\tau^2} = \frac{B^2T^2}{\omega^2}$$

$$\frac{\Delta}{\pi} = \begin{cases} 0 & kT < 2\alpha \\ \frac{1}{C}\frac{\gamma B}{\eta_1 k\omega}\left[(k^2T^2 - 4\alpha^2)^{1/2} - 2\alpha\ \mathrm{Cos}^{-1}\left(\frac{2\alpha}{kT}\right)\right] & 2\alpha < kT < \delta_1 \\ \frac{1}{C}\frac{\gamma B}{\eta_1 k\omega}\left[\gamma\eta_1 - 2\alpha\ \mathrm{Cos}^{-1}\left(\frac{2\alpha}{\delta_1}\right)\right] & kT > \delta_1 \end{cases} \quad (25)$$

$$\frac{\Delta C}{C} = \begin{cases} 0 & kT < 2\alpha \\ \frac{1}{C}\frac{\gamma B^2 T}{\eta_1 k\omega^2}\left[(k^2T^2 - 4\alpha^2)^{1/2} - 2\alpha\ \mathrm{Cos}^{-1}\left(\frac{2\alpha}{kT}\right)\right] & 2\alpha < kT < \delta_1 \\ \frac{1}{C}\frac{\gamma B^2 T}{\eta_1 k\omega^2}\left[\gamma\eta_1 - 2\alpha\ \mathrm{Cos}^{-1}\left(\frac{2\alpha}{\delta_1}\right)\right] & kT > \delta_1 \end{cases} \quad (26)$$

(2) $\omega\tau << 1$

$$\frac{\omega\tau}{1 + \omega^2\tau^2} = \omega\tau = \frac{\omega}{BT}, \qquad \frac{1}{1 + \omega^2\tau^2} = 1 \quad \text{then}$$

$$\frac{\Delta}{\pi} = \begin{cases} 0 & kT < 2\alpha \\ \frac{1}{C}\frac{\gamma\omega}{\eta_1 kBT^2}\left[(k^2T^2 - 4\alpha^2)^{1/2} - 2\alpha\ \mathrm{Cos}^{-1}\left(\frac{2\alpha}{kT}\right)\right] & 2\alpha < kT < \delta_1 \\ \frac{1}{C}\frac{\gamma\omega}{\eta_1 kBT^2}\left[\gamma\eta_1 - 2\alpha\ \mathrm{Cos}^{-1}\left(\frac{2\alpha}{\delta_1}\right)\right] & kT > \delta_1 \end{cases} \quad (27)$$

$$\frac{\Delta C}{C} = \begin{cases} 0 & kT < 2\alpha \\ \frac{1}{C}\frac{\gamma}{\eta_1 kT}\left[(k^2T^2 - 4\alpha^2)^{1/2} - 2\alpha\ \mathrm{Cos}^{-1}\left(\frac{2\alpha}{kT}\right)\right] & 2\alpha < kT < \delta \\ \frac{1}{C}\frac{\gamma}{\eta_1 kT}\left[\gamma\eta_1 - 2\alpha\ \mathrm{Cos}^{-1}\left(\frac{2\alpha}{\delta_1}\right)\right] & kT > \delta_1 \end{cases} \quad (28)$$

It can be seen that, when $\omega\tau >> 1$, Δ behaves like a step function. Δ is zero for $0 \leq kT \leq 2\alpha$, then increases almost linearly with T until $kT = \delta_1$, then keeps constant for a long range of temperature until $\omega\tau \simeq 1$. At $\omega\tau = 1$ the decrement drops to half of the maximum. The elastic constant change is zero until the temperature reaches $2\alpha/k$, then decreases as T^2 until $T = \delta_1/k$, then decreases slowly as T. A similar discussion can be applied to the case when $\omega\tau << 1$. One can know how the decrement and elastic constant change behave from the simple square strain distribution. However, a more practical strain distribution like a Lorentzian distribution ought to be used. But the general features of the behavior will not change much, with only the discontinuity due to the square distribution smoothed out. Shown in Fig. 24 is a plot of decrement as a function of temperature for $\omega\tau >> 1$ and $\omega\tau << 1$, with the solid line for a square strain distribution and dotted line for a Lorentzian distribution. The η_1 for both distributions are chosen so that the two curves look alike.

There is another contribution to the elastic constant change which is from the second derivative of the curved states with respect to the strain. Since this contribution does not involve any repopulation between eigenstates, there would not be any decrement change associated with elastic constant change. For a two state system, this non-relaxing part has a 1/T temperature dependence.[26] Shown in Fig. 25 is a plot of the elastic constant change as a function of temperature for $\omega\tau >> 1$. At low temperature, it behaves like 1/T. At $T = 2\alpha/k$, it starts to decrease as T^2 until $T = \delta_1/k$, then it decreases as T.

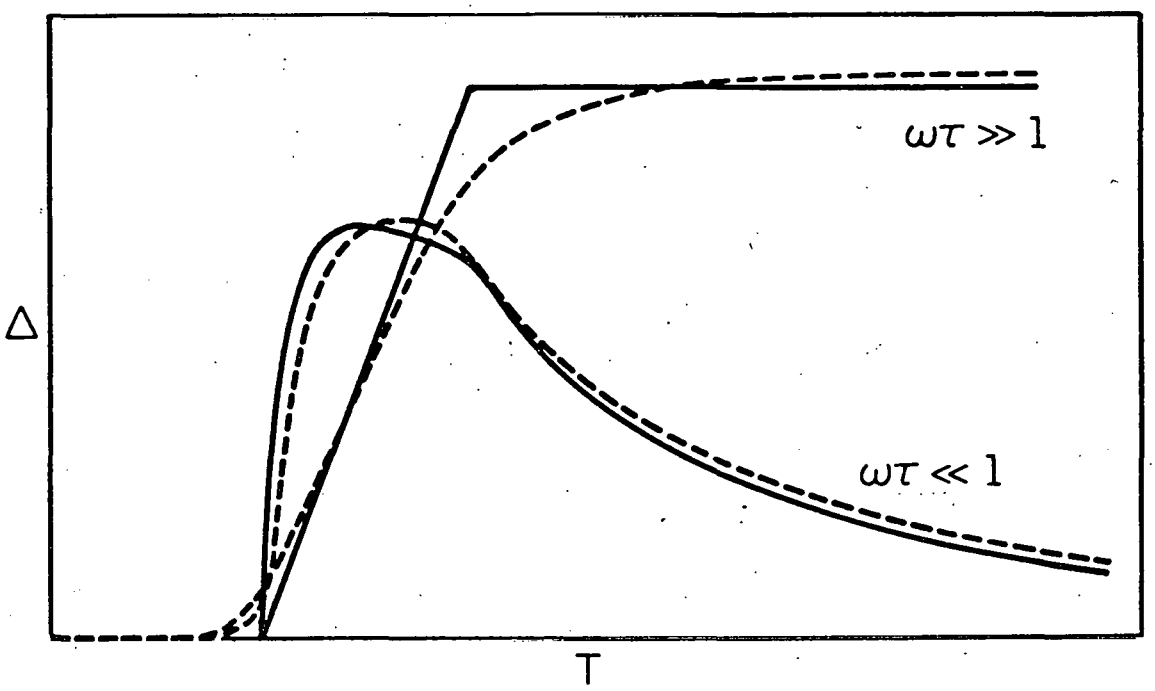

Figure 24. The decrement as a function of temperature for $\omega\tau >> 1$ and $\omega\tau << 1$. The solid curves represent the results for a square distribution and the dashed curves represent the results for a Lorentzian distribution.

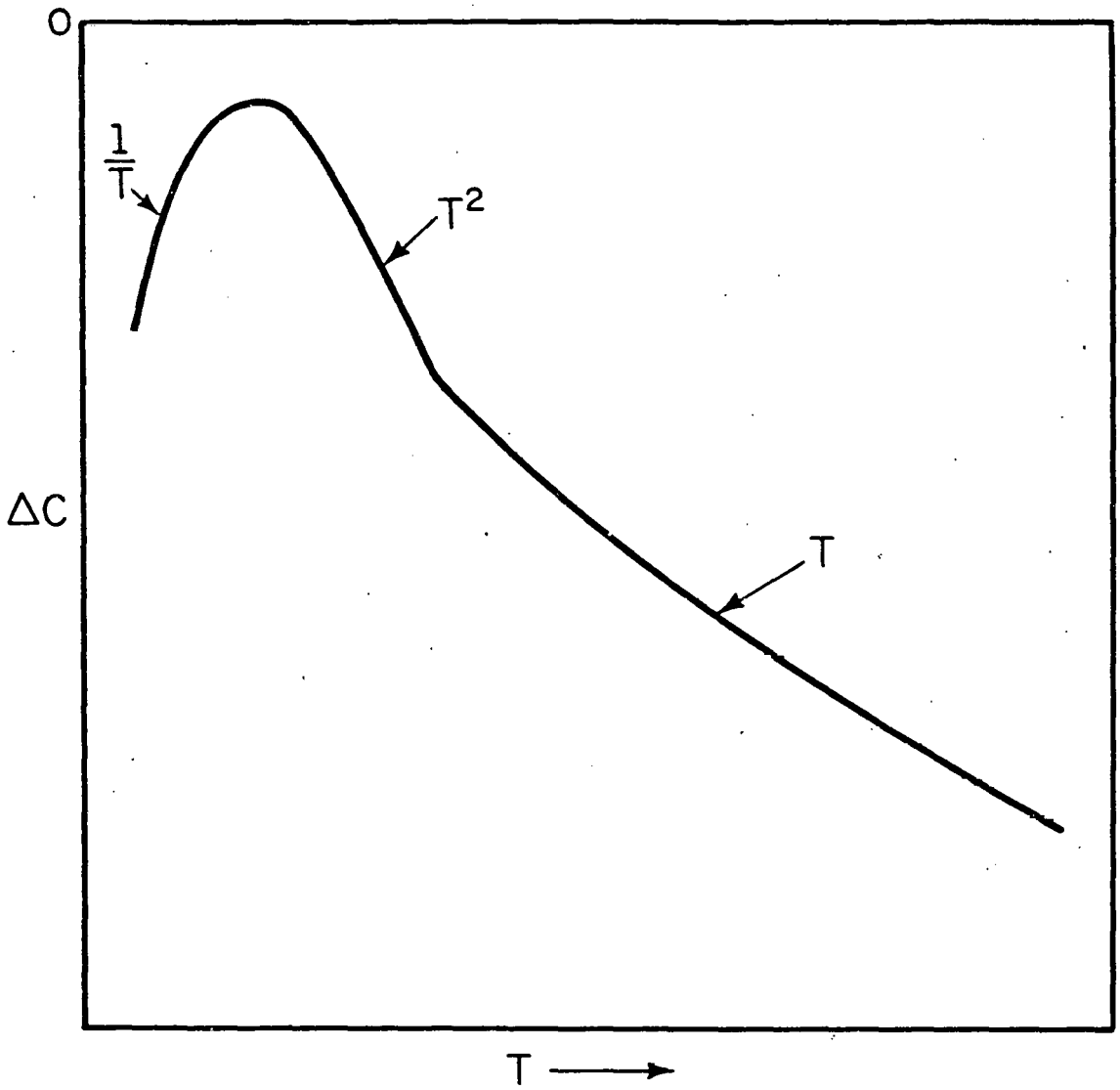

Figure 25. The general feature of the elastic constant change as a function of temperature for a direct process transition between two eigenstates. At low temperatures, ΔC has a $1/T$ temperature dependence arising from the curvature of the eigenstates. At the takeoff temperature $T = 2\alpha/k$, it decreases as T^2 until the temperature at which all the states are used up, then it decreases as T.

4. Vibrational Levels and Tunnelling Distances

With α and β given, one may estimate the tunnelling distances and the potential barriers. A one-dimensional approximation to the potential is assumed

$$V(x) = \frac{V_o}{2} \text{Cos}(\frac{2\pi x}{d}) \tag{29}$$

where d is the distance between two minima, V_o is the barrier. The frequency of a harmonic oscillator in one of the potential minima is given by

$$\omega^2 = 2\pi^2 V_o/md^2 \tag{30}$$

In the case of a deep potential $V_o >> h\omega$, the tunnelling matrix element is given by[27]

$$J = 8 \frac{\hbar^2}{2md^2} (\frac{2md^2V_o}{\hbar^2})^{3/4} \exp[-\frac{2}{\pi}(\frac{2md^2V_o}{\hbar^2})^{1/2}] \tag{31}$$

It can also be expressed as

$$J = \frac{4\hbar^2 d}{m} (\frac{m^2\omega^2}{\pi^2\hbar^2})^{3/4} \exp[-(\frac{2}{\pi})(\frac{m\omega}{\pi\hbar})d^2] \tag{32}$$

In the model, one will have the potential barriers V_a, V_b, tunnelling distances a, b and vibrational frequencies ω_a, ω_b for the α and β tunnelling matrix elements, respectively.

IV. INTERPRETATION AND PARAMETER DETERMINATION

1. Low Temperature Ultrasonic Results

The relaxation time of the hydrogen peak has an exponential temperature dependence, indicating that it is an Orbach process. The slope of the first excited state energy versus strain, γ, determines the relaxation strength. The energy difference between the ground state and the first excited states, δ, determines the temperature at which depopulation occurs, which affects the relaxation strength. The activation energy Δ in the relaxation time determines the energy spacing between the first excited states and the upper state through which the transition occurs. The fitting has been done by Poker,[22] one may use his results and identify them with our parameters. The γ, δ and Δ obtained by Poker are γ = 90 meV, δ = 0.4 meV and Δ = 1.8 meV. By comparing with our model, one gets $\alpha = \frac{\delta}{2}$ = 0.2 meV and $\Delta = 2(\beta - \alpha)$, β = 1.1 meV. Here the dominating transition has been determined to be the one through E_5 but not E_8. One can easily verify it by calculating the relaxation rates for both transitions. γ = 90 meV will be used in the rest of the fitting.

One can also determine the matrix element $\langle\psi_2|H_{44}|\psi_5\rangle$ from the pre-exponential factor in the relaxation time. Since $1/\tau = 3.89\times10^{10}\ \exp(-1.8/kT)$ (with kT in meV), one may compare it with Equation 10 and get $\langle\psi_2|H_{44}|\psi_5\rangle$ = 54 meV, or γ_{44} = 76 meV (see the Appendix).

For the deuterium step function like decrement result, one knows that the relaxation process cannot be an Orbach process. From the discussion in the previous section, one may conclude that the deuterium result must be due to a direct process. The fitting for D/Nb = 1800 ppm is shown in Fig. 9.

The distribution function used now is a more practical Lorentzian distribution. The parameters determined are α = .06 meV and $\eta_1 = 8 \times 10^{-4}$. β cannot be determined here but one realizes that it must be small so that the Orbach process is not detectable in the temperature range measurements are taken. There is a factor of two discrepancy between the concentration used in the fitting and that reported by Poker. This does not seem to be a serious problem, since a 50% error in the determination of the concentration is not unusual.

The elastic constant fitting is shown in Fig. 26. The fit is good at temperatures below 9 K. There is a discontinuity in slope in the background near 9 K due to the superconducting effect. This makes the behaviour of the velocity curve above 9 K difficult to determine.

The decrement and velocity fitting for another specimen with D/Nb = 230 ppm is shown in Fig. 27. The takeoff temperature is lower in the decrement, hence α = 0.048 meV and $\eta_1 = 6.4 \times 10^{-4}$. The D/T fit below 2 K is done by fixing D, which is an independent parameter.

The quantity $\omega\tau$ used in the fitting was $\omega\tau = 21/T$, for $\omega = 2\pi \times 10^7$ and T in Kelvin. The calculated $\omega\tau = \omega/BT$, using Equation 17, is only about 2/T. One suspects that the deviation may arise from the accuracy of Equation 9.

2. High Temperature Ultrasonic Results

The high temperature (150-200 K) relaxation peak observed by Mattas and Birnbaum[9] and Zapp and Birnbaum[28-29] may correspond to incoherent hopping through the same sites that would be expected at temperatures high enough to destroy the coherent tunnelling states. The effective potential would not be expected to change much since it should be determined mainly

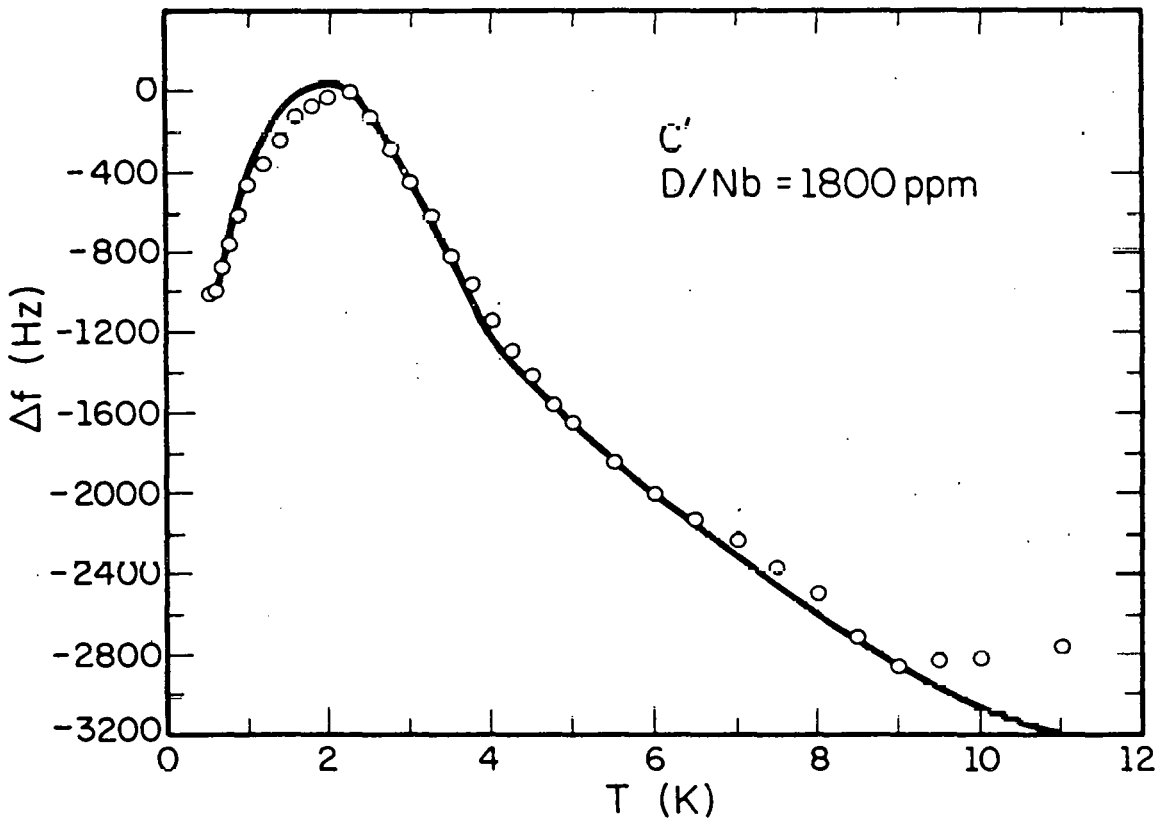

Figure 26. The frequency change of the C' mode as a function of temperature for D/Nb = 1800 ppm. The solid curve is the fit of the eight-state model with the parameters α = 0.06 meV and $\eta_1 = 8 \times 10^{-4}$. The D/T decrease below 2 K in the fit is done by fixing D, which is treated as an independent parameter.

Figure 27. The decrement per unit concentration and the frequency change of the C' mode as functicns of temperature for D/Nb = 230 ppm. The solid curves are the fit of the eight-state model with the parameters α = 0.048 meV and $\eta_1 = 6.4 \times 10^{-4}$. The 1/T fit below 2 K is 160/T (T in Kelvin).

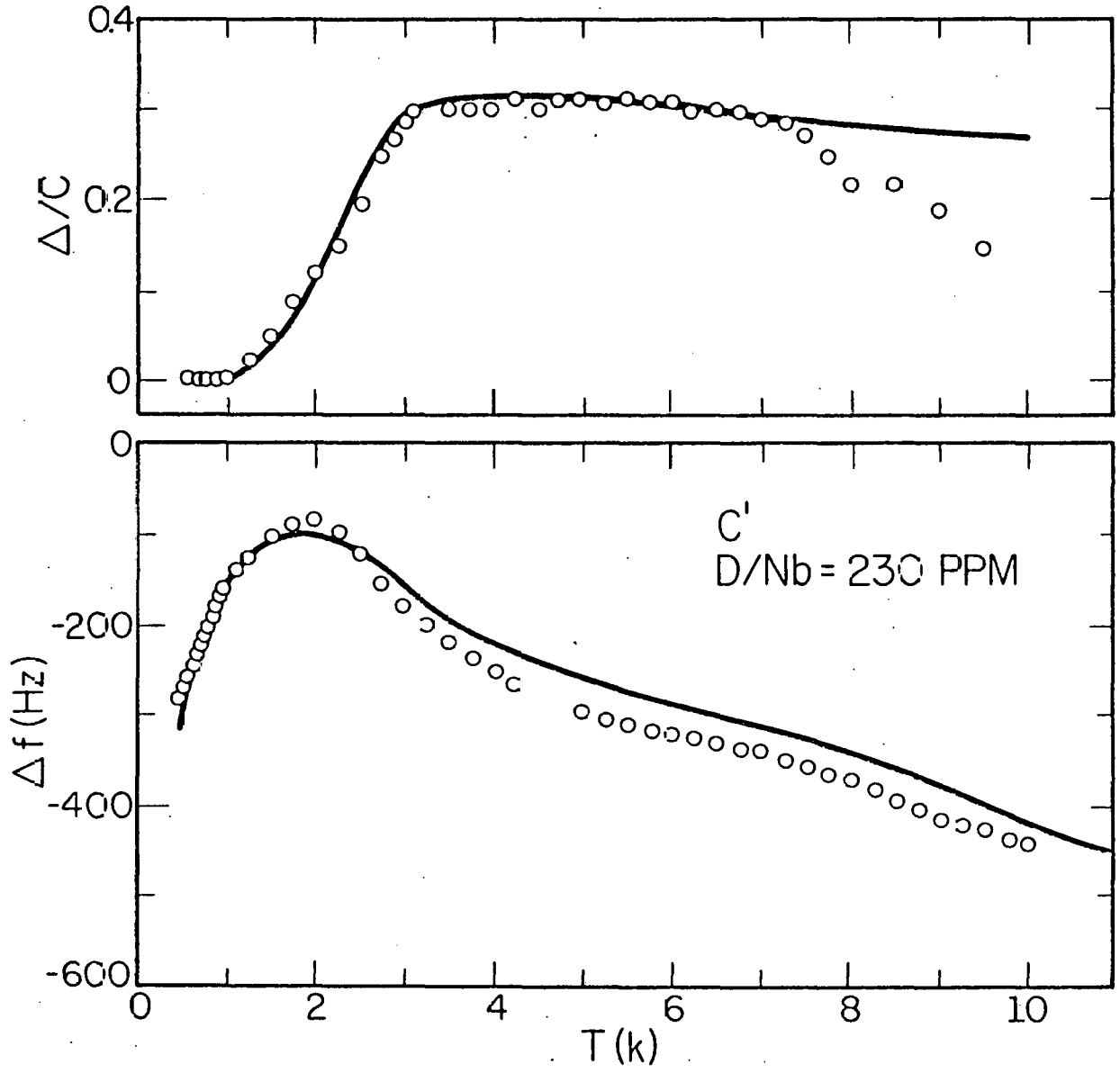
0.4
0.2
0
Δ/C
0
-200
-400
-600
Δf (Hz)
C'
D/Nb = 230 PPM
0
2
4
6
8
10
T (k)

by the strongly displaced nearest neighbour niobium atoms with respect to the oxygen, and less so by lattice relaxation about the hydrogen. One would therefore expect energy barriers ∿ .3 eV, and both C' (horizontal jumps) and C_{44}' (vertical jumps) relaxations, as observed. More detailed studies would be useful connecting the low and high temperature peaks to see if this is indeed an example of a transition from correlated to uncorrelated motion.

3. Specific Heat

It is worth pointing out first that there remains a large discrepancy between the Sellers, et al.[6] data and the Morkel, Wipf and Neumaier[14] data. In the Sellers, et al. data, the hydrogen responsible for the specific heat was estimated to be about 50 ppm, while in the Morkel, et al. data, the concentration of N-H pairs was 2000 ppm, which is 40 times larger; however, the measured specific heat was only 3 times larger. In order to account for this large discrepancy, Morkel, et al. claimed that the amount of trapped hydrogen in the samples used by Sellers, Anderson and Birnbaum should be 350 ppm, which was estimated from the residual resistivity ratio of the sample.

In our eight-state model, a concentration of 50 ppm was needed to obtain a good fit to the Sellers, et al. data. The Schottky term in Equation 6 was not used in hydrogen fitting, hence β was not determined for hydrogen. But in the deuterium data fitting, both α and β were determined. The Schottky term peaks around .3 K where a little bump is seen. The second term in Equation 6 peaks around 1.2 K, then starts to fall off slowly. The fitting for both hydrogen and deuterium is shown in Fig. 28, with the solid

Figure 28. The specific heat fit of the eight-state model (solid curve) and the two-state model (dashed curve) to the Sellers, Anderson and Birnbaum[6] data. The concentration used in the eight-state model fit is 50 ppm, while the concentration used in the two-state model is 350 ppm. The overall fit of the two-state model in the deuterium case is bad, and the fit at temperatures above 1 K in the hydrogen case starts to deviate from data.

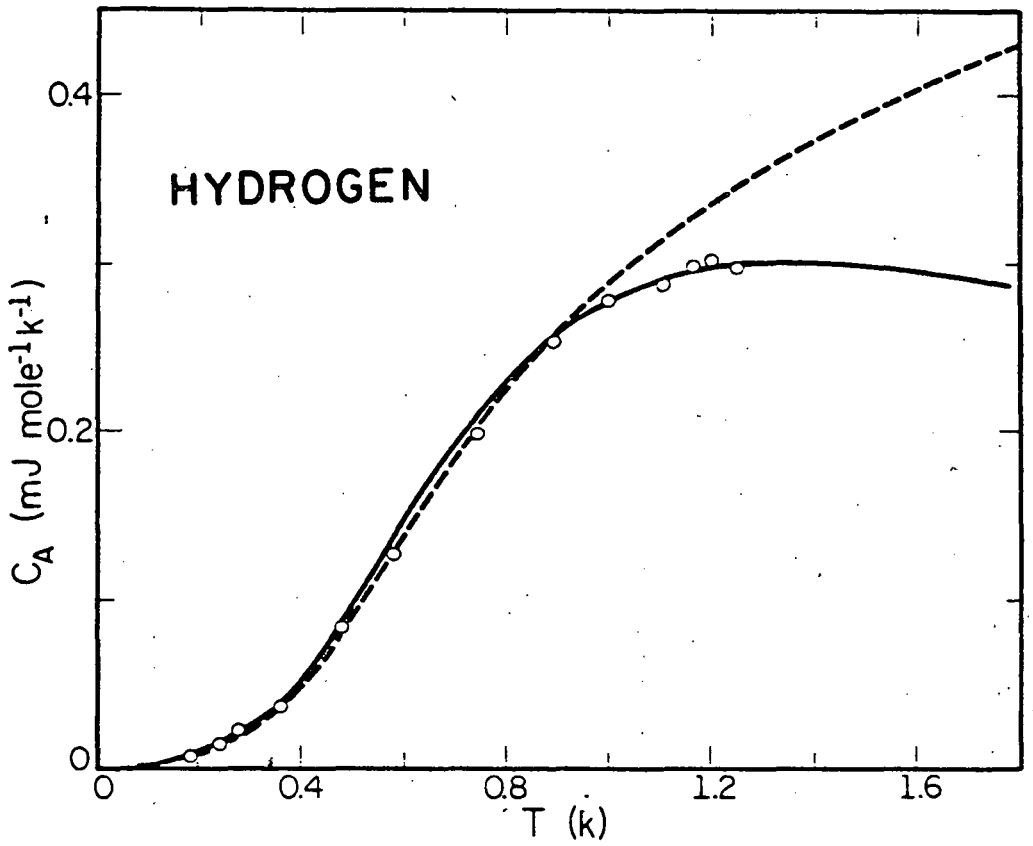
HYDROGEN
C_A (mJ mole^{-1}k^{-1})
0.4
0.2
0
0
0.4
0.8
1.2
1.6
T (k)

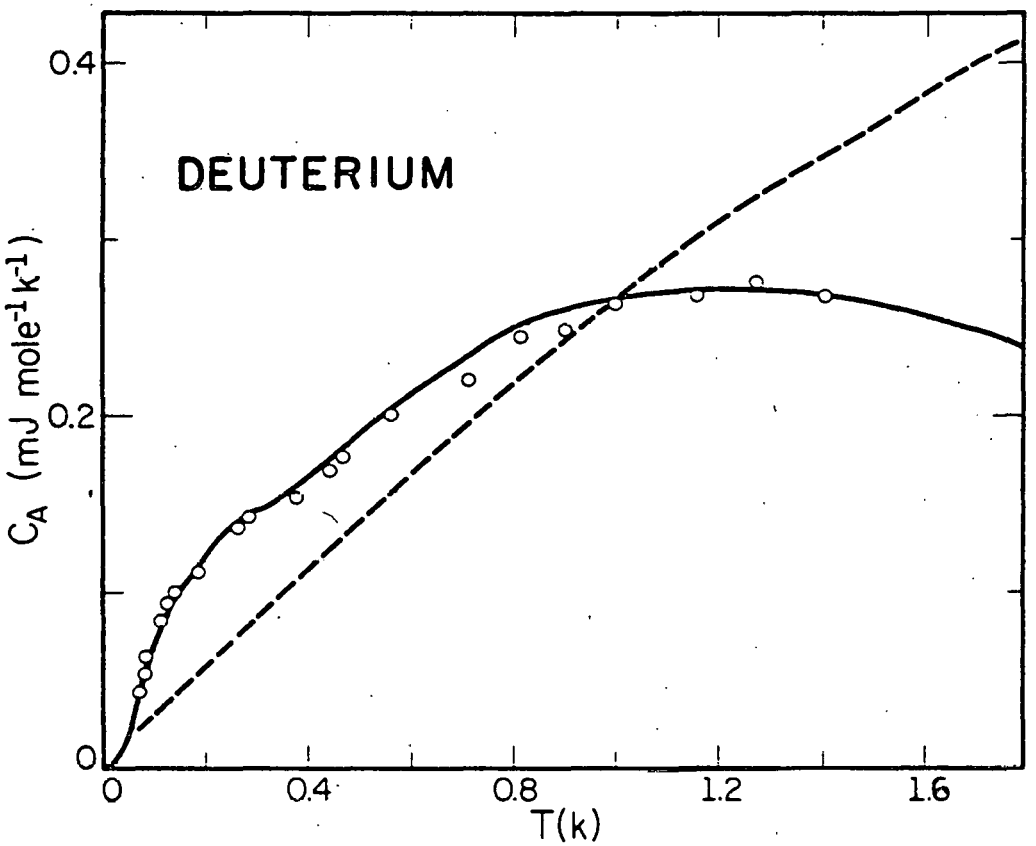
DEUTERIUM
C_A (mJ mole^{-1}k^{-1})
0.4
0.2
0
0
0.4
0.8
1.2
1.6
T(k)

curve representing the calculated specific heat from the eight-state model, and the dashed curve from the two state model suggested by Wipf, et al.[19]

If one assumes that Morkel, et al. were correct about the concentration of trapped hydrogen in the Sellers, et al. data, then in order to account for the rather small specific heat data, Wipf, et al. would have to use a very broad strain distribution so that most of the trapped hydrogen would not make contributions to the low temperature specific heat. However, the calculated specific heat would keep increasing almost linearly until about 8 K. Figure 27 clearly shows that the two-state model fit deviates from the data around 1 K for both hydrogen and deuterium, and the overall fit for deuterium is bad.

One may conclude here that the eight-state model can fit the data well with a rather small concentration compared with the concentration determined from resistivity measurements, while the two state model cannot fit the data well with any concentration but can only get the magnitude of the measured specific heat about right, if large strains are assumed.

The parameters determined from ultrasonic and specific heat data are collected in Table 1.

Table 1. Parameters α, β, η_1 Determined from Ultrasonic Data and Specific Heat Data for Hydrogen and Deuterium.

		Ultrasonic	Specific Heat
Hydrogen	α	0.2 meV	0.14 meV
	β	1.1 meV	--
	η_1	--	2×10^{-4}
Deuterium	α	0.06 meV	0.1 meV
	β	--	0.03 meV
	η_1	8×10^{-4}	1×10^{-4}

One can see that the α and β agree rather well from different fittings. The η_1 from the ultrasonic data is eight times larger than that from the specific heat data for the deuterium case. This is reasonable, because in the specific heat fitting, only 50 ppm trapped deuterium was in the sample, while in the ultrasonic data, there was 1800 ppm trapped deuterium.

4. Thermal Conductivity

With the α and β known, one may calculate the energy gaps for all the possible resonance transitions. Table 2 lists all the energies between the states that have nonzero matrix elements through C' or C_{44}, with the upper value for hydrogen and lower value for deuterium.

Table 2. Energy Difference in meV Between the Levels That Have Nonzero Matrix Elements Through C' or C_{44}.

	E_1	E_2	E_3	E_4	E_5	E_6	E_7	E_8
E_1				C' 0.8 0.24		C_{44} 2.6 0.18	C_{44} 2.6 0.18	
E_2					C_{44} 1.8 0.06			C_{44} 2.6 0.18
E_3					C_{44} 1.8 0.06			C_{44} 2.6 0.18
E_4						C_{44} 1.8 0.06	C_{44} 1.8 0.06	
E_5								C' 0.8 0.24
E_6								
E_7								
E_8								

One then can expect phonon resonant scattering at a temperature $T = \frac{\Delta E}{3.8k}$.[30] Hence the temperatures at which phonon resonant scattering will be expected are 2.4 K, 5.5 K and 8 K for hydrogen, and 0.18 K, 0.54 K and .73 K for deuterium. In Fig. 3, one can see that the mean free path minima are at 0.8 K for hydrogen charged sample and 0.1 K for deuterium charged sample. In the hydrogen case, it seems that our model does not predict the temperature observed. However, it has been shown[30] that the phonons can also be scattered from dislocations in Nb, and this interaction produces a minimum in the mean free path around .8 K. The presence of H in Nb may enhance the dislocation scattering caused by the dislocation loops punched out by β-phase hydride as the sample is cooled. Hence it is not inconsistent with our model. In the deuterium case, the model does predict a phonon resonant scattering at 0.18 K, which is close to the 0.1 K observed. The other two temperatures 0.54 K and 0.72 K, predicted by the model, will also be mixed up with the dislocation scattering, and hard to separate.

5. Inelastic Neutron Scattering

The smallest energy gap in the hydrogen case is 0.4 meV, which is the energy difference between the ground state and the first excited states. It seems that it is inconsistent with the energy 0.19±0.04 meV obtained from the inelastic neutron scattering experiments by Wipf, et al.[18] However, the sample they used had 1.3% oxygen and 1.6% hydrogen, a large internal strain would be expected. From the energy diagram for hydrogen; one can see that the energy difference between the ground state and the first excited state will be reduced at large strains. Hence the energy 0.19 meV is not incompatible with our model.

6. Tunnelling Distances and Potential Barriers

From Equations 30 and 32, the α, β in Table 1, and the neutron vibrational levels, 0.11 eV and 0.16 eV, one can calculate V_a, V_b and a, b for hydrogen. Since the vibrational levels for the trapped deuterium have not been reported, it is assumed here (may not be good) that they are the same as those of the free deuterium. There are two vibrational levels with the higher one degenerate, one does not know which levels should be used for the α, β tunnelling. For the present calculation, we simply use the two degenerate levels, and demonstrate later that it is a reasonable assumption based on some potential calculation.

Table 3 lists a, b, V_a, V_b, and r (the O-H or O-D distance calculated from a and b) for hydrogen and deuterium.

Table 3. Tunnelling Distances a, b, Energy Barriers V_a, V_b and O-H, O-D Distance r

	Hydrogen	Deuterium
a	1.04 Å	0.92 Å
b	0.9 Å	0.95 Å
r	0.86 Å	0.81 Å
V_a	340 meV	300 meV
V_b	260 meV	320 meV

The O-H distance calculated seems to be small. But if one takes into account that there might be some off-center displacement of the O-H C.M.,[31] and that the hydrogen wave function is extending out away from the oxygen (explained in next section), the real distance should be larger than the calculated 0.86 Å. This rather small distance also may be due to the electronic shielding in the metal lattice. The deuterium result is based on the assumption that the trapped and the free deuterium have the same vibrational levels, which have not been observed experimentally. One should not take it too seriously.

7. A Simple Potential Calculation

It remains to be demonstrated that the equilibrium positions assumed in the model are reasonable and that the energy levels found in neutron spectroscopy are not incompatible with this model.

A potential for the Nb-H interaction has been proposed by Sugimoto and Fukai,[32-33] consisting of two Born-Mayer terms, one short-range and the other long-range. The parameters of this potential were chosen to fit the neutron spectroscopy energy levels and the observed strain field anisotropy of hydrogen. With the potential, they calculated potential maps and wave functions numerically taking account of lattice relaxation by a self-consistent procedure for several configurations of free (untrapped) hydrogen, including the tetrahedral (1T), octahedral (O), and ring of four tetrahedral (4T) configurations. The short range part of the potential was the most important part. They found that the tetrahedral configuration (1T) had the lowest energy with the potential map given in Fig. 29(a). The ground state wave function is centered at a tetrahedral site, but the

Figure 29. (a) The equi-potential contour for a self-trapped hydrogen on a tetrahedral site labeled S. The potential is given by Sugimoto and Fukai.[32,33]

(b) The equi-potential contour for the trapped hydrogen, using a A/r^6 potential for the Nb-H interaction and AR/r^6 for the O-H interaction. The oxygen is located on an octahedral site, and the two potential minimum positions labeled a, e are on the plane of the face of a unit cell. The potential is soft along the O-H direction.

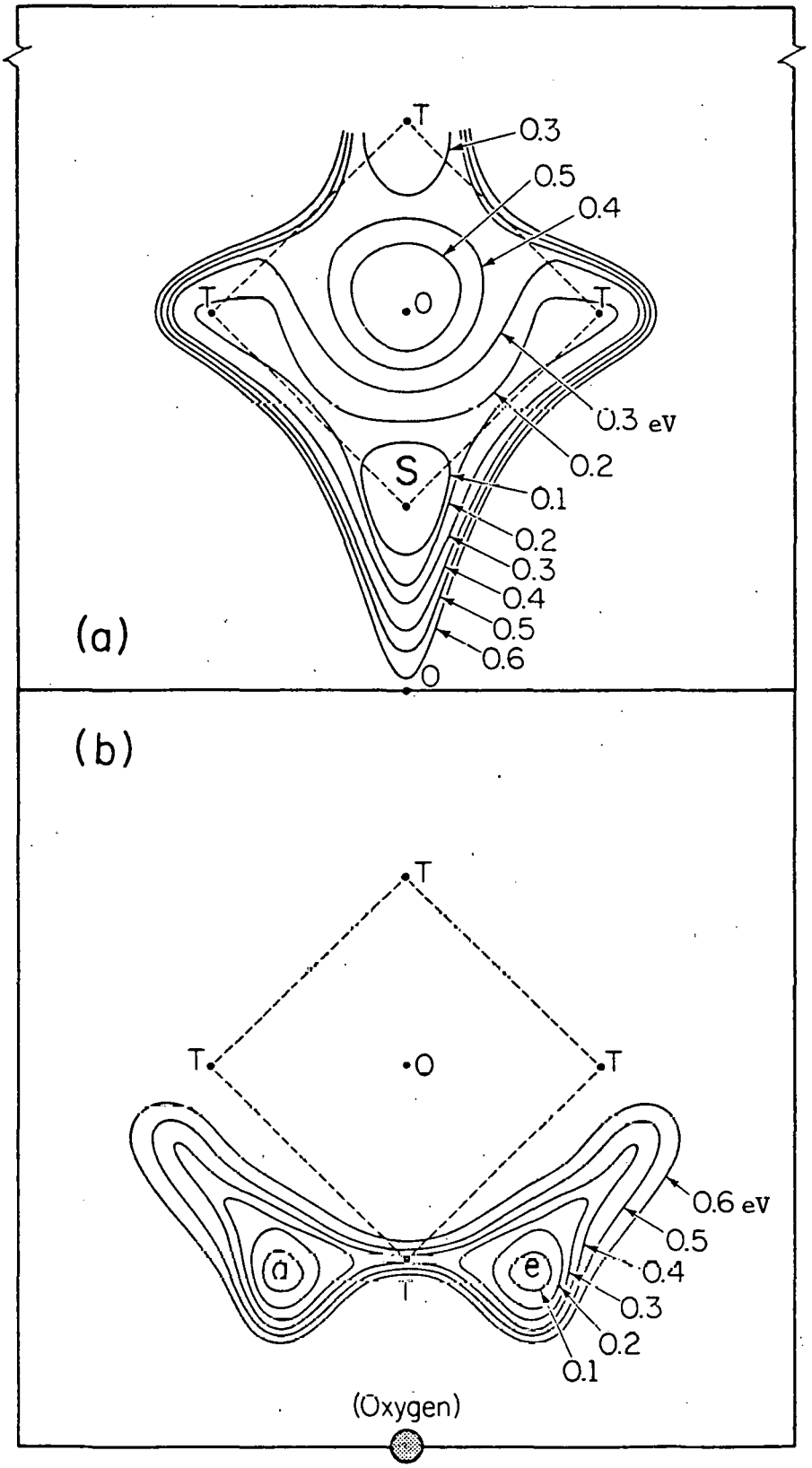
T
0.3
0.5
0.4
T
O
T
0.3 eV
0.2
S
0.1
0.2
0.3
0.4
0.5
0.6
O
(a)
(b)
T
T
O
T
0.6 eV
0.5
a
e
0.4
T
0.3
0.2
0.1
(Oxygen)

excited state wave functions extend out to neighbouring tetrahedral sites. In spite of this anharmonicity of the potential, the observed excitation energies seen in neutron spectroscopy were approximated well.

A full calculation of this type for the present model has not been attempted. An approximate calculation of the potential has been made using a simple potential of the form A/r^6 for the Nb-H interaction, with AR/r^6 for the O-H interaction, and assuming a displacement D for the niobiums which are nearest neighbours to the oxygen. The potential gives a similar map for the potential along a T-O-T path to that given by Sugimoto and Fukai (4-T model) for an assumed (constant) relaxation of 11.6%. It is not intended here to obtain accurate results, but only to see if the general features of the model can be obtained in a reasonable way.

It was found that the postulated eight minimum positions can be obtained by adjusting R and D. Shown in Fig. 30 are the equi-potential contours for two planes, one with the oxygen and two potential minimum positions a and e on it, and the other one with potential minimum positions a, e, b and f on it. The potential has been normalized so that the barrier between a and e is around .4 eV. One could solve the wave equation to get the energy levels; however, one can easily see from Fig. 29 that the two "frequencies" in the α and β tunnelling directions are about the same, while the "frequency" in the O-H direction is smaller. Furthermore, by comparison with the Sugimoto-Fukai potential in Fig. 29, it is possible to imagine that the two high "frequencies" are about the same as for the tetrahedral 1T site.

The fact that the potential is rather soft along the O-H direction could be used to account for the rather small O-H, O-D distance calculated

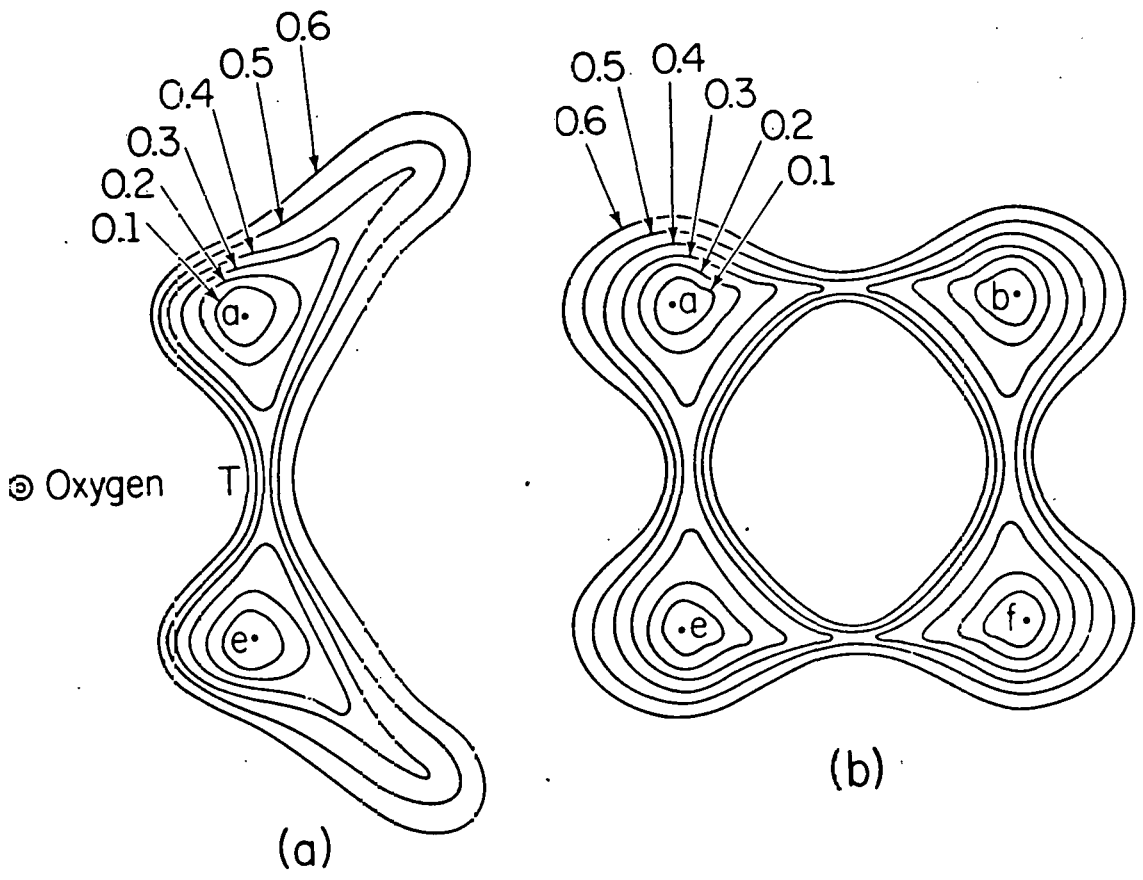

Figure 30. (a) Equi-potential contour on the plane with oxygen and two potential minimum positions a, e on it.

(b) Equi-potential contour on the plane with the four potential minimum positions a, b, e, f on it.

before, since the hydrogen wave function is expected to extend out much more in this direction, meaning a larger O-H or O-D distance.

The parameters R and D used are 5×10^{-3} and .18a (a is the lattice constant). The small R indicates that the O-H interaction is small, compared with the Nb-H interaction. The displacement D is bigger than the one .142a obtained by Blanter and Khachaturyan[34] using a lattice statics theory. For D = .142a, we find a second shallower minimum near the second nearest neighbour tetrahedral site of the oxygen.

Since the real potential is not known, and the approximation used here is extremely crude, this calculation cannot be taken seriously numerically. However, we believe that it demonstrates the existence of the main topological features required, with two high "frequencies" and one low, so that one cannot conclude from the neutron spectroscopy data that the trapped hydrogen must be on tetrahedral sites, and that these sites must be far from the oxygen. The calculation suggests instead that the main effect of the displaced niobium and the oxygen atom is to displace the potential well, rather like the familiar rigid displacement of a harmonic oscillator potential in an external field.

PART B

V. EXPERIMENTAL TECHNIQUES AND APPARATUS

1. Sample Preparation

Two specimens were used for ultrasonic measurement. One of them, cubic and slightly larger than one centimeter dimension, was spark cut from a six inch section of a single crystal niobium rod one inch in diameter which was supplied by Dr. H. K. Birnbaum. The second one of about the same size, was prepared from a boule of 1/2 inch diameter single crystal purchased from MRC. The surfaces were all oriented with one set of (100) faces and two sets of (110) faces. The orientation was done by the x-ray scattering technique developed by Ochs.[35] The surfaces were mechanically polished by mounting in a stainless steel polishing disk and using diamond or aluminum paste as an abrasive.

Impurity analysis indicated that the primary impurity was Ta with some amounts of N, O and C. The concentrations of these impurities for both samples are given in Table 4. After a few runs, Nb2 was annealed at 2500 K in an ultra high vacuum of 10^{-11} Torr for a week. The oxygen content in this sample was estimated to be around 20 ppm.

Table 4. Impurity Concentrations in Atomic ppm.

	Nb1	Nb2
Ta	200	100
C	70	60
N	49	80
O	64	200

2. Hydrogen and Deuterium Charging

Sample charging with hydrogen or deuterium was done from the gaseous phase at high temperature. It consisted of heating the specimen to about 800°C in a vacuum of 10^{-6} torr. At this temperature, the impermeable oxide on the sample surfaces would dissolve into the metal and allow hydrogen to diffuse in. Hydrogen or deuterium which had been purified by diffusing through a Pd-Ag membrane was introduced into the sample chamber at the pressure required to equilibrate the concentration of the gas in the sample. The thermodynamic relationship for niobium-hydrogen system in equilibrium at low concentration values is given as[36]

$$\log C = 0.5 \log P - 2.43 + 1840/T \qquad (33)$$

where C in at%, P in mbar, T in K. As the temperature of the sample was lowered, the pressure of the gas was correspondingly reduced to maintain equilibrium. At the end of slow cooling (about 150°C), air was admitted briefly into the system to reoxidize the niobium surface and so confine the hydrogen within the sample.

The concentration was checked again by weighing the sample on a microbalance before and after charging. It was discovered that the concentration of gas in the sample was always lower than the value expected from thermodynamic consideration. A 50% discrepancy is not unusual for C_H < 500 ppm, but it gets better for higher hydrogen concentrations.

3. Ultrasonic Measurement

The ultrasonic waves were generated by unplated 1/4 inch diameter 10 MHz transducers. The transducers were bonded to the sample with Nonaq

stopcock grease. Because of the difference in thermal expansion between the quartz and niobium sample, great care had to be taken to insure the survival of the bond while cooling fast from 230 K to helium temperature.

The procedure for making a good bond is summarized here. First the sample surface and transducers were cleaned in acetone then dried and heated to about 40°C. A drop of Nonaq was outgassed by gently heating under vacuum for a few minutes. A small amount of the Nonaq was then applied to the sample surface and the transducer was gently pressed into place. The quality of the bond can be judged visually through the unplated transducer and tested at room temperature using a Sperry Attenuation Comparator.

Attenuation measurements were performed using Matec Models 6600 and 2470A pulse echo generator and attenuation recorder. The pulse generator was frequency variable and generated a pulse about one microsecond in length. The frequency could be adjusted to any odd harmonic of the transducer fundamental frequency, allowing a large variation in the measurement of decrement versus frequency. The attenuation recorder measured the logrithmic difference in amplitudes of two echos in units of decibels. The decrement was obtained by the relation[37]

$$\Delta = A/8.68f \tag{34}$$

where A is the attenuation in dB/μsec and f is the frequency in MHz.

A detailed description of the attenuation and velocity system is given by Hultman[26] and Wong.[38]

The corresponding elastic constant is given by

$$C = \rho v^2 \tag{35}$$

For small change in velocity, the frequency is related to the corresponding elastic constant by

$$\frac{\Delta C}{C} = 2\,\frac{\Delta f}{f} \qquad (36)$$

Measurement of the frequency of the 10 MHz wave is efficient to determine relative change in the elastic constants. It is possible to measure change in frequency as small as 1 Hz, corresponding to a sensitivity of 2×10^{-7} in the elastic constant.

4. Cryostat

The initial experiments were performed using a He^3 refrigerator which was designed for temperatures ranging from 0.5 K to 60 K. It turned out later that quenching the sample from 250 K to helium temperature was necessary to prevent hydrogen from precipitation, and the low cooling power He^3 refrigerator was not good for our experiments. Hence the later experiments were performed using the other cryostat which was originally designed for radiation damage experiments. The cryostat and temperature measurement and control system are described by Hultman[36] and Wong.[38]

5. Experimental Procedure

Background runs were done on the initial slow cooling (0.5 K/min) from room temperature to 2 K. A steep drop in attenuation was always observed in the temperature range from room temperature to about 240 K probably because of the gradual freezing of the grease bond. The superconducting contribution was predictable and could easily be accounted for. The contribution by hydrogen to the attenuation therefore was easier to determine.

Quenching usually was done after background runs. The sample temperature was raised to 240 K for about an hour to let the precipitated hydrogen redissolve into solution. Then with the throttle valve all the way open, the sample was quenched to helium temperature. The quenching rate was estimated to be about 2 K/sec. Attenuation and velocity measurements were made for 10 and 30 MHz from 2 K to 30 K.

The annealing program consisted of a series of linear temperature ramps from 5 K up to a chosen anneal point followed by a 10 minute anneal and a linear ramp back to 5 K. After each anneal point, the attenuation were measured from 2 K to 30 K. The annealing point was chosen to start from 60 K for hydrogen, since usually below 60 K the 10 minute anneal would not affect the relaxation peaks.

VI. ANELASTIC RELAXATION

A crystal containing a dilute concentration of point defect will produce a distortion of the neighboring atoms to accommodate the solute atom. If the atomic configuration of the defect has a symmetry lower than that of the host crystal, then the defect can take up several equivalent but distinguishable orientations in the crystal. Under zero stress, the equilibrium occupation of all the available sites is simply a random one in which the defect population is divided equally among the different orientations. Due to the ability of a given defect to move from one orientation to another by thermally activated jumps, it should be borne in mind that the equilibrium state is a dynamic condition which can also be thought of as the result of each defect spending equal amounts of time in each of the equivalent orientations. The application of an appropriate stress can remove the degeneracy, causing a repopulation of the number of the defects in the various orientations. The stress induced ordering leads to the production of an additional lattice strain due to the corresponding ordering of the distortion surrounding the defect. This additional strain is reflected in the elastic constant and internal friction. The process whereby an applied stress leads to ordering of an internal variable which produces a change in the elastic constant is referred to as an anelastic relaxation.

A good review of anelastic relaxation is given by Nowick and Heller[39-40] and Nowick and Berry.[41] The results that are relevant to the discussion will be presented here.

Transitions between defect orientations are assumed to occur with a characteristic time, defined as the relaxation time, τ. When an external stress with an angular frequency ω is applied, the response of the decrement, Δ, and the relative change in the elastic constant, $\Delta C/C$, are given by the well-known Debye equations (Equation 13 in Part A). The relaxation strength Δ_R is temperature dependent, and for classical systems is given by

$$\Delta_R = \frac{\beta c_o v_o}{kT} C(\delta\lambda) \tag{37}$$

where β is a dimensionless geometrical constant, c_o is the atomic concentrations of defects, v_o is the molecular volume, C is the appropriate elastic constant, k is Boltzmann's constant, T is the temperature and $\delta\lambda$ is the shape factor of the defect derived from differences between the principal values of the lambda tensor. The lambda tensor describes the strain produced in the crystal per unit concentration of the defect.

The temperature dependence of the relaxation strength for a quantum system can be very different from that given above. In general, the relaxation strength will approach the classical value at high temperatures, but can exhibit deviations at low temperatures.

The forms of the response functions are simple when expressed as functions of $\omega\tau$. Since it is usually difficult to vary ω by more than one order of magnitude when measuring any sample to cover various frequencies. It is usually simpler to vary τ by varying the temperature. The temperature dependence of τ may take various function forms, but often the function follows the Arrhenius equation,

$$\tau = \tau_o \exp(Q/kT) \tag{38}$$

where Q is the activation energy and k is Boltzmann's constant. The response functions for this temperature dependence are displayed in Fig. 31. The decrement shows a peak where $\omega\tau = 1$. The response in the elastic constant is different. At low temperatures, where τ is very large, $\Delta C/C$ is small because the defect does not move fast enough to make a transition during a cycle of stress. At higher temperatures, the elastic constant decreases, the dispersion occurring in the same temperature range as the peak in the decrement. At still higher temperatures, instead of becoming constant, the elastic constant rises again to its low temperature value. This occurs because of the 1/T temperature dependence of the relaxation strength as seen in Equation 38.

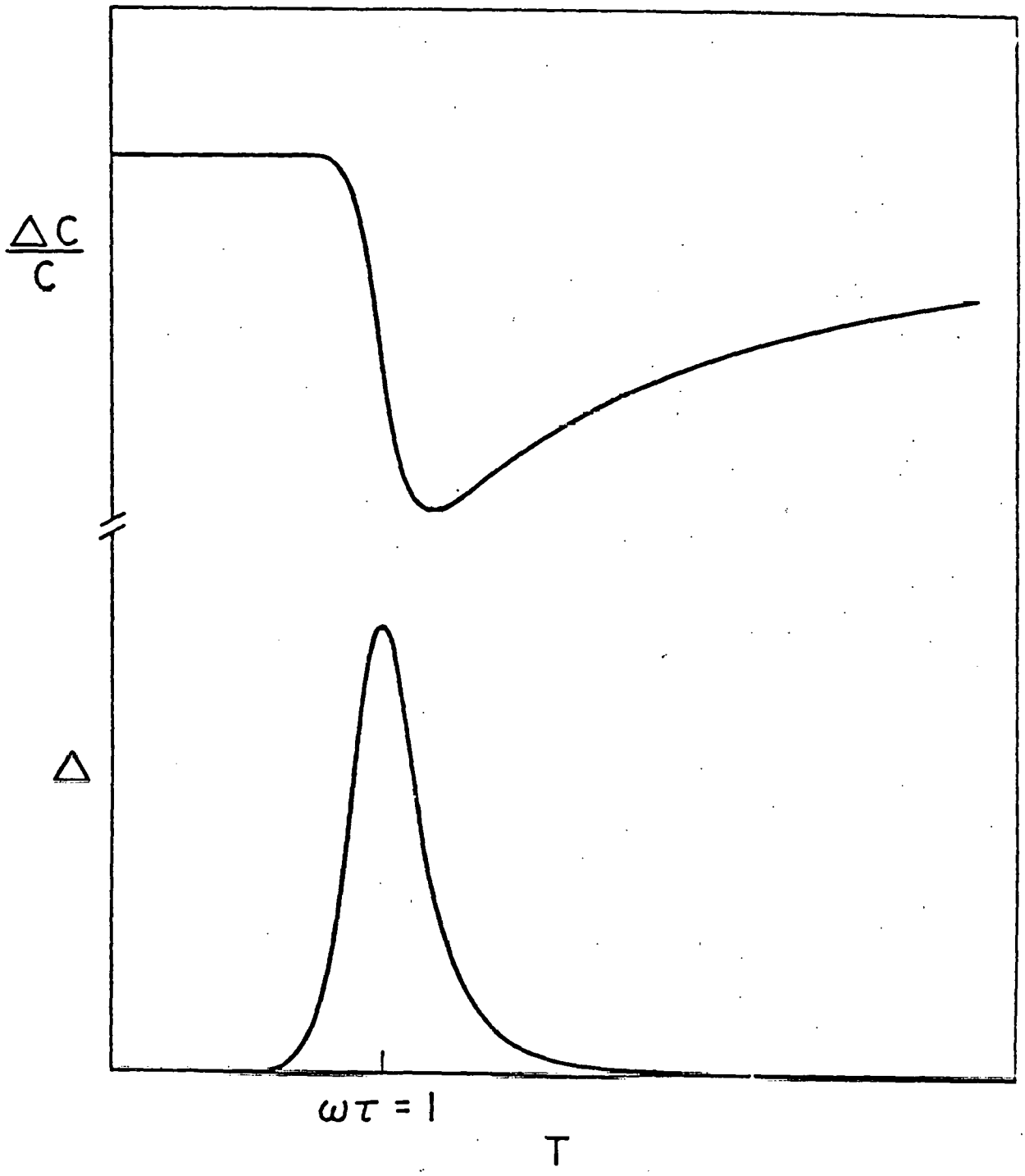

Figure 31. The decrement Δ, and elastic constant change, ΔC/C, for an anelastic relaxation as functions of temperature. The decrement peak and the elastic constant decrease are centered at a temperature where $\omega\tau = 1$.

VII. EXPERIMENTAL RESULTS

1. Hydrogen Results

In the present work, measurements of ultrasonic attenuation and velocity in dilute Nb-O-H alloys were made as a function of temperature, frequency, polarization, annealing temperature and isotope. In addition to the stable 2.5 K relaxation peak (peak 1) found by Poker, et al.,[20] an additional low temperature isotope sensitive peak (peak 2) was found when the specimen was rapidly cooled to helium temperature.

Shown in Fig. 32 is a plot of decrement versus temperature for a 10 MHz C' mode in a niobium crystal containing about 100 ppm O and 700 ppm H after a rapid cool down from 240 K, followed by annealing at 70, 80, 90, 100 and 120 K. The decrement is made up of a temperature independent background due to bonding and diffraction losses, an electronic contribution proportional to the electrical conductivity which decreases below the superconducting transition temperature, and two peaks due to hydrogen. The peak at 6.3 K anneals out near 80 K, while the peak at 2.5 K increases only a small amount. Both peaks were observed in the C' mode, but not in the C_{44} mode.

Figure 33 shows the decrement versus temperature for three niobium specimens with differing oxygen contents after rapid cooling from 240 K. The hydrogen concentration is much greater than the oxygen concentration. The background has been subtracted in this figure. The peak heights scale with the oxygen concentration, while the electronic contribution decreases with increasing impurity content. The background attenuation at the Nb superconducting critical temperature shows a discontinuity which is

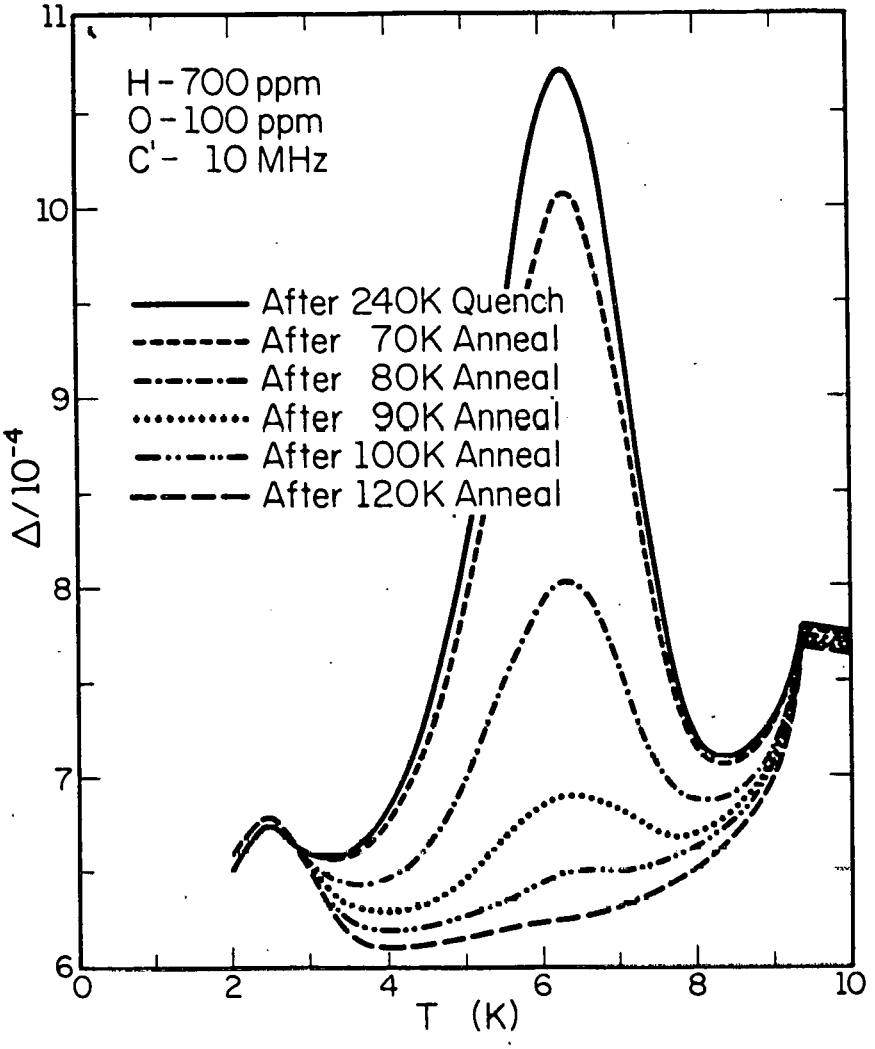

Figure 32. The decrement versus temperature for a 10 MHz C' mode in a niobium crystal containing about 100 ppm O and 700 ppm H after a rapid cool down from 240 K, followed by annealing at 70, 80, 90, 100 and 120 K. The discontinuity near 9.2 K is due to the transition from normal state to superconducting state.

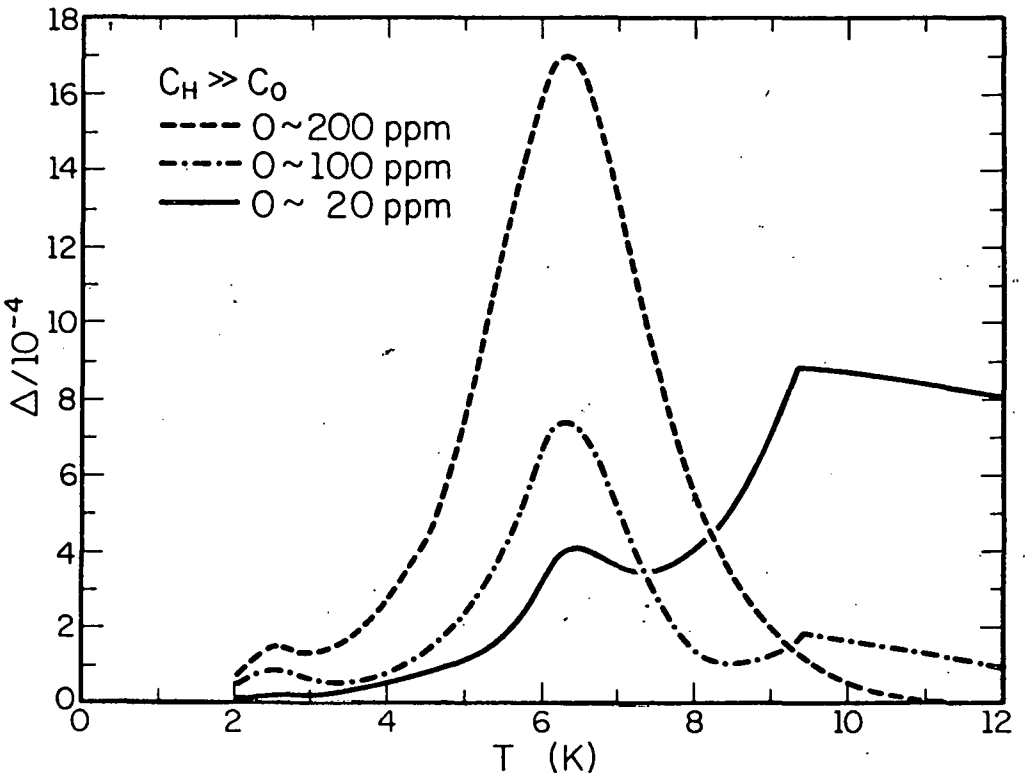

Figure 33. The decrement versus temperature for three niobium specimens with differing oxygen concentrations after rapid cooling from 240 K. The superconducting drop near 9.2 K is sensitive to the oxygen content. The height of peak 2 is also related to the oxygen content.

sensitive to the oxygen concentration. In the purest sample (after one week UHV anneal at 2500 K), the discontinuity drop was large but peak 2 was small. However, in the sample with about 200 ppm oxygen, the drop was hardly observed and peak 2 was large. After unloading the hydrogen in the specimen, a small discontinuity was found. The superconducting effect in the background attenuation serves as a monitor for the impurity content.

The decrement as a function of temperature for various frequencies, from 10 MHz to 70 MHz is shown in Fig. 34. The superconducting effect increases as a function of increasing frequency. The shear wave attenuation due to conduction electrons is given[42] in the low frequency limit (electron mean free path << ultrasonic wavelength) by

$$A = \left(\frac{2\pi^2 f^2}{\rho v^3}\right)(3\pi^2 N)^{2/3}\left(\frac{\hbar^2 \sigma}{5e^2}\right) \tag{39}$$

where f is the frequency of the sound wave, ρ is the sample density, v is the sample velocity, N is the number of electrons of charge e per unit volume, and σ is the electrical conductivity (all in Gaussian units). The decrement can be obtained by $\Delta = A(dB/\mu sec)/8.68f(MHz)$. Hence the decrement scales linearly with frequency and conductivity. The resistivity due to oxygen in Nb is 5 $\mu\Omega\cdot$cm/at%,[43] 100 ppm oxygen corresponds to 5×10^{-2} $\mu\Omega\cdot$cm. The calculated decrement for 10 MHz is about 9×10^{-5}, which is smaller than the measured value 1.6×10^{-4}. The figure also shows that the discontinuity drop scales roughly linearly with frequency.

The two peaks shift to higher temperatures as a function of increasing frequency. The relaxation time of peak 1 has been shown by Poker[22] to

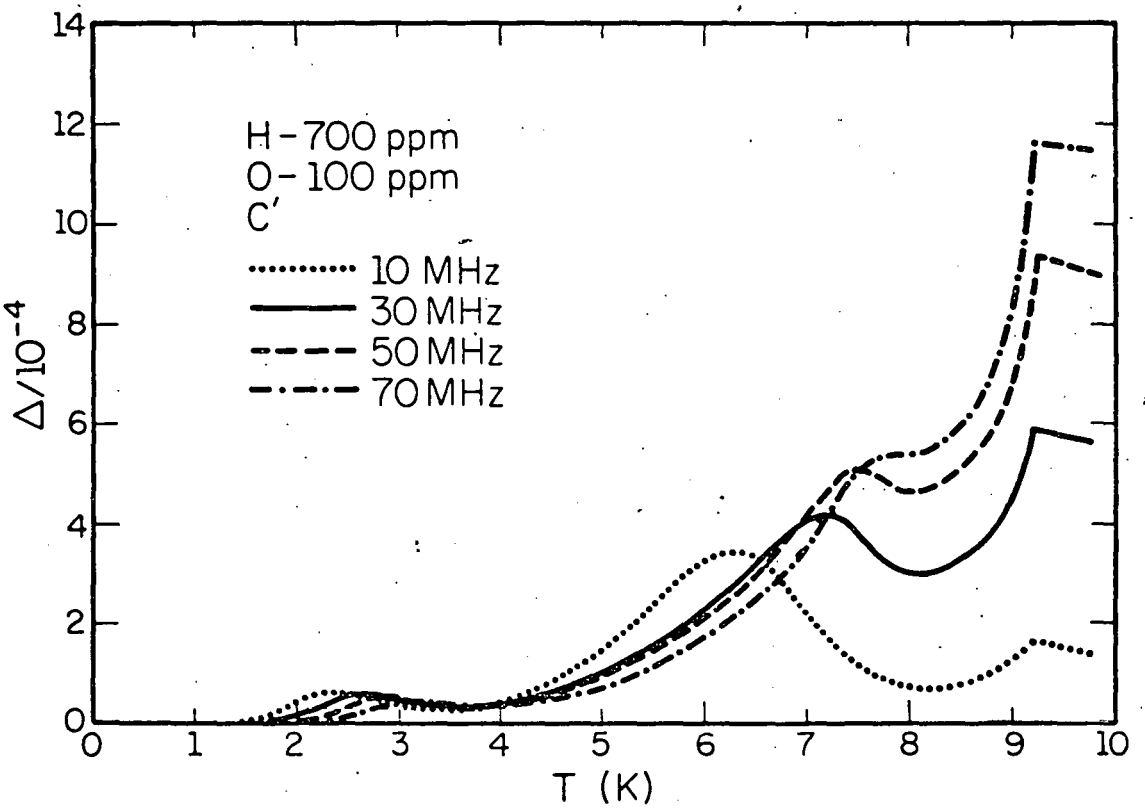

Figure 34. The decrement as a function of temperature for various frequencies. The positions of both peak 1 and peak 2 shift to higher temperatures as a function of increasing frequency. The superconducting drop near 9.2 K is proporticnal to the frequency.

have an exponential temperature dependence with an activation energy of 1.8 meV. The relaxation time of peak 2 as a function of temperature is plotted in Fig. 35. It also has an exponential temperature dependence with an activation energy of 5.5 meV, and a frequency factor of 2.96×10^{11}.

The temperature dependence of the relaxation strength of peak 2 was obtained by plotting the peak heights (with the electronic contribution subtracted) as a function of inverse temperature, which is shown in Fig. 36. Due to the large superconducting effects at higher frequencies, the error is rather large. However, one can still see roughly that it has a 1/T temperature dependence, and does not show the quantum depletion effect observed in peak 1.

2. Deuterium Results

Shown in Fig. 37 is a plot of decrement versus temperature for a 10 MHz C' mode in a niobium crystal containing 100 ppm oxygen and 2000 ppm deuterium. Peak 1 was buried in peak 2, which appeared near 10.5 K with a high temperature shoulder. Also shown in Fig. 38 is the same plot but for a 30 MHz C' mode.

The large attenuation at higher frequencies made it difficult to take any measurements, therefore only 10 MHz and 30 MHz attenuation measurements were made for deuterium charged samples. With only two relaxation frequencies, it is hard to determine the temperature dependence of the relaxation time. But roughly speaking, the peak shifts to higher temperatures as a function of increasing frequency. If an Arrhenius dependence of relaxation time with temperature is assumed as in the hydrogen case. The activation energy can be obtained. Shown in Fig. 35 is a plot of relaxation

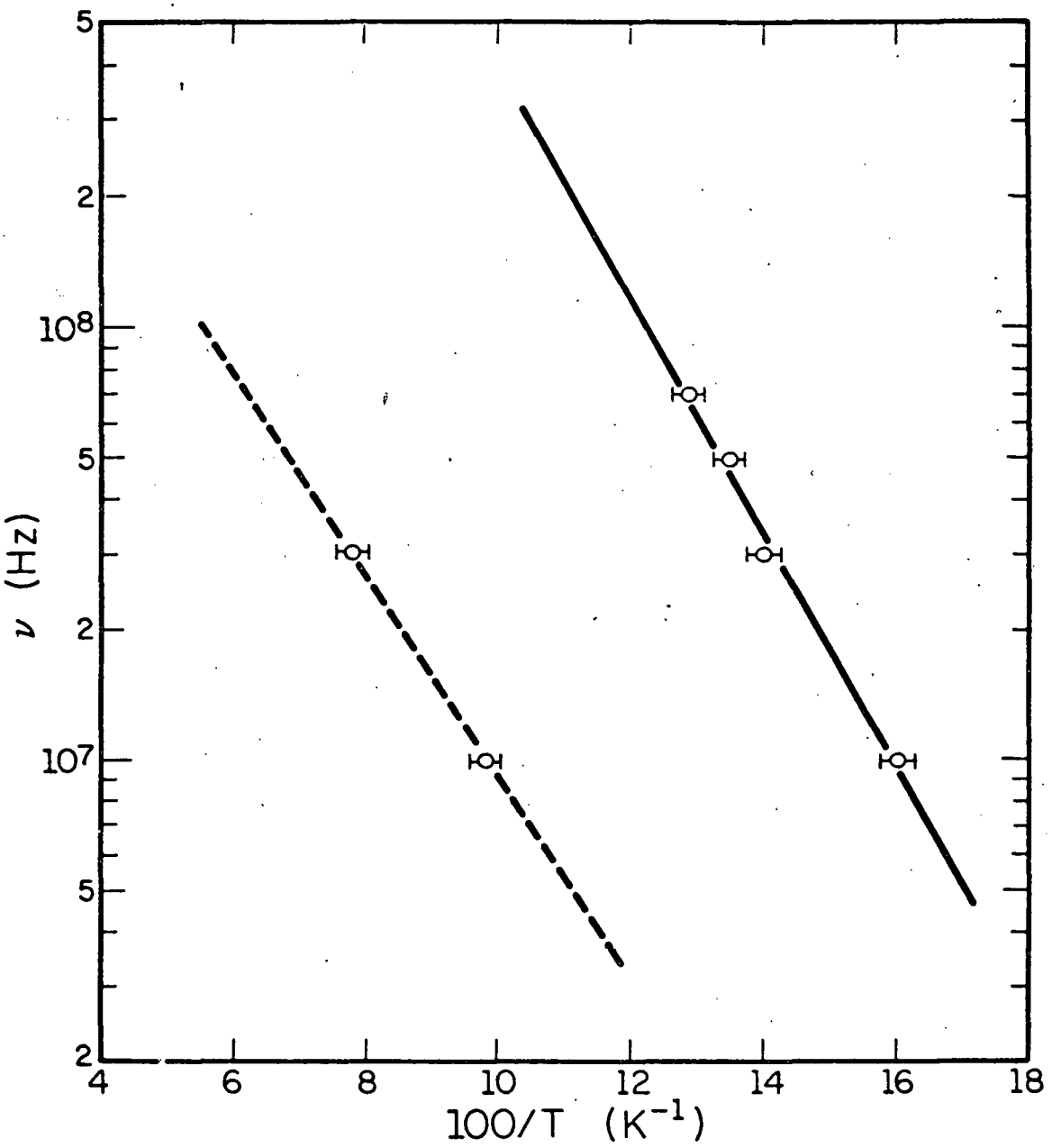

Figure 35. The logarithm of relaxation frequency as a function of inverse temperature. The solid curve is the fit to the data points of the OH_2 relaxation, with an activation energy of 5.5 meV. The dashed curve is the fit to the data points of the OD_2 relaxation, assuming that the relaxation frequency has an exponential temperature dependence.

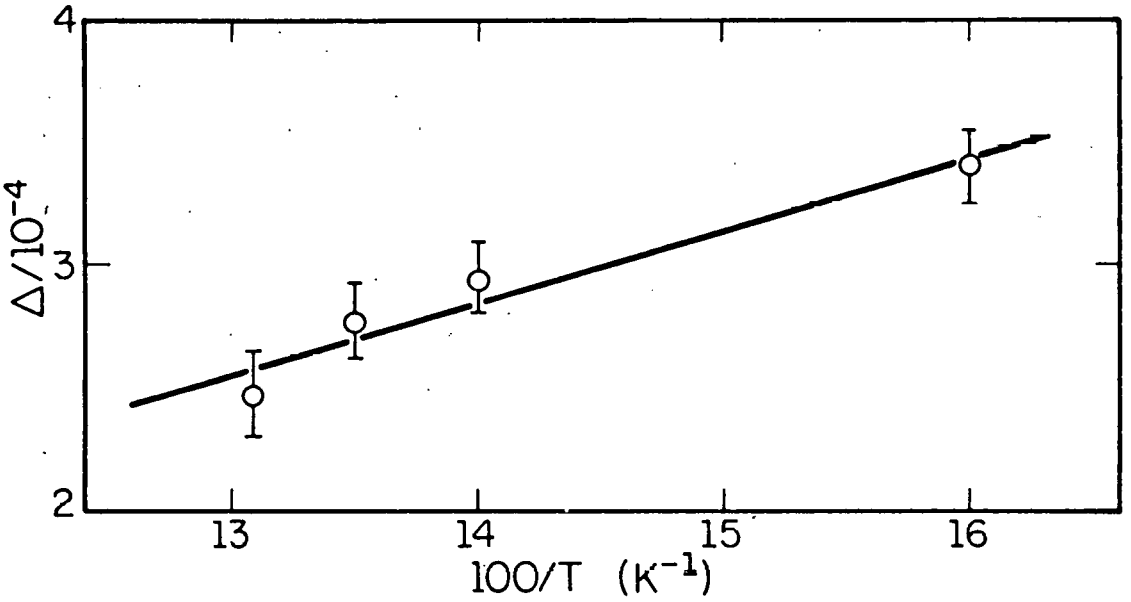

Figure 36. The relaxation strength of the second peak as a function of inverse temperature. The solid line is the 1/T fit.

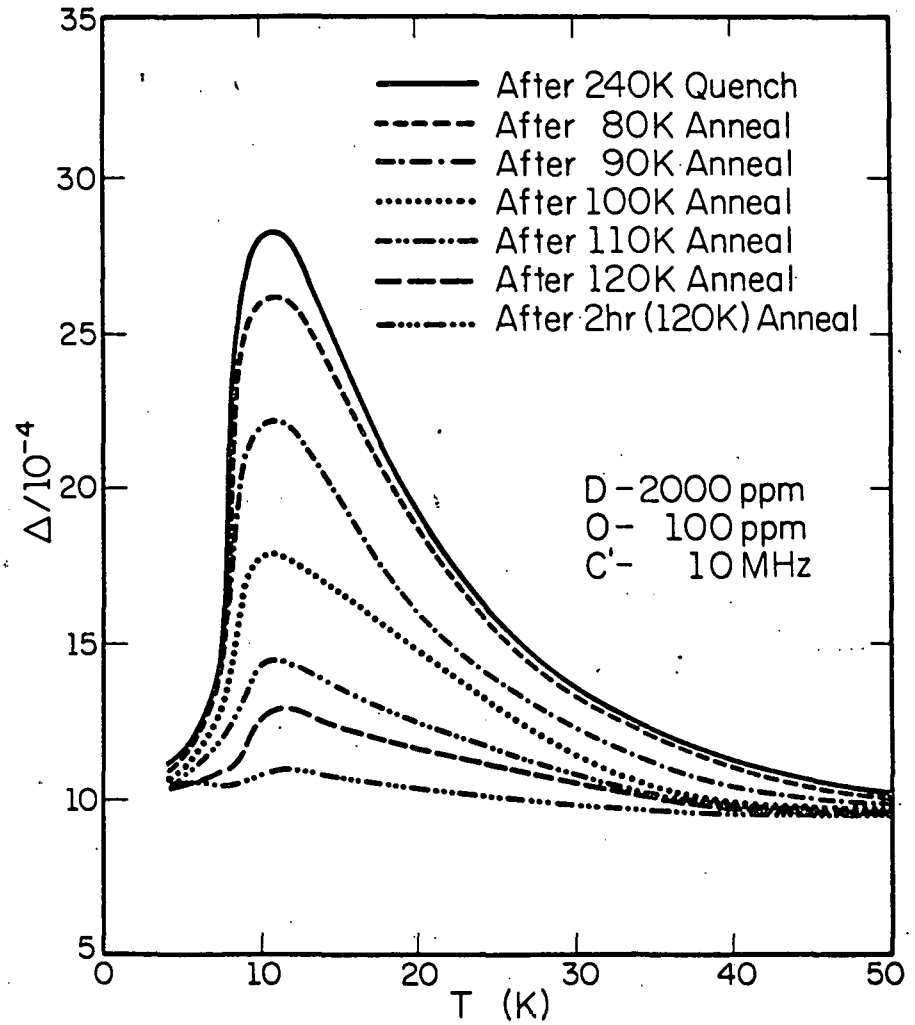

Figure 37. The decrement versus temperature for a 10 MHz C' mode in a niobium crystal containing about 100 ppm O and 2000 ppm D after a rapid cool down from 240 K, followed by annealing at 80, 90, 100, 110, and 120 K. The peak appears at 10.5 K and has a high temperature tail.

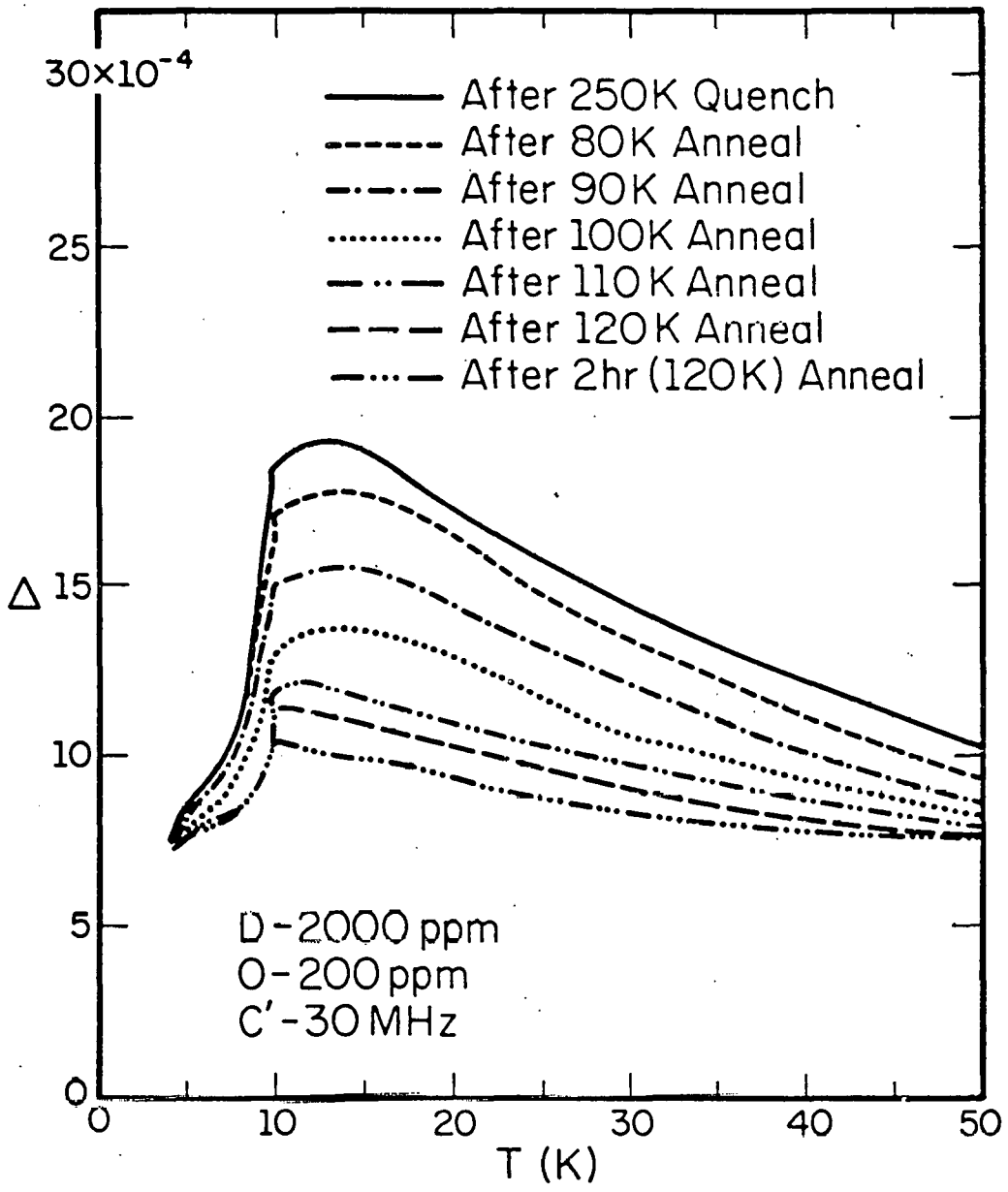

Figure 38. The decrement versus temperature for a 30 MHz C' mode in a niobium crystal containing about 200 ppm O and 2000 ppm D after a rapid cool from 250 K, followed by annealing at 80, 90, 100, 110, and 120 K.

frequency versus 1/T. The activation energy and frequency factor thus determined are 4.6 meV and 1.79×10^9 respectively.

3. Annealing Behavior

The annealing behavior of the hydrogen peaks is interesting. As mentioned earlier, peak 1 increased a little, while peak 2 annealed out. To find out whether the growth of peak 1 is correlated with the annealing of peak 2, one has to decompose the two peaks. This is difficult due to the fact that peak 2 is large compared with peak 1 and they are not far apart. One may assume that each peak has a fixed shape, during annealing, only the peak height is changing but not the shape. The shape of peak 1 can be readily obtained from the 120 K anneal data, because peak 2 is gone with only peak 1 left. The shape of peak 2 is undetermined.

If one assumes that peak 2 is a Debye peak, then the contribution of peak 2 tail at peak 1 can be obtained. By subtracting this contribution from peak 1, one gets the real height of peak 1. With the shape and height known for both peaks, one can add them up to see if the resultant can fit the data. Figure 39 shows the result for the case assuming that peak 2 is a Debye peak. The dashed curves are the two decomposed peaks. The dotted curve is the sum of these two peaks. The solid curve is the data. It clearly shows that the fit is bad in the temperature region in between the two peaks. Different shapes for peak 2 were used until a good fit was achieved. Figure 40 shows the example of a good fit, with the dashed curves representing the two decomposed peaks and the solid curve representing the data. With the peak shape determined this way, the two peaks were decomposed for each annealing temperature.

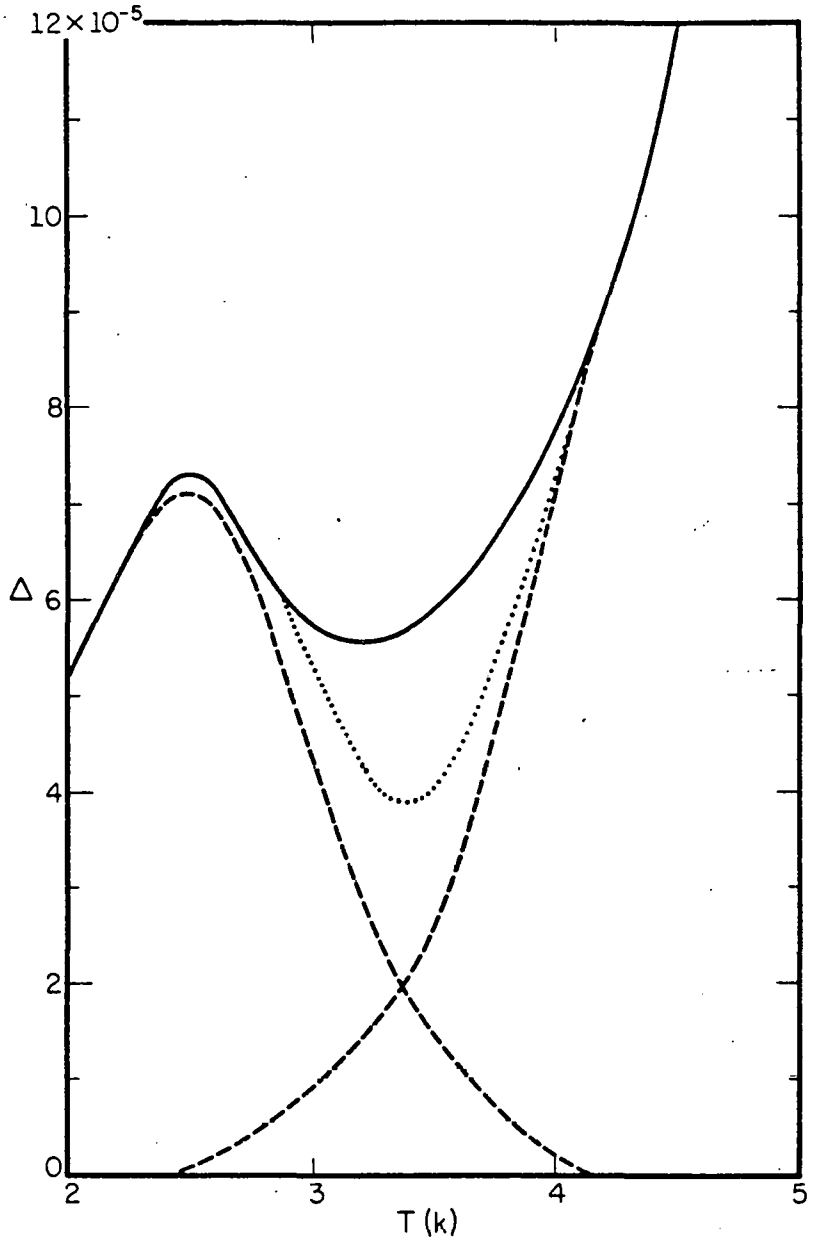

Figure 39. Decomposition of the two peaks with the assumption that peak 2 is a Debye peak. The two dashed curves represent the two decomposed peaks and the resultant of the two is the dotted curve, which is a bad fit to the solid curve (data).

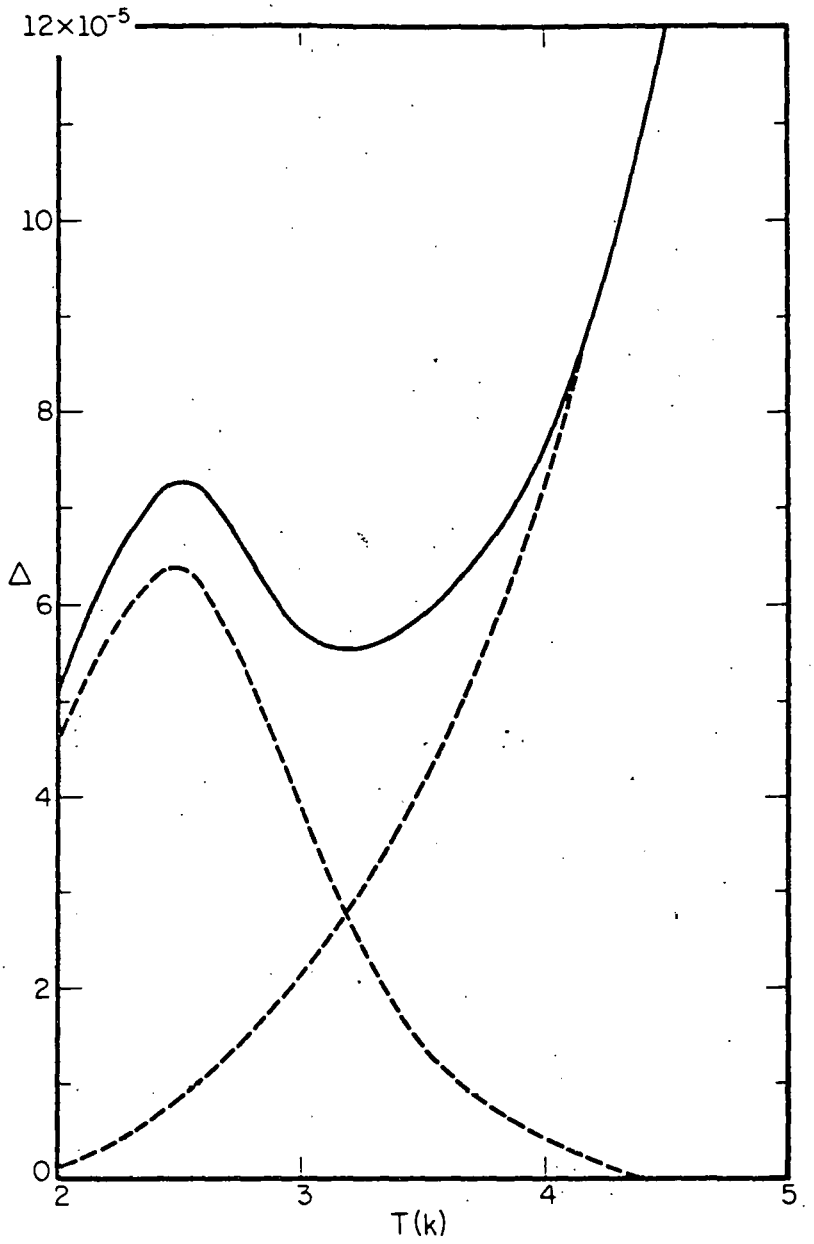

Figure 40. Decomposition of the two peaks. The dashed curves are the two decomposed peaks and the solid curve is the data.

The annealing data for the two decomposed peaks are plotted in Fig. 41. The curves show the normalized magnitude of each peak after a 10 minute anneal at the indicated temperature. The first peak increases by about 15% while the second peak anneals out. Shown in Fig. 42 is a plot of peak heights 1 versus 2 at each annealing temperature. A linear relation can be observed showing that the defects responsible for peak 2 become the defects responsible for peak 1 during annealing. Since peak 2 is about 6 times larger than peak 1 and the defect concentration of peak 2 is only about 15% that of peak 1, one may conclude that the relaxation strength of peak 2 is about 6/.15 = 40 times greater than that of peak 1.

4. Velocity Measurements

Velocity measurements were made from 0.6 K to 20 K for slow cooling and quenching from 240 K on a sample with 100 ppm oxygen and 700 ppm hydrogen. The frequency change as a function of temperature is plotted in Fig. 43. The 1/T decrease at low temperatures is much stronger than observed by Poker.[22] It is understandable because the sample had only 100 ppm oxygen. The little bump at 2.5 K apparently is due to peak 1, which is present in both slow cooling and fast cooling processes. The dispersion around 6 K is seen only in a fast cooling process, indicating that the second peak is due to a relaxation process.

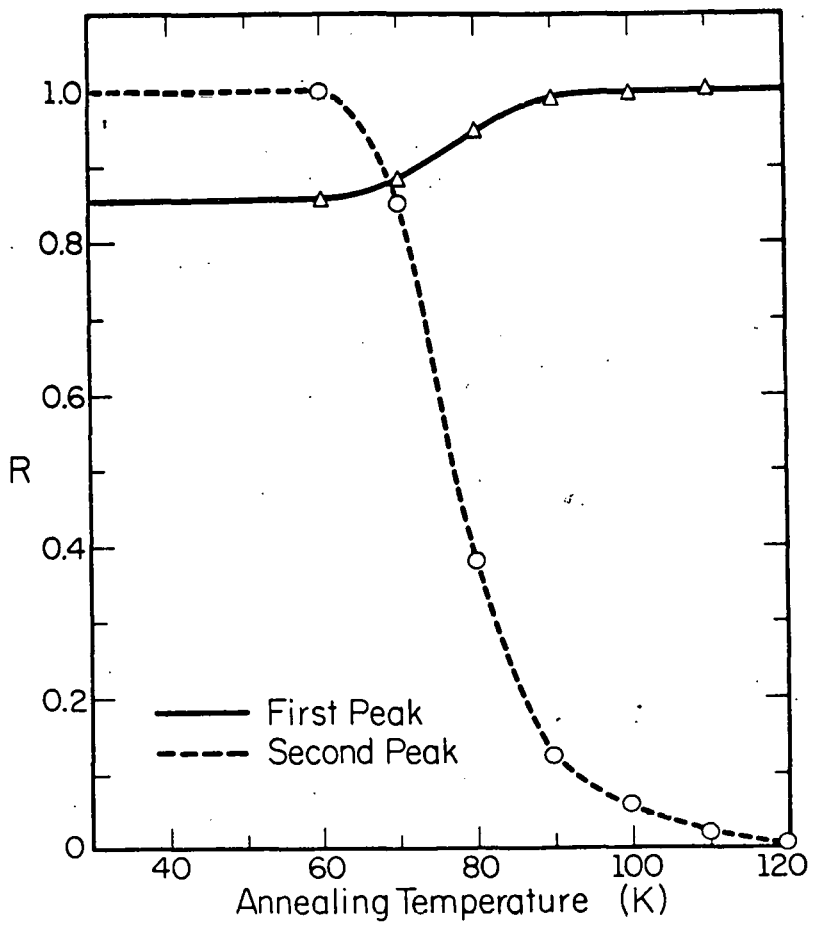

Figure 41. Annealing behavior of the two peaks. The solid and dashed curves represent the normalized magnitude of each peak after a 10 minute anneal at the indicated temperature. The first peak increases by about 15% while the second peak anneals out.

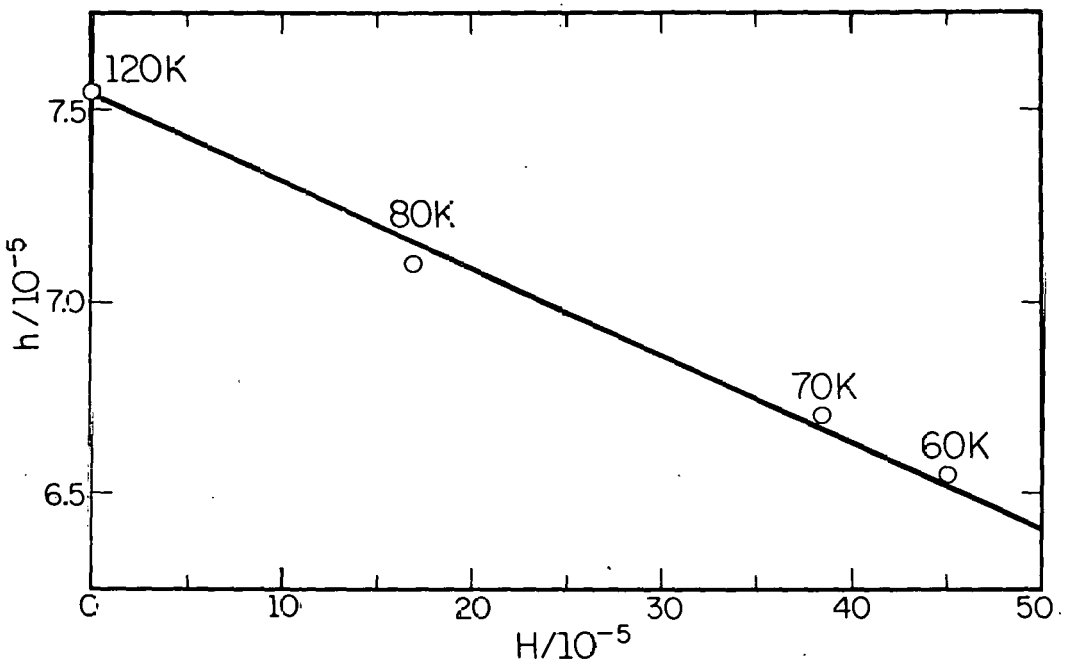

Figure 42. Peak height 1 (h) versus peak height 2 (H) at annealing temperatures 60 K, 70 K, 80 K and 120 K.

Figure 43. The frequency change versus temperature for a 10 MHz C' mode in a niobium crystal containing about 100 ppm O and 700 ppm H. The solid curve represents the result of a slow cooling process and the dashed curve represents that of a fast cooling from 240 K. The little bump near 2 K is seen in both slow and fast cooling processes. The decrease near 6 K is present only in the fast cooling process.

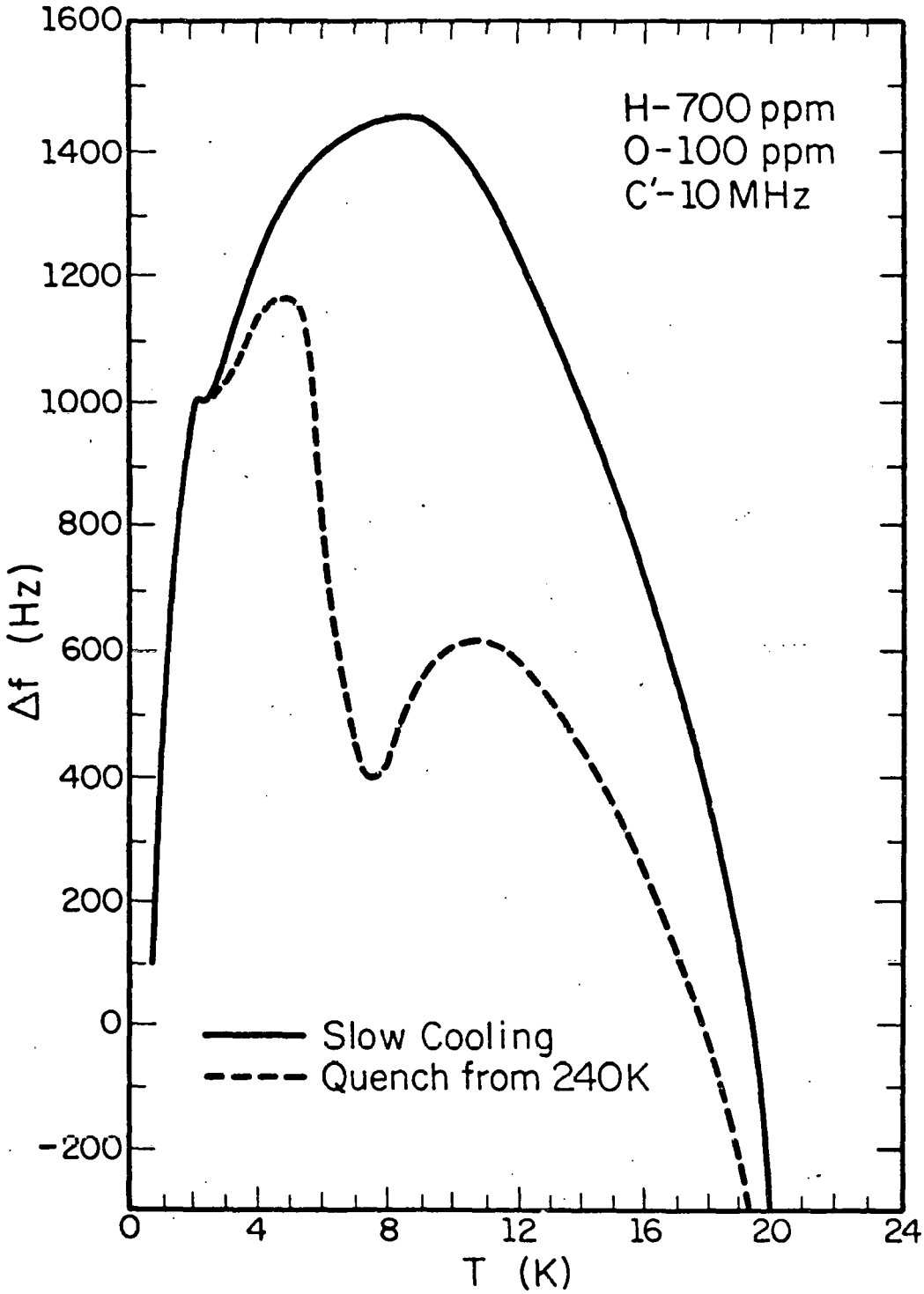
H-700 ppm
O-100 ppm
C'-10 MHz
Slow Cooling
Quench from 240K
Δf (Hz)
T (K)
1600
1400
1200
1000
800
600
400
200
0
-200
0
4
8
12
16
20
24

VIII. INTERPRETATION AND DISCUSSION

1. Interpretation

Quenching experiments on Nb with dilute concentrations of oxygen and hydrogen (or deuterium) by Hanada[43] and Engelhard[44] showed a resistivity increase at low temperatures, indicating that hydrogen was frozen into the lattice. The annealing data also showed that most of the quenched-in resistivity annealed out between 4.2 K and 100 K. Two major recovery stages were found, one centered at 40 K and the other at 80 K. The 80 K stage was observed only in the specimen with high oxygen content. It was interpreted as the detrapping of hydrogen freed from oxygen interstitials. However, since Pfeiffer and Wipf[13] had shown that the O-H pair was rather stable at 80 K, it was suggested by Hanada[43] that the quenched-in defects were OH_n complexes with $n = 2 \sim 4$.

Our annealing data showed that peak 2 annealed out at the same temperature, both for H and D, as those found by Hanada for quenched specimens. Also from the data measured on differing oxygen contents, one can know that the defect responsible for peak 2 is associated with oxygen. The correlation between peak 1 and peak 2 during annealing shows that peak 2 arises from an OH_2 complex. In a slow cooling process, one oxygen traps only one hydrogen at low temperatures, and this O-H pair is rather stable. In a rapid cooling process, some of the oxygen traps more than one hydrogen, forming an OH_2. However, the second hydrogen is less strongly bound than the first one. During annealing, detrapping of one of the two hydrogens occurs and an OH_2 becomes an OH with the freed hydrogen going into precipitates.

The simple interpretation can be expressed more properly by rate theory. First one can assume that hydrogen atoms are mobile in the lattice with a migration energy of E_m, and that oxygen atoms are immobile. As hydrogen is migrating through the lattice, if it sees an oxygen, an OH may be formed, if it sees an OH, then an OH_2 may be formed. These reactions can be expressed as

$$O + H \rightleftharpoons OH$$

$$OH + H \rightleftharpoons OH_2$$

The rate equations describing these reactions are

$$\frac{dC_{OH}}{dt} = \nu C_O C_H \exp(-E_m/kT) - \nu C_{OH} \exp[-(E_1 + E_m)/kT]$$

$$+ \nu C_{OH_2} \exp[-(E_2 + E_m)/kT] - \nu C_H C_{OH} \exp(-E_m/kT) \tag{40}$$

$$\frac{dC_{OH_2}}{dt} = - \nu C_{OH_2} \exp[-(E_2 + E_m)/kT] + \nu C_H C_{OH} \exp(-E_m/kT) \tag{41}$$

where C_H, C_O, C_{OH}, C_{OH_2} are the hydrogen, oxygen, OH and OH_2 concentrations, respectively, E_m is the migration energy of hydrogen, E_1 is the binding energy between O and H, E_2 is the binding energy between OH and H, ν is the vibrational frequency of hydrogen in any configuration (H, OH or OH_2). Conservation of total H and O further requires

$$C_H^T = C_H + C_{OH} + 2\, C_{OH_2} \tag{42}$$

$$C_O^T = C_{OH} + C_{OH_2} + C_O \tag{43}$$

Since in all the experiments, $C_H^T >> C_O^T$, one may assume that the hydrogen concentration can be approximated by that for a pure sample, which has the form

$$C_H = a \exp(-\Delta H/kT) \tag{44}$$

with the rest of hydrogen precipitating into β-phase hydrides. ΔH and a have been determined by Pfeiffer and Wipf[13] to be 0.12±0.015 eV and 4.7±0.9, with C_H given in H/Nb ratios.

In thermal equilibrium one has $dC_{OH}/dt = 0$ and $dC_{OH_2}/dt = 0$, whence

$$C_{OH_2} = C_H C_{OH} \exp(E_2/kT) \tag{45}$$

$$C_{OH} = C_H C_O \exp(E_1/kT) \tag{46}$$

One then can solve Equations 43, 44, 45 and 46 for C_{OH_2} and C_{OH}. The solutions are

$$\frac{C_{OH_2}}{C_O^T} = \frac{a^2 \exp[(E_1 + E_2 - 2\Delta H)/kT]}{a^2 \exp[(E_1 + E_2 - 2\Delta H)/kT] + a \exp[(E_1 - \Delta H)/kT] + 1} \tag{47}$$

$$\frac{C_{OH}}{C_O^T} = \frac{a \exp[(E_1 - \Delta H)/kT]}{a^2 \exp[(E_1 + E_2 - 2\Delta H)/kT] + a \exp[(E_1 - \Delta H)/kT] + 1} \tag{48}$$

The annealing process is rather complicated. At 80 K the second hydrogen of the quenched-in OH_2 may escape and becomes a free hydrogen migrating in the lattice. It can either precipitate or form another OH_2 when it sees an OH. Since the precipitation mechanism is not known, it is difficult to obtain the binding energy E_2 from the annealing data. However, E_2 cannot

be greater than E_1, otherwise one would get only OH_2, instead of OH, at low temperatures. A rough estimate of 0.07 eV for E_2 and 0.1 eV for E_m was used to calculate the equilibrium concentrations for OH and OH_2. Shown in Fig. 44 is a plot of these two concentrations versus temperature, with E_1 = 0.13 eV, ΔH = 0.12 eV, E_2 = 0.07 eV, a = 4.7 and C_O^T = 100 ppm. It shows that at room temperature, the specimen has certain fractions of O, OH and OH_2. As the specimen is cooled down slowly, the OH_2 concentration decreases and the OH concentration increases. At low temperatures, each oxygen traps only one hydrogen, no OH_2 remains. But if the specimen is cooled rapidly, a high temperature configuration with some OH_2 will be frozen in. Since the annealing data showed that the quenched-in configuration had a C_{OH}/C_{OH_2} ratio of 6, the frozen-in temperature could be around 130 K.

2. Discussion

A model using the same tunnelling sites described previously is proposed for OH_2. The two hydrogen atoms trapped by the oxygen may occupy two of those eight sites. However, according to Westlake,[45] the shortest distance two hydrogen atoms can have in a metal is about 2 Å, one then assumes that the two trapped hydrogen atoms have to stay on the opposite sides of the oxygen. Both hydrogen atoms can tunnel but they have to move together to keep H-O-H straight. Because the two hydrogen atoms are identical, only four states are expected, i.e., (a,g), (b,h), (c,e), (d,f), where (a,g) represents two hydrogen atoms occupying site a and g respectively, and similarly for the others. The state can change from (a,g) to (b,h) when the hydrogen at a going to b, and the hydrogen at g to h, with

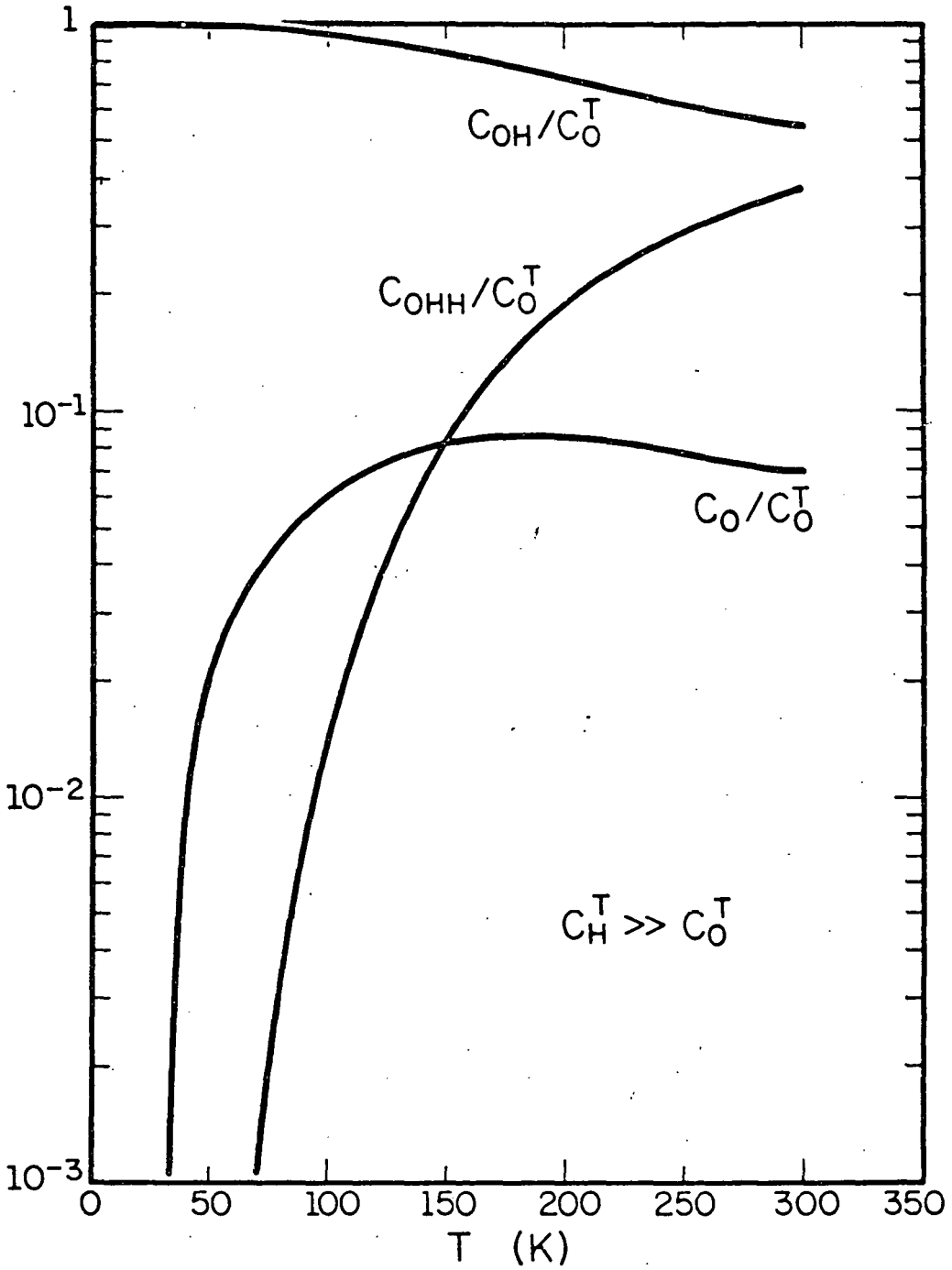

Figure 44. The concentrations C_{OH}/C_O^T, C_{OH_2}/C_O^T and C_O/C_O^T versus temperature.

a tunnelling matrix element α. The state can also change from (a,g) to (c,e), when the hydrogen at a tunnelling to e and the hydrogen at g tunnelling to c with a tunnelling matrix element β. A 4 × 4 matrix can be constructed with the two tunnelling matrix elements α, β

$$\begin{pmatrix} 0 & \alpha & \beta & \alpha \\ \alpha & 0 & \alpha & \beta \\ \beta & \alpha & 0 & \alpha \\ \alpha & \beta & \alpha & 0 \end{pmatrix}$$

Diagonalizing the matrix, one gets the four energy levels. Similar to the OH, the energy levels as a function of C' or C_{44} strains and the coupling between these levels can be obtained.

The energy levels for the C' strain can be expressed analytically

$$E_{1,2} = -\beta \mp \gamma\eta \tag{49}$$

$$E_{3,4} = \beta \mp (4\alpha^2 + \gamma^2\eta^2)^{1/2} \tag{50}$$

and the non-zero matrix elements at $\eta = 0$ through C_{44} are

$$\langle\psi_1|H_{44}|\psi_3\rangle = \langle\psi_2|H_{44}|\psi_3\rangle - \gamma_{44}/\sqrt{2} \tag{51}$$

$$\langle\psi_1|H_{44}|\psi_4\rangle = \langle\psi_2|H_{44}|\psi_4\rangle = \gamma_{44}/\sqrt{2} \tag{52}$$

where γ and γ_{44} are the strain coupling constants (see the Appendix). Shown in Fig. 45 are the energy levels as a function of C' strain. Since ψ_1 and ψ_2 are degenerate, an Orbach process can occur when a C' strain is applied. A C_{44} strain splits the degenerate states quadratically, hence no C_{44} effect is expected.

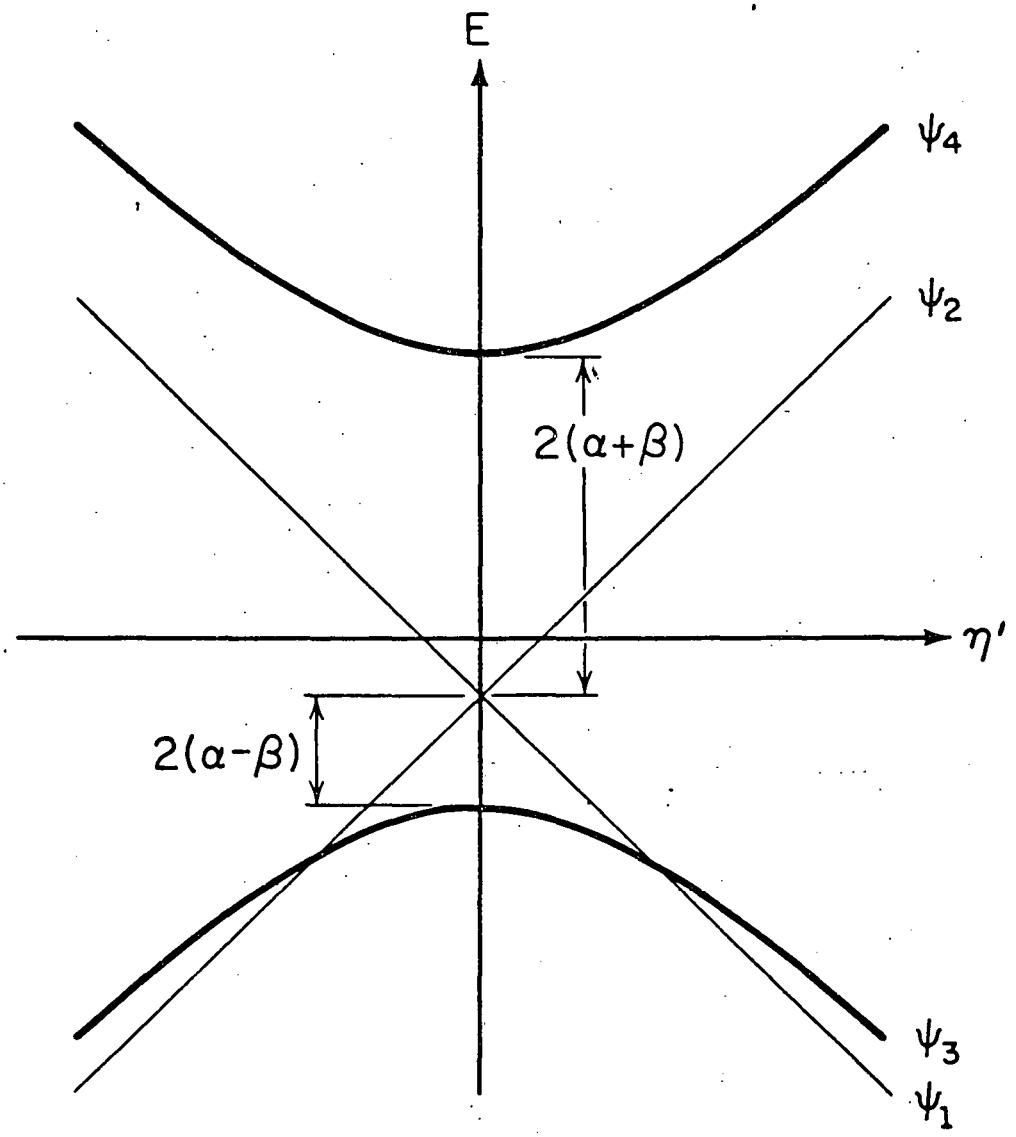

Figure 45. The energy levels as a function of C' strain for the four-state system. The first excited states are degenerate. A C' strain will split the degeneracy linearly.

If $\beta > \alpha$, then the energy difference between the ground state and the first degenerate excited states is $2(\beta - \alpha)$. Since the measured relaxation strength has a $1/T$ temperature dependence, the energy $2(\beta - \alpha)$ cannot be determined. The only information about α and β one can get is from the activation energy of the Orbach process, which is $2(\beta + \alpha)$. By comparing with experimental results, one gets $2(\beta + \alpha) = 5.5$ meV. One can also estimate γ by comparing with the relaxation strengths of OH and OH_2. Since the relaxation strength is proportional to γ^2,[22] and the OH_2 relaxation strength is about 40 times larger. The γ for OH_2 then is $\sqrt{40} \times 90$ meV = 570 meV.

IX. SUMMARY

A review of all the experimental data on Nb-N-H or Nb-O-H system is first given. The results that need to be explained are

(1) There is a low temperature specific heat anomaly due to hydrogen or deuterium in Nb. A large isotope effect is observed.

(2) Phonon mean free path minima are observed at 0.8 K for hydrogen charged niobium and 0.1 K for deuterium charged niobium.

(3) The vibrational levels of trapped hydrogen are about the same as those of free hydrogen, which are 0.11 eV and 0.16 eV with the higher one doubly degenerate.

(4) Inelastic neutron scattering experiments show that there is an energy transfer to the hydrogen tunnelling system. The energy is about 0.19 meV.

(5) A low temperature ultrasonic relaxation peak is observed at 2.5 K for a 10 MHz C' mode, but not for a C_{44} mode, on a sample charged with hydrogen and oxygen. The relaxation time has an exponential temperature dependence and the relaxation strength shows a quantum depletion effect. The ultrasonic attenuation for a deuterium charged sample has a step-like temperature dependence, which is rather unusual. The behavior of the velocity is also unusual, which cannot be explained by any existing theory.

(6) High temperature (150~200 K) relaxations are observed for both C' and C_{44} mode.

An eight state model then is proposed and the properties of the system is developed. A comparison of the predictions of this model with the

available data is made. Four parameters which can be determined separate-by the specific heat data and the ultrasonic data are sufficient to describe the properties of the model.

A reasonable fit is made to the low temperature specific heat data for both hydrogen and deuterium. The fit uses a concentration of 50 ppm which is much lower than what would be expected from residual resistivity ratio. A comparison with the fit based on a two-state model is made. It appears that the eight-state model can fit the data with a small concentration and the two-state model cannot fit the data for any concentration.

The eight-state model clearly predicts that only a C' relaxation will be seen at low temperature for hydrogen. An Orbach process is proposed to account for the relaxation time, and the low temperature depletion of the relaxation strength is also predicted by the model. Furthermore, a direct process is proposed to explain the unusual behavior of attenuation and velocity data, a satisfying fit to the data is obtained.

High temperature (150~200 K) relaxations for both C' and C_{44} mode are also predicted, with the system making a transition from coherent tunnelling at low temperatures to incoherent hopping at high temperatures.

The model also predicts phonon resonant scattering at 0.18 K for deuterium charged specimen, which is close to that observed. The phonon mean free path minimum observed at 0.8 K might be due to phonon scattering from dislocations.

A crude calculation for the potential is given, using an $1/r^6$ potential and taking into account the Nb-H, O-H interaction and the heavily displaced two nearest neighbor niobium atoms with respect to the oxygen. It

demonstrates the existence of the main features of the model, and that the energy levels found in neutron spectroscopy are not incompatible with the model.

In Part B, ultrasonic studies of rapidly cooled Nb-O-H systems are given. An additional peak is found at 6.3 K for hydrogen and at 10.5 K for deuterium for a 10 MHz C' mode, when the specimen is cooled rapidly. The peak anneals at the same temperature, for both hydrogen and deuterium, as those found by Hanada in their resistivity quenching experiments. An OH_2 complex is suggested to be the defect responsible for the peak. A model in terms of an extension of the model given in Part A is proposed to account for the relaxation.

APPENDIX

CALCULATION OF THE STRESS ENERGY USING λ TENSOR

To obtain the strain dependence of the energy levels, one needs to know the strain interaction energies first. Suppose hydrogen is localized in site a, then the λ tensor expressed in the principal axes coordinate system (x',y',z'), with x' along the O-H defect direction will be

$$\lambda^{a}_{(x',y',z')} = \begin{pmatrix} \lambda_1 & 0 & 0 \\ 0 & \lambda_2 & 0 \\ 0 & 0 & \lambda_3 \end{pmatrix} \tag{1}$$

λ^a can also be expressed in the crystal coordinate system by rotating the coordinate axes. For example, here one needs only to rotate Z' an angle of θ to get

$$\lambda^{a}_{(x,y,z)} = \begin{pmatrix} \lambda_1 \mathrm{Cos}^2\theta + \lambda_3 \mathrm{Sin}^2\theta & 0 & (\lambda_3 - \lambda_1)\mathrm{Sin}\theta\mathrm{Cos}\theta \\ 0 & \lambda_2 & 0 \\ (\lambda_3 - \lambda_1)\mathrm{Sin}\theta\mathrm{Cos}\theta & 0 & \lambda_1 \mathrm{Sin}^2\theta + \lambda_3 \mathrm{Cos}^2\theta \end{pmatrix} \tag{2}$$

where θ is the angle between the O-H defect direction and the x-axis of the crystal. Similarly, λ^b λ^c,...., λ^h can be obtained.

The strain energy is defined as

$$H = \tilde{\sigma} \cdot \tilde{\varepsilon} \tag{3}$$

where $\tilde{\sigma}$ is the stress tensor and $\tilde{\varepsilon}$ the strain tensor.

For a C' type stress in the xy plane, the stress tensor in the crystal coordinates has only two non-zero elements, $\sigma_{xx} = -\sigma_{yy} = \sigma$. Therefore the strain energy for hydrogen localized at site a is

$$\begin{aligned}\tilde{\sigma} \cdot \tilde{\lambda}^a &= \sigma[(\lambda_1 \mathrm{Cos}^2\theta + \lambda_3 \mathrm{Sin}^2\theta) - \lambda_2] \\ &= C'\eta\,[(\lambda_1 \mathrm{Cos}^2\theta + \lambda_3 \mathrm{Sin}^2\theta) - \lambda_2] \\ &= \gamma\eta \qquad (4)\end{aligned}$$

where C' is the elastic constant and η is the strength of the strain and $\gamma \equiv C'[(\lambda_1 \mathrm{Cos}^2\theta + \lambda_3 \mathrm{Sin}^2\theta) - \lambda_2]$. Similarly one has

$$\begin{aligned}&\tilde{\sigma} \cdot \tilde{\lambda}^a = \tilde{\sigma} \cdot \tilde{\lambda}^c = \tilde{\sigma} \cdot \tilde{\lambda}^e = \tilde{\sigma} \cdot \tilde{\lambda}^g = \gamma\eta \\ &\tilde{\sigma} \cdot \tilde{\lambda}^b = \tilde{\sigma} \cdot \tilde{\lambda}^d = \tilde{\sigma} \cdot \tilde{\lambda}^f = \tilde{\sigma} \cdot \tilde{\lambda}^h = -\gamma\eta \qquad (5)\end{aligned}$$

For a unit strain, one may write

$$\begin{aligned}H'|a\rangle &= \gamma|a\rangle \\ H'|b\rangle &= -\gamma|b\rangle \quad \text{etc.} \qquad (6)\end{aligned}$$

For a C_{44} strain pulling along the crystal body diagonal, $\tilde{\sigma}$ can be expressed as

$$\tilde{\sigma}_{44} = \frac{\sigma}{3} \begin{pmatrix} \cdot & \cdot & \cdot \\ \cdot & \cdot & \cdot \\ \cdot & \cdot & \cdot \end{pmatrix} \qquad (7)$$

Hence

$$\tilde{\sigma}_{44} \cdot \tilde{\lambda}^a = \frac{1}{3}\sigma\ (\lambda_3 - \lambda_1)\mathrm{Sin}2\theta = \frac{1}{3} C_{44}\ \eta_{44}\ (\lambda_3 - \lambda_1)\mathrm{Sin}2\theta$$

$$\equiv \gamma_{44}\eta_{44} \tag{8}$$

where $\gamma_{44} = \frac{1}{3} C_{44}(\lambda_3 - \lambda_1)\mathrm{Sin}2\theta$

Similarly,

$$\tilde{\sigma}_{44} \cdot \tilde{\lambda}^a = \tilde{\sigma}_{44} \cdot \tilde{\lambda}^b = \tilde{\sigma}_{44} \cdot \tilde{\lambda}^g = \tilde{\sigma}_{44} \cdot \tilde{\lambda}^h = \gamma_{44}\eta_{44}$$

$$\tilde{\sigma}_{44} \cdot \tilde{\lambda}^c = \tilde{\sigma}_{44} \cdot \tilde{\lambda}^d = \tilde{\sigma}_{44} \cdot \tilde{\lambda}^e = \tilde{\sigma}_{44} \cdot \tilde{\lambda}^f = -\gamma_{44}\eta_{44} \tag{9}$$

or

$$H_{44}|a\rangle = \gamma_{44}|a\rangle$$

$$H_{44}|c\rangle = -\gamma_{44}|c\rangle \qquad \text{etc.} \qquad \text{for unit strain.} \tag{10}$$

With the eight states and the strain-stress interaction, one may calculate all the matrix elements. Listed below are all the non-zero matrix elements through C' and C_{44}.

$$\langle\psi_1|H'|\psi_4\rangle = \langle\psi_5|H'|\psi_8\rangle = \gamma$$

$$\langle\psi_2|H_{44}|\psi_5\rangle = \langle\psi_2|H_{44}|\psi_8\rangle = \gamma_{44}/\sqrt{2}$$

$$\langle\psi_3|H_{44}|\psi_5\rangle = \langle\psi_3|H_{44}|\psi_8\rangle = \gamma_{44}/\sqrt{2}$$

$$\langle\psi_1|H_{44}|\psi_6\rangle = \langle\psi_1|H_{44}|\psi_7\rangle = \gamma_{44}/\sqrt{2}$$

$$\langle\psi_4|H_{44}|\psi_6\rangle = \langle\psi_4|H_{44}|\psi_7\rangle = \gamma_{44}/\sqrt{2} \qquad (11)$$

Since γ_{44} = 76 meV, one can calculate $(\lambda_3 - \lambda_1)/v_o$ from Equation 8.

$$\lambda_3 - \lambda_1 = \frac{3\,\gamma_{44}}{C_{44}\cdot \mathrm{Sin}2\theta} = 1.41 \times 10^{-24}\ \mathrm{cm}^3$$

$$(\lambda_3 - \lambda_1)/v_o = 0.078$$

where v_o is Nb molecular volume and $\theta \simeq 35°$. Similarly, from γ, one gets

$$(\lambda_1 \mathrm{Cos}^2\theta + \lambda_3 \mathrm{Sin}^2\theta - \lambda_2)/v_o = (0.7\lambda_1 + 0.3\lambda_3 - \lambda_2)/v_o$$

$$= 0.014$$

REFERENCES

1. P. P. Matyask, N. A. Skakun and N. P. Dikii, JETP Letters 19, 18 (1974).
2. H. D. Carstanjen, Phys. Stat. Sol. (a) 59, 11 (1980).
3. T. Schober and H. Wenzl, in Topics in Applied Phys., Vol. 29, Hydrogen in Metals II, eds. G. Alefeld and J. Völkl, Springer-Verlag, Berlin-Heidelberg-New York, 1978, p. 11.
4. A. Somenkov, A. V. Gurskaya, M. G. Zemlyanov, M. E. Kost, N. A. Chernoplekov and A. A. Chertkov, Sov. Phys.-Solid State 10, 1076 (1968).
5. A. Magerl, N. Stump, H. Wipf and G. Alefeld, J. Phys. Chem. Solids 38, 683 (1977).
6. G. J. Sellers, A. C. Anderson and H. K. Birnbaum, Phys. Rev. B 10, 2771 (1974).
7. C. Baker and H. K. Birnbaum, Acta Metall. 21, 865 (1973).
8. C. P. Flynn and A. M. Stoneham, Phys. Rev. B 1, 3966 (1970).
9. R. F. Mattas and H. K. Birnbaum, Acta Metall. 23, 973 (1975).
10. G. Matusiewicz and H. K. Birnbaum, J. Phys. F 7, 2285 (1977).
11. G. O'Hara, G. J. Sellers and A. C. Anderson, Phys. Rev. B 10, 2777 (1974).
12. D. G. Westlake and S. T. Ockers, Met. Trans. 6A, 399, edited by K. D. Timmerhaus, W. J. O'Sullivan and E. F. Hammel (Plenum Press, New York, 1974) Vol. 3, p. 372.
13. G. Pfeiffer and H. Wipf, J. Phys. F 6, 167 (1976).
14. C. Morkel, H. Wipf and K. Neumaier, Phys. Rev. Lett. 40, 947 (1978).
15. A. Magerl, V. Wagner and N. Stump, Solid State Commun. 33, 627 (1980).

16. D. Richter and S. M. Shapiro, Phys. Rev. B 22, 599 (1980).

17. J. J. Rush, A. Magerl, J. M. Rowe, D. Richter and H. Wipf, Bull. Am. Phys. Soc. 27, 162 (1982).

18. H. Wipf, A. Magerl, S. M. Shapiro, S. K. Satija and W. Thomlinson, Phys. Rev. Lett. 46, 947 (1981).

19. H. Wipf, K. Neumaier, International Symposium on the Electronic Structure and Properties of Hydrogen in Metals, Richmond, Virginia, March 1982.

20. D. B. Poker, G. G. Setser, A. V. Granato and H. K. Birnbaum, Z. Phys. Chem. N.F. 116, 39 (1979).

21. H. K. Birnbaum and C. P. Flynn, Phys. Rev. Lett. 37, 25 (1976).

22. D. B. Poker, Ph.D. Thesis, Physics Department, University of Illinois at Urbana-Champaign, 1979.

23. H. Wipf, A. Magerl, S. M. Shapiro, S. K. Satija and W. Thomlinson, Proc. Miami Int. Symp. on Metal-Hydrogen Systems, Miami, 1981.

24. R. Orbach, Proc. R. Soc. A 264, 458 (1961).

25. M. D. Kemple, Ph.D. Thesis, Physics Department, University of Illinois at Urbana-Champaign, 1971.

26. K. L. Hultman, Ph.D. Thesis, Physics Department, University of Illinois at Urbana-Champaign, 1979.

27. K. W. Kehr, in Topics in Applied Phys., Vol. 28, Hydrogen in Metals I, eds. G. Alefeld and J. Völkl, Springer-Verlag, Berlin-Heidelberg-New York, 1978, p. 203.

28. P. E. Zapp and H. K. Birnbaum, Acta Metall. 28, 1275 (1980).

29. P. E. Zapp and H. K. Birnbaum, Acta Metall. 28, 1523 (1980).

30. A. C. Anderson and S. C. Smith, J. Phys. Chem. Solids 34, 111 (1973).

31. G. K. Pandey and D. K. Shukla, Phys. Rev. B 3, 4391 (1971).

32. H. Sugimoto and Y. Fubai, Phys. Rev. B 22, 670 (1980).

33. H. Sugimoto and Y. Fubai, J. Phys. Sol. Japan 50, 3709 (1981).

34. M. S. Blanter and A. G. Khachaturyan, Met. Trans. 9A, 753 (1978).

35. T. Ochs, J. Phys. E 1, 1122 (1968).

36. T. Schober and H. Wenzl, in Topics in Applied Phys., Vol. 29, Hydrogen in Metals II, eds. G. Alefeld and J. Völkl, Springer-Verlag, Berlin-Heidelberg-Ner York, 1978, p. 57.

37. R. Truell, C. Elbaum and B. Chick, in Ultrasonic Methods in Solid State Physics, Academic Press, New York, 1969.

38. H. P. Wong, Ph.D. Thesis, Physics Department, University of Illinois at Urbana-Champaign, 1982.

39. A. S. Nowick and W. R. Heller, Adv. Phys. 12, 251 (1963).

40. A. S. Nowick and W. R. Heller, Adv. Phys. 14, 101 (1965).

41. A. S. Nowick and B. S. Berry, Anelastic Relaxation in Crystalline Solids, Academic Press, New York, 1972.

42. W. P. Mason, Physical Acoustics and the Properties of Solids, D. Van Nostrand Company, Inc., Princeton, New Jersey, 1958.

43. R. Hanada, Second International Congress on Hydrogen in Metals, 1B6, Paris, 1977.

44. J. Engelhard, J. Phys. F: Metal Phys. 9, 2217 (1979).

45. D. G. Westlake, Int. Symposium on the Electronic Structure and Properties of Hydrogen in Metals, Richmond, Virginia, March 1982.

VITA

Kai-feng Huang was born on [redacted] He received his secondary education at First Taichung High School, Taichung, Taiwan. He then attended National Taiwan University and received a Bachelor of Science degree in physics in June, 1976. He has been a graduate student at the University of Illinois, receiving a Master of Science degree in January, 1978.